The application of hybrid Computational Fluid Dynamics to optimize the air curtain of a refrigerated display cabinet

By

L.A.Milano

in partial fulfilment of the requirements for the degree of

Master of Science
in Mechanical Engineering

at the Delft University of Technology,

Student number:	5180694		
Project duration:	November 23, 2021 – July 11, 2022		
Thesis comittee:	Dr. R. Delfos	(supervisor)	TU Delft
	Dr.ir. M.J.B.M. Pourquie	(supervisor)	TU Delft
	Dr.ir. R. Pecnik		TU Delft
	Prof.dr.ir. K. Hooman		TU Delft
	Ir. R.E.W. Berents	(supervisor)	Fri-jado

TU Delft Delft University of Technology

fri-jado

Acknowledgements

Firstly, I would like to thank my supervisors. Rene Delfos, for organizing meetings with other thesis students, providing constructive feedback with regards to the experimental part of my thesis and support with the experimental setup of the infrared measurements. Mathieu Pourquie I would like to thank for the constructive feedback he gave me for the simulation part of my thesis. I am also very grateful to my Fri-jado supervisor Robert Berents, who supported my research ideas and providing me with a very interesting thesis experience in which I was able to do experiments and was able to use commercial simulation packages. I would also like to thank Jan Diepstraten and Elvis Boekhoudt for providing me with excellent support during the experimental testing in the Fri-jado lab. In addition, I would like to thank Roos Lievaart for constructing the thermocouple and infrared frames, which I used for my experiments. Furthermore, I would like to thank the entire Product Development division of Fri-jado for being involved in my research, providing feedback and creating a pleasant working environment. Finally, I would also like to thank my parents and my girlfriend Milou, who supported me through the entire TU Delft master by keeping me motivated and helping me to focus on achieving my goals.

Contents

List Of Figures

List Of Tables

Abstract

Conventionally, the geometry of the Fri-Jado open vertical refrigerated display cabinet design is optimized by drawing and producing the new components and testing the new configuration in a climate chamber, which is known to be an iterative process that consumes a large amount of time. To speed up the optimization process, the application of computational fluid dynamics (CFD) was proposed. For this thesis, a case study was performed on a specific Fri-Jado cabinet that required many iterations for optimizing the geometry, using the commercial Simscale CFD package. In addition, experimental tests were performed on the Fri-Jado cabinet to compare with the simulation results.

During the experimental testing and literature review, it was found that the entrainment of ambient air was the main component of the heat load for the cabinet. By designing and validating a simplified 2D $k-\omega$ SST simulation of the air curtain and external environment, an optimization study was performed. In this optimization study, it was found that for an offset angle of 10° and throw angle of 25° in combination with a stepped velocity profile, minimal thermal and mass entrainment ratios were reached.

1. Introduction

In 2019, the International Institute of Refrigeration estimated that the refrigeration sector-related greenhouse gas emissions account for 4.14 Giga tonnes CO_2eq, representing 7.8% of global greenhouse gas emissions. In total, approximately 5 billion refrigeration systems (including air-conditioning) are in operation, of which 120 million units can be related to commercial refrigeration (Dupont et al., 2019) [1]. Commercial refrigeration comprises equipment used by retail outlets for preparing, holding and displaying frozen and fresh food and beverages for customer purchase, as defined by the Intergovernmental Panel on Climate Change (Agarwal et al., 2018) [2].

Greenhouse gas emissions coming from the cold chain can be subdivided in direct (refrigerant leakage) and indirect (energy derived from fossil fuels to generate electricity) categories (T.Grof, 2009) [3]. Dupont et al. estimated that the refrigeration sector, including air conditioning, consumes about 20% of the overall electricity used worldwide, which could more than double by 2050, due to increasing refrigeration demand in numerous sectors and global warming, highlighting a significant contribution of emissions due to energy consumption. Moreover, indirect emissions vary from about 60% to over 90% of the total cold chain emissions historically, depending on the amount of refrigerant recovered (Amrane, 2019) [4].

Besides emissions related to the refrigeration equipment itself, additional emissions can be related to food waste that depend on the refrigeration performance, as the food quality and storage time is affected by the temperature (Lindenberg & Jensen, 2014) [5]. Moreover, critical food products, such as meat, fish and dairy products perish very quickly if not stored under 5 °C, being a threat to health (Dudeja & Singh, 2017) [6]. In the end, making a good economic decision between food waste and cooling performance can prove to be a difficult process.

Moreover, improper usage of refrigeration systems can further increase the emissions. New regulations in Paris now prohibit leaving the doors open for consumers, while running the air conditioning system (NOS, 2022) [**7**]. The same problem is present in commercial refrigeration, where one can observe many doors of refrigeration equipment left open when passing through a retail store.

Not much information is known about the distribution of emissions in commercial refrigeration. Approximately one third of the energy use in the commercial refrigeration sector can be attributed to supermarkets (Westphalen et al., 1996) [8]. Another study investigated the emissions in UK supermarkets and implies that refrigerated display cabinets are responsible for approximately 50% of the total supermarket's greenhouse gas emissions (Faramarzi, 1999) [9].

Refrigerated display cabinets can be divided in access to food with doors (closed type) or without doors (open type). The advantage of an open type cabinet is that there is no physical barrier between the product and customer, allowing customers to be more drawn to products than in closed type cabinets. A second distinction is made in the shape of the cabinet. The shape can be vertical or horizontal. An open vertical refrigerated display cabinet with multiple shelves (multi-deck) is the most used cabinet because it allows the customer almost unrestricted access to the product (Navaz et al., 2015) [10]. Therefore, an open vertical refrigerated display cabinet will now be referred to as 'cabinet'. Since doors are not present in these cabinets, additional thermal insulation is realized by flowing cold air over the open interface that makes contact with the environment. This airflow is called the air curtain. The disadvantage of these cabinets is that they typically consume more energy than vertical closed type refrigerated display cabinets (Fricke & Becker, 2010) [11].

About 67% - 77% of the thermal load in these cabinets is due to infiltration of warm and moist ambient air across the air curtain, while approximately 6-12% can be related to thermal radiation and 7% - 10% to lighting (Gaspar,

Gonçalves & Pitarma, 2011)[12]. Therefore, the thermal entrainment factor of the air curtain seems to be the main performance indicator in the case of these cabinets. (Chaomuang, Flick & Laguerre, 2017)[13]. Nevertheless, thermal radiation can have a significant impact in loading on the frontal area of the products (Laguerre, Hoang & Flick, 2012)[14], while lighting can increase front and top loading of products by 0.1 ~ 1.2 °C in these cabinets (Zihjuan et al., 2013)[15]. In addition, ambient conditions such as air velocity, ambient temperature and relative humidity greatly influence the heat transfer to the cabinet (Chen & Yuan, 2005) [16]. In order to guarantee a cabinet design that fits realistic ambient conditions, while maintaining a good product temperature distribution, guidelines provided by NEN-EN-ISO 23953-2 can be followed (International Organization for Standardization, 2015) [17].
Conventionally, improving the cooling performance of these cabinets requires an iterative process involving alterations to the computer aided design (CAD) model, producing the new design and performing tests in climate chambers, which can take up a large amount of time and money. A proven and effective way of optimizing the aforementioned process is the combination of CFD and experimental validation, called hybrid CFD (Norton & Sun, 2006) [18].
In the past, multiple studies that made use of the hybrid CFD method have been conducted. Cortella computed the airflow pattern and food temperature distribution of an open type and closed type cabinet by making use of an in-house CFD code (Cortella, 2002) [19]. D'Agaro, Cortella & Groce, 2006 [20] made two-dimensional (2D) and three-dimensional (3D) steady state and transient simulations of the airflow pattern and temperature distribution in a frozen food cabinet using a commercial CFD code and compared the results with experiments. Ge & Tassou, 2001 [21] used CFD to develop correlations for the heat transfer across refrigerated display cabinet air curtains and validated these correlations experimentally. Ge, Tassou and Hadaway, 2010 [22] developed a model for a cabinet with integration of CFD and cooling coil sub models. Gaspar, Gonçalves & Pitarma [23] created a two-dimensional (2D) CFD simulation of a cabinet taking into account the airflow through internal ducts, across fans, evaporator and grilles and the heat conduction through food products for steady-state. [10] used CFD in combination with particle image velocimetry (PIV) and laser doppler velocimetry to validate and optimize the airflow distribution in the air curtain of a cabinet.
All of these studies used cabinets that had perforated back panels (PBP's) installed inside the cabinet. While it's known that the airflow through the PBP stabilizes and fortifies the air curtain [16], it also blocks the view on the food products, reducing the total display area. The energy efficiency index (EEI) for a cabinet equals

$$\mathrm{EEI} = \frac{\mathrm{AE}}{\mathrm{SAE}} \tag{1}$$

With AE the annual electrical energy consumption and SAE the reference annual electrical energy consumption, which is calculated based on the type of cabinet, as described by the regulations of the European union. A lower EEI indicates a better energy performance. Since multi-deck refrigerated display cabinets have all compartments within the same temperature class, these terms are (European Union, 2017) [24]

$$\mathrm{AE} = 365 \cdot \mathrm{E_{daily}} \tag{2}$$

and

$$\mathrm{SAE} = 365 \cdot \mathrm{P} \cdot (\mathrm{M} + \mathrm{N} \cdot \mathrm{A_{total}}) \cdot \mathrm{C} \tag{3}$$

with:

- $\mathrm{E_{daily}}$ the daily electrical energy consumption
- M, N, P and C being positive constants dependent on the cabinet type which are determined by Fri-Jado
- Where $\mathrm{A_{total}}$ is the total display area

Indicating that a lower EEI can also be achieved with an increase in display area. Therefore, the implementation of a PBP into a cabinet is not necessarily beneficial for the EEI because it reduces the display area. One could combine a PBP with a more transparent material to increase the display area. However, with the implementation of a PBP back doors cannot be used for service purposes and costs are increased (Fri-jado, 2021) [25]. An alternative, potentially more cost-effective approach that ensures the preservation of back doors and a low EEI would be the removal of the PBP, increasing the total display area and SAE. However, the absence of the PBP causes an additional air curtain in the back, which can lead to more unpredictability of the flow field. Obviously, stabilization of the frontal air curtain must now be ensured by an alternative solution than the PBP.

Therefore, the aim of this study is to improve the air curtain design of a cabinet without a PBP, by the use of the hybrid CFD method.
The studied cabinet will be the Fri-jado MCC Cold 90 ss as shown in figure 1. The used CFD software will be the commercial Simscale package (Simcale, 2021) [26].

Fig. 1. The studied cabinet: MCC COLD 90 ss in the climate chamber, during the experimental testing.

1.1. Fri-Jado B.V.

Since 1937 Fri-Jado develops and manufactures equipment that prepares, presents and preserves hot and cold food products, being one of the first companies in the Netherlands active in this sector. All the equipment is developed, engineered and produced in the headquarters based in Oud-Gastel (NL). The manufactured equipment is exported to 70 different countries globally. Their equipment is used by world-wide supermarket organisations, convenience stores, fast-food restaurant, butchers, speciality stores and petrol stations. Fri-Jado has its own research and development lab, which is facilitated by two state of the art climate chambers and advanced measurement tools.

1.2. Thesis Outline & Research Objectives

In the second chapter, the experimental tests that have been performed on the cabinet are discussed. Firstly, the experimental apparatus is described in this chapter to provide the reader with insight in the geometry of the cabinet, air flow circulation and cooling principles. In addition, the most important test for assessing the performance of the cabinet is discussed, in which thermocouple thermometry is involved. Hereafter, experimental techniques and performance parameters are identified and reviewed, which can be used for further experimental testing and optimization of the cabinet. In addition, the physics of the air curtain is described and the problem of ambient air entrainment that occurs in the frontal air curtain of the cabinet is validated. Moreover, insight will be gained in the modelling of the air curtain. Finally, additional experimental data is obtained and reviewed in this chapter, which can later be used for the simulation of the cabinet.

In chapter 3, a review on previous cabinet/ air curtain simulations is performed, including the 3D simulation of the case study cabinet to get a good indication of how the simulation domain of the air curtain should look like and other subjects such as temporal dependency and demarcation of the flow domain are discussed. In addition, benchmark tests that were already performed by Simscale and have relevance to the physics of the air curtain are assessed and the need for performing additional benchmark tests that validate the simulation of an air curtain are supported.

To get more insight into the commercial Simscale package, the available numerics, mesh generators, models and solvers are discussed in chapter 4, which can later be used for setting up the simulation.

Chapter 5 focusses on the validation of the simulation, in which the benchmark tests are performed and reviewed. In addition, the geometry used for the Fri-Jado air curtain is reviewed and validated. Chapter 6 focusses on the optimization of the air curtain.

The main research question of this study which was previously introduced and additional sub questions that are answered in this research are defined below. The answer to the research questions is provided in chapter 7.

How can the air curtain of an open vertical refrigerated display cabinet design without a PBP be optimized, by making use of the hybrid CFD method?

1. *What performance parameters can be used for optimization of the cabinet?*
2. *What are the physics of the air curtain?*
3. *What benchmark tests are needed to validate the commercial Simscale software?*
4. *What numerical methods should be used for the simulation?*
5. *What is the accuracy of the benchmark test(s)?*
6. *What is the accuracy of the air curtain simulation used for optimization?*
7. *What is the interaction between the design parameters and what modifications can be made to the cabinet?*

2. Experimental Testing

In this chapter the experimental apparatus is described in section 2.1 to provide the reader with a better picture of the cabinet. Test results that have been obtained by Fri-Jado on the cabinet in the past are reviewed in section 2.2. This section clarifies why the implementation of CFD can potentially optimize the Fri-Jado design routine. Moreover, experimental techniques and performance parameters that can aid in assessing the cabinet design are discussed in section 2.3. As mentioned in the introduction, thermal entrainment of the air curtain is expected to be the main factor for the thermal loading. Therefore, to better understand the physics of the air curtain, the general physics of the air curtain are described in section 2.4.

2.1. Experimental Apparatus

Figure 2 shows the mid-plane cross-section of the cabinet and figure 3 depicts a cartoon of the airflow of the cabinet. Pictures of the experimental setup are shown in appendix A, figure A1.

Fig. 2. Mid-plane Cross-section of the cabinet. Each blue colored and green contoured M-package has a thermocouple inserted.

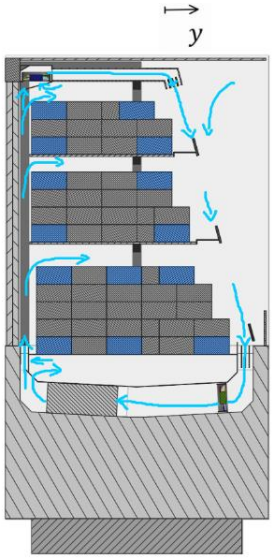

Fig. 3. Cartoon of the airflow in the cabinet.

Temperature is regulated with a temperature sensor, which is placed in between the evaporator fins. Heat is transferred via the condenser to an ambient air flow that is generated by additional fans. When the system is cooling and the air temperature gets below its set point of -4.5°C, the evaporator stops cooling by turning of the compressor in the coolant circuit. The cooling restarts when a temperature of -3.5°C is measured by the temperature sensor. If the setpoint is reached too slow, frozen condensate droplets will form on the evaporator fins, blocking the air flow-through area. To counteract this problem, cooling takes place at a faster pace, such that the water vapor in the air sublimates on the evaporator fins, leaving behind a greater air gap than in the case of freezing condensate. The condensed water is transferred out of the cabinet through a drain located in the evaporator room. In addition, a defrosting interval initializes once every 3 hours. During this interval, cooling will stop until the temperature sensor measures a temperature greater than a prescribed temperature, or if the defrosting interval takes longer than 30 minutes. Figure 4 shows a typical air temperature versus time plot to illustrate the aforementioned temperature interval in between two defrosting periods. The measured temperatures are sampled by a Yokogawa data acquisition system and are displayed on a SMARTDAC+ digital recorder, as shown in figures 5 and 6.

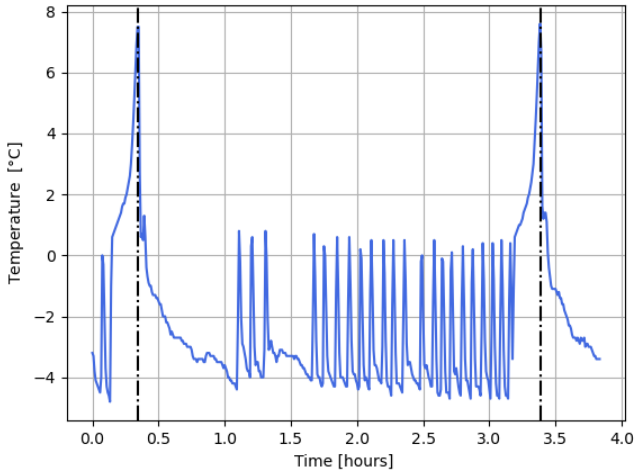

Fig. 4. The cooling cycle initiates at the left black dashed line, while the defrosting cycle ends at the right at the right black dashed line black dashed line.

Fig. 5. Yokogawa data acquisition system.

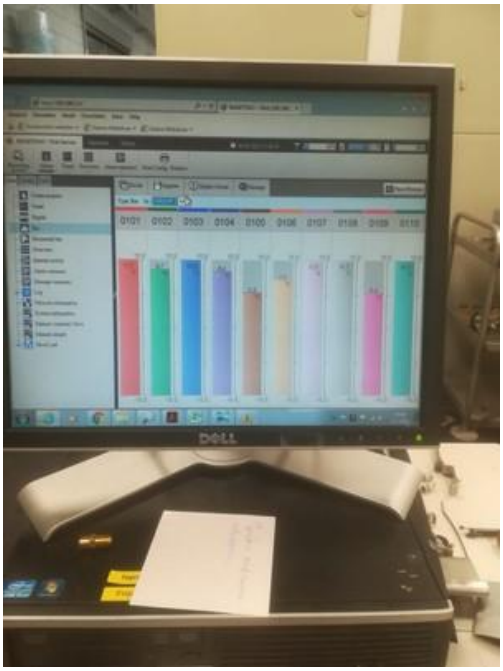

Fig. 6. SMARTDAC+ digital recorder. This picture depicts the measured temperatures for a set of thermocouples.

Food products are located on all the shelves. Five fans located in front of the evaporator draw air from the ambient environment. The air passes through the evaporator and is cooled below the conservation temperature of the perishable products. A part of the air is discharged through perforations that lead to the clearance space. This air is then discharged to the conservation space in order to convectively cool the products that are located on shelf 3. The other part of air is discharged through the back discharge air grille (BDAG) in the conservation space where all the products are located. The BDAG has inclined compartments of 5° at the sides to guide a greater amount of air towards the side walls, to counteract the shear effect caused by the boundary layers at the side walls. These compartments are shown in figure 7. Each sliding has a different spacing with respect to the shelves, creating an unequal flowthrough surface for the air that goes from the BDAG to the back return air grille (BRAG).

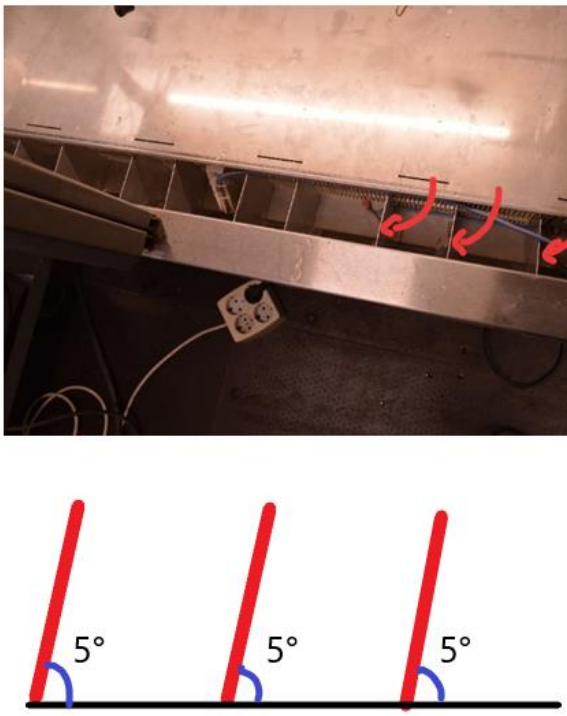

Fig. 7. The photo shows a top view of the BDAG for the new design. The arrows indicate the air guidance strips that are inclined with 5° with respect to the side walls. The same inclination holds for the other side of the BDAG. The schematic depicts the front view of the air guidance strips.

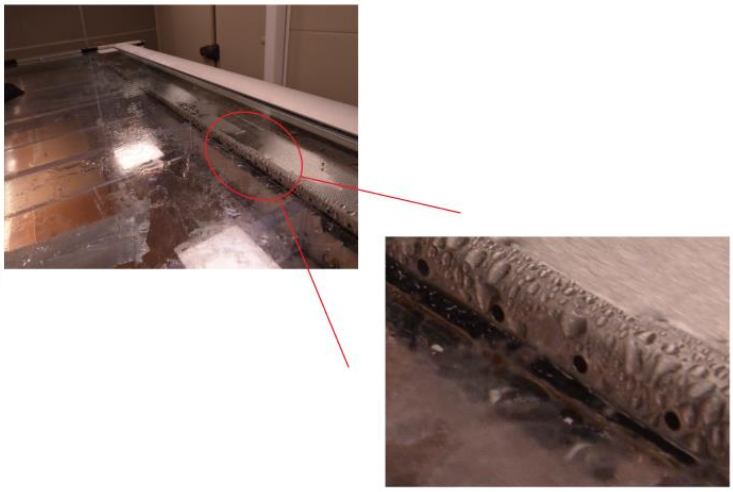

Fig. 8. Circular perforations added to the upper fan room.

Air from the top of the conservation space is drawn in by five top fans through the BRAG and is convected to the front discharge air grille (supply). In addition, figure 8 shows circular perforations that were added to the upper fan room, with the goal to decrease the amount of condensate film that is deposited on the ceiling of the cabinet.

The air mass leaving the front discharge air grille supplies the air curtain that develops vertically between the supply and the front return air grille (return). Air guiding strips are attached to all the shelves, which help to improve to air curtain strength and thus reduce the impact of warm ambient air (Sun et al., 2017) [27][25]. The dimensions of this cabinet are 900 × 750 × 1320 mm (L × W × H). The frontal opening height H_f is 714.5 mm. The side walls, back doors, top and child lock are made of perspex. A cartoon of the air flow in the cabinet is depicted in figure 3. Food products are represented by M-packages in accordance with NEN-EN-ISO-23953. A standard M-package weighs 500 g and has dimensions 50 × 100 × 100 mm. However, note that different dimensions are also possible for the filler M-packages that are used to complete the loading. A T-type thermocouple is inserted in the center of a standard M-package at locations according to NEN-EN-ISO 23953. The thermocouples are in direct contact with the filling material, which consists of 115 g of oxyethylmethylcellulose, 382.1 g of water, 2.5 g of sodium chloride and 0.4 g of para-chlorometa-cresol. A sheet of transparent colorless plastic encloses the filling material. A schematic of the M-package inserted with a thermocouple is depicted in figure 9. For this case study, a total of 42 thermocouples were

inserted in M-packages. Figure 2, in combination with the front view of the cabinet depicted in figure 10 give a complete picture of the M-package loading. Twelve thermocouples are positioned on shelf 1 and shelf 2 and 18 in shelf 3.

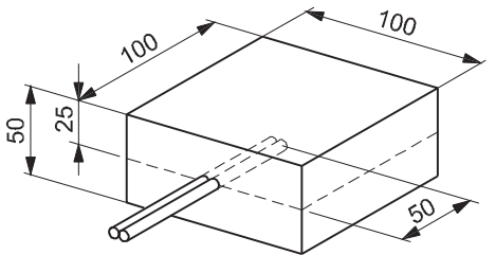

Fig. 9. Standard M-package (dimensions in mm) inserted with a thermocouple in compliance with NEN-EN-ISO 23953 (International Organization for Standardization, 2015) [17].

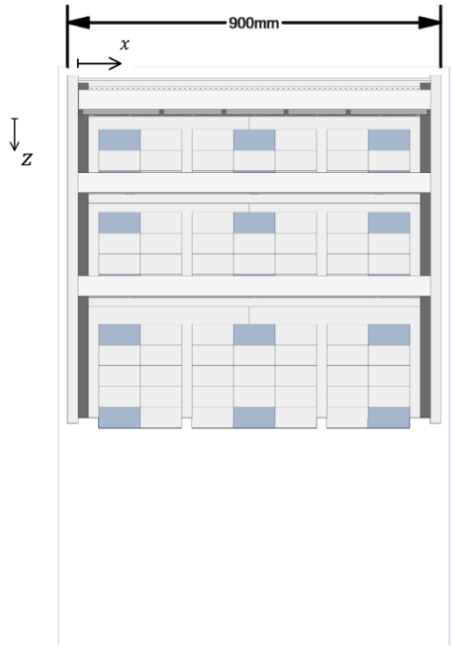

Fig. 10. Front view of the cabinet.

There are 2 Hielkema climate rooms available for experimental testing that are in compliance with NEN-EN-ISO 23953. Both climate rooms are a parallelepiped space with dimensions 6900 × 3900 × 3000 mm (L × W × H) for climate room 1 and dimensions 5400 × 3900 × 3000 for climate room 2. The condensing unit of the refrigeration system is located beneath the cabinet, making the system self-contained. Because the condenser airflow rises and potentially re-enters the cabinet, an air deflector is used to guide the air away from the cabinet in the streamwise direction of the ambient cross flow. Figure 11 shows the air deflector with the sketched air flow. Additional pictures of the experimental setup can be found in appendix A.

Fig. 11. The air deflector used to guide away the warm condenser air from the cabinet. The duct has a closed and open end at the indicated locations.

2.2. 3M1 Conditions & M-package Temperature Test from The Previous Measurement

M-package temperature measurements are needed to validate the cooling performance of the cabinet.
The test conditions under which the M-package temperatures have to be measured are 3M1, as described by table 1. Note that it is allowed to deviate from the test conditions by some margin as described in the ISO regulations. Therefore, Fri-jado aims to minimize the temperature and relative humidity inside this margin, such that the thermal loading is decreased. Hence the test conditions applied by Fri-Jado are are $55\%\ ^{+5\%}_{0\%}$ and $24\ ℃\ ^{+1°C}_{0°C}$.

Table 1. 3M1 test conditions according to NEN-EN-ISO-23953.

Test Condition	Symbol	Value
Test Room Dry Bulb Temperature (℃)	T_{amb}	$25 \pm 1\ ℃$
Test Room Relative Humidity (%)	RH	$60 \pm 5\%$
Test Room Air Velocity (ms^{-1})	u_{amb}	0.2
M-Package Temperature Range (℃)	$T_{package}$	$-1 \leq T_{package} \leq 5$
Lux measured 1m above floor level (lx)	lux	600 ± 100
Emissivity walls, ceilings and wrapper @ 25°C (-)	ε_{amb}	$0.9 \leq \varepsilon \leq 1$

During the test, a thermocouple and a humidity sensor were attached to the top of the cabinet. Both sensors were used for feedback such that the setpoint of the climate chamber could be manually changed, in the case that the aforementioned 3M1 conditions of the climate chamber were not met. The ambient temperature was measured with a T-type thermocouple and calibrated to correct any errors. In total, the temperature and humidity were measured for 24 hours. The configuration of the humidity sensor and thermocouple is according to NEN-EN-ISO 23953-2 and shown in figure 12.
Note that the air velocity of the test room is parallel to the frontal opening plane of the cabinet. The operation of the cabinet is considered stable if for 24 hours in between two defrosting periods the M-package temperatures fluctuate no more than $\pm$ 0.5 ° C.
In the past, M-package temperature measurements have been conducted by Fri-jado according to NEN-EN-ISO-23953, in climate chamber 1. It has to be highlighted that during this test, climate cell conditions were offset by some margin due to flow perturbation by dust particles coming from clogged filters in the circulation circuit of the climate chamber. Setpoints of 22.5 ℃ and 60% were used to reach the 3M1 conditions for the climate chamber (the setpoints used by the author are 24℃, 58% and 15 Hz climate room fan speed, because during these measurements the filters weren't clogged anymore. More on these measurements is explained later in this chapter).

Fig. 12. Configuration of the thermocouple and humidity sensor**.**

During the test performed by Fri-Jado in the past, only the maximum and minimum temperatures were recovered for each M-package. These temperatures are shown in the figures 14 and 13. Both figures show that the M-packages with the highest temperature are located in the front of the cabinet. As described in literature, thermal entrainment of ambient air into the air curtain is the main component of the thermal load and has the greatest impact on the frontal M-packages (Evans Scarcelli & Swain, 2007) [28][13]. Moreover, [20] created a 3D transient simulation of an air curtain for a refrigerated display cabinet. Their simulations show that by increasing the cabinet length from one to two meters, a decrease of 20% in refrigeration power per unit length would occur. In addition, the extra thermal load was said to occur due to the increase of end-wall vortices. An experimental proof of the increased thermal entrainment near the end walls is shown in section 2.4. It has to be noted that Fri-jado has dealt with this phenomenon in the past. In particular, they changed the inclination angle of the air guidance fins inside the BDAG to a 5° angle such that additional cold air is guided towards the side walls, as previously discussed and shown in figure 7.
Finally, figures 14 and 13 show that the greatest temperature change is from the back to the front. This temperature gradient exists because the coldest air in the conservation space is neighboring the BDAG while being in the back of the cabinet. Significant temperature changes can also be observed in the z and x direction, indicating that the cabinet is affected by the thermal loading in three dimensions.
In total it took 54 iterations in changing the design, over a period of 85 days to approach 3M1 conditions, highlighting the urgency of the optimization problem. After the last iteration, only 1 M-package measured a maximum temperature of 5.2 °C, exceeding the 3M1 package temperature limit. Therefore, the 3M1 certification requirements were not achieved, which clearly gives rise to the topic whether CFD can be used for optimization purposes of the cabinet.

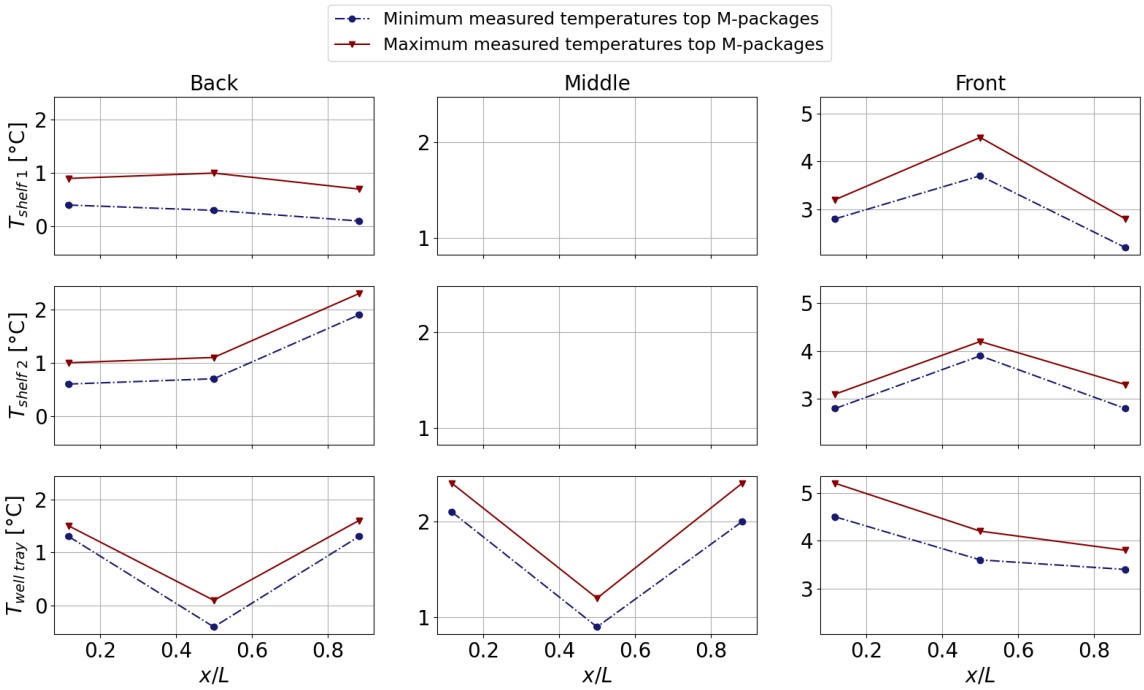

Fig. 13. Temperature distribution of the top M-packages located on each shelf (see figure 10 for more information about the coordinate axis, appendix C1 for the dataset and appendix D for the exact locations of the thermocouples). Each marker in the plot represents the temperature that was measured with a thermocouple in the center of a M-package.

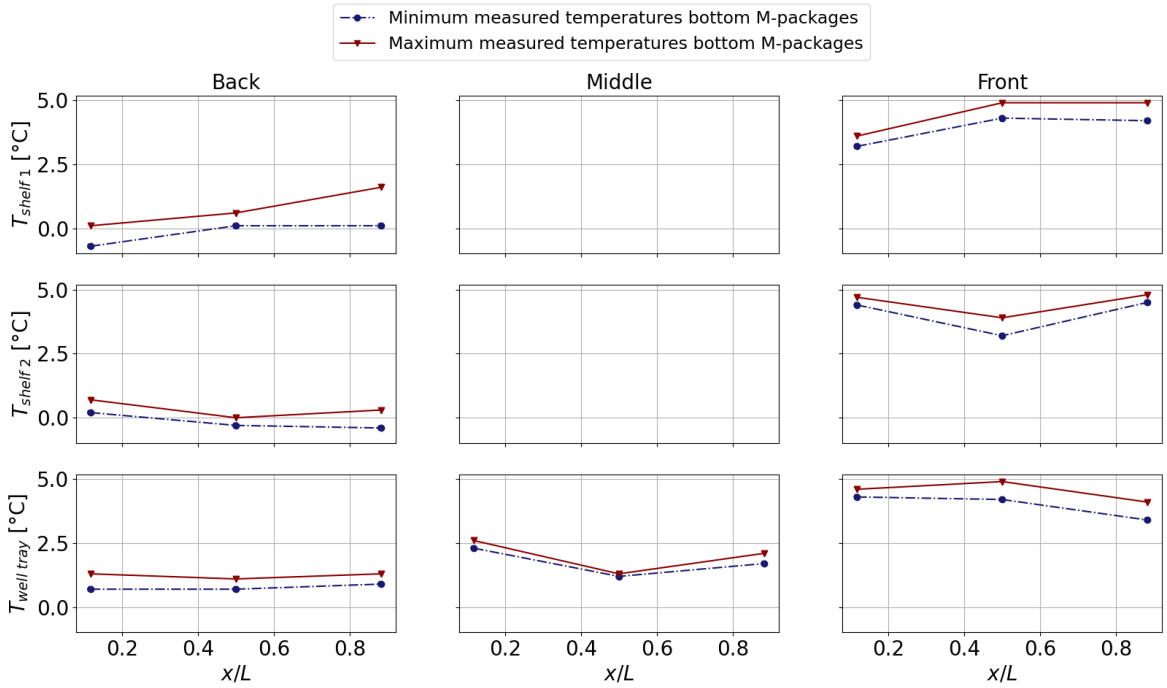

Fig. 14. Temperature distribution of the bottom M-packages located on each shelf field (see figure 10 for more information about the coordinate axis, appendix C1 for the dataset and appendix D for the exact locations of the thermocouples). Each marker in the plot represents the temperature that was measured with a thermocouple in the center of a M-package.

2.3. Experimental Techniques & Performance Parameters

Experimental techniques and performance parameters can be used to give an indication on how good the design of a cabinet is and how it can be optimized.

Firstly, infrared (IR) thermography can be used to evaluate the temperature field of the air curtain and M-packages and approximate local thermophysical parameters such as the local heat transfer coefficient of the air curtain. One could use the local heat transfer coefficient for optimizing the efficiency of the air curtain. For computing the local heat

transfer coefficient, a paper grid with a low thermal conductivity is placed in the air flow. Because the paper has a high emissivity, it will maximize the radiative heat transfer to the IR camera. Assuming negligible thermal conduction in the paper grid, thermal equilibrium between convection and radiation is reached after a certain time, indirectly making the IR camera a way of visualizing the convective heat transfer. With the assumption of thermal equilibrium between convection and radiation across the paper grid, the local heat transfer coefficient can be approximated by

$$\bar{h}(\bar{y},\bar{z}) = \frac{\varepsilon\sigma\left(T(\bar{x},\bar{z})^4 - T_{refl}^4\right)}{T(\bar{x},\bar{z}) - \overline{T}_{refl}} \tag{4}$$

where $\bar{x}$ and $\bar{z}$ are the local coordinates on the paper grid (Figure 15), σ the Stefan Boltzmann constant, T_{refl} the reflected temperature and $\overline{T}_{refl}$ is the mean reflected temperature, which includes dependency on the local coordinates (Danjoux, Pastor & Thunevin, 2010) [29]. However, for the air curtain of the cabinet it was concluded that it would take a lot of effort to measure the air temperature at each point of the air curtain. Moreover, the area that the paper grid needs to capture is much smaller and more complex than the grid that was used in the experiments of [29]. Moreover, the side walls are made of glass and have a significant emittance. To top off, many surfaces present in the cabinet have temporally dependent temperatures and different view factors with respect to a single point on the paper grid. Therefore, the heat transfer coefficient is tedious to compute. Hence, IR thermography is only used to qualitatively measure the temperature field of the M-packages and air curtain.

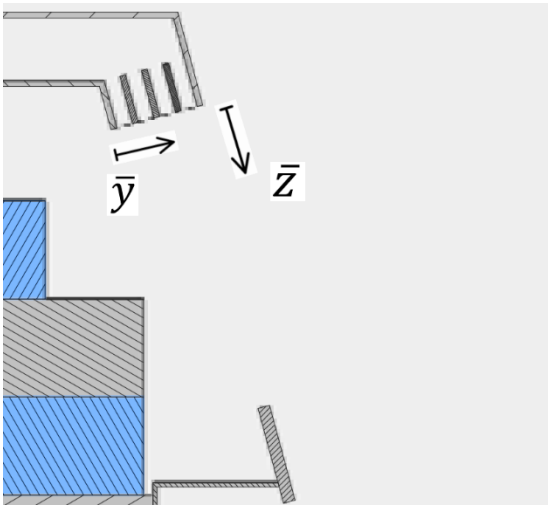

Fig. 15. Local coordinate axes for the air curtain.

Next, Gaspar, Gonçalves & Pitarma (2007) [30] measured air temperatures at different locations in the air curtain of a cabinet, to examine the influence of different frontal opening lengths on the thermal entrainment ratio. The thermal entrainment ratio is defined by

$$\alpha_T = \frac{h_{return} - h_{jet}}{h_{amb} - h_{jet}} \tag{5}$$

where subscript ‘jet’ refers to the start of the air curtain when it leaves the supply and return refers to the end of the air curtain before the fans inside the return.
Equation (5) is derived by the enthalpy method as described by Navaz et al. (2005) [31]. Note that in this method, the thermal entrainment is calculated based on an energy balance with a control volume that demarcates the entire air curtain. Hence the thermal entrainment ratio is based on both the entrained air and the spilled air. Also note that the temperatures of the supply and return should be measured at points where the flow is well-mixed i.e. before the supply in the upper fan space and below the return in the lower fan space.

The thermal entrainment ratio can be used as an engineering approximation to evaluate the thermal performance of a cabinet. One way to use this parameter is by testing the fans with different blade configurations, dimensions and rotational speeds [12]. Equation (5) can be simplified by assuming a constant specific heat capacity. A thermal entrainment ratio that is equal to 0 indicates no entrainment of ambient air for $T = T_{jet}$. A thermal entrainment ratio that reaches unity indicates complete entrainment of ambient air for $T = T_{amb}$. In addition, Field and Loth (2006) [32] showed that the thermal entrainment ratio increases with an increase in the Richardson number, which is defined by

$$Ri = \frac{(\rho_{amb} - \rho_{jet})gb}{\rho_{amb} u_{jet}^2} = \frac{(T_{amb} - T_{jet})gb}{T_{jet} u_{jet}^2} \tag{6}$$

Since an increasing Richardson number indicates an increase in buoyancy force, the air curtain destabilizes and tends to move inwards the cabinet. Moreover, it is known that an increase in the Richardson enhances mixing with the ambient. On the other hand, increasing the Richardson number for a fully packed cabinet can decrease the air curtain detachment to the packages, which favorably affects heat transfer (Kalluri & Loth, 2003) [33]. The Richardson number and Reynolds number can be related by the Grashof number

$$Ri = \frac{Gr}{Re^2} \tag{7}$$

Where the Grashof number equals

$$Gr = \frac{(\rho_{amb} - \rho_{jet})gb^3}{\rho_{amb} \left(\frac{\mu_{jet}}{\rho_{jet}}\right)^2} \tag{8}$$

Equation (7) shows that when the Grashof number stays constant, an increasing Richardson number reduces the Reynolds number and can potentially decrease the product of $\alpha \cdot Re$, which is known as the relative thermal entrainment. Gray et al. (2008) [34] validated this result with experimental testing on a cabinet. However, it has to be noted that the experiments are only valid for Reynolds between 4700 and 8000. On the contrary, Field, Kalluri & Loth (2002) [35] concluded that only at a Reynolds number of about 100 or less, buoyancy forces become of significance for the thermal entrainment indicating that the air curtain should have more momentum. The Reynolds number is defined by

$$Re = \frac{\rho u_{jet} b}{\mu} \tag{9}$$

A proper Reynolds number of 3200-3400 at the supply is recommended to maintain a good balance between buoyancy and inertial forces [31]. While many different experiments were performed on cabinet's with PBP's, it has to be remarked that the Reynolds number that was obtained experimentally, is not generically applicable to all types of cabinets, since the geometry of the studied cabinet is unique. Therefore, different Reynolds numbers can be recommended for different types of cabinet designs. Hence, a more precise statement with regards to the relationship between the Richardson number, Reynolds number and thermal entrainment has yet to be formulated for the Fri-Jado cabinet geometry.

Besides the thermal entrainment, one can also compute the mass entrainment. The infiltration rate can be calculated by integrating the negative values of the entrainment velocity over the opening of the cabinet (Navaz et al., 2002) [36] (i.e. the velocity vector points towards the control volume of the air curtain). Therefore, the infiltration rate doesn't take into account the spilled air, as opposed to the thermal entrainment ratio. Consequently, the mass entrainment ratio can be calculated by dividing by the inlet mass flow of the supply

$$\alpha_M = \frac{\int \rho u_{entrainment} dx}{\int \rho u_{jet} dy} \tag{10}$$

By assuming a constant density one can also compute the volumetric flowrates instead. Note that the computation of the infiltration rate can only be applied to the simulation because no accurate measurement tool for measuring the velocity profiles of the air curtain is available. A second method that can be used for determining the infiltration ratio is the tracer gas technique as proposed by Amin, Dabiri & Navaz (2009) [37]. In this method, a tracer gas with close molar weight to air is injected into the system, by which the infiltration ratio is computed by the concentration differences in tracer gas. This method will not be used because it requires modifications to the cabinet and additional monetary investments. Alternatively, the absolute infiltration mass flow rate can be approximated by measuring the amount of condensate [9].

It was shown that the infiltration rate linearly increases with the turbulence intensity, indicating that a low turbulence intensity is preferred (Amin, Dabiri & Navaz, 2011; Amin, Dabiri & Navaz, 2012) [38][39]. In the work of [9], the infiltration rate of the air curtain of a cabinet with a PBP was reduced by changing the geometry of the supply, reducing the turbulence intensity. The validation was obtained experimentally by PIV and laser doppler velocimetry and it was shown that for a reduced turbulence intensity at the supply, a more parabolic velocity profile in the air curtain was maintained, with less shear between the air of the conservation space and surroundings, finally resulting in reduced entrainment of ambient air. The turbulence intensity at the supply is defined by

$$I_{jet} = \frac{u'}{u_{jet}} \tag{11}$$

where u_{jet} is the Reynolds averaged supply velocity and u' is the root mean square value of the velocity fluctuations

$$u' = \sqrt{\frac{\sigma_{u_x}^2 + \sigma_{u_y}^2 + \sigma_{u_z}^2}{3}} \tag{12}$$

The velocity fluctuation can be calculated by recording the measured velocity and consequently computing the standard deviation by

$$\sigma_{u_z} = \sqrt{\frac{\sum_{i=1}^{n} u_i - u_z}{n-1}} \tag{13}$$

where n is the number of samples. While using equations (11), (12), and (13) definitely give a good indication on the state of performance of the cabinet it has to be emphasized that in order to measure these velocity fluctuations, a measurement tool with a high resolution, such as PIV or LDV has to be used. Moreover, it assumed that the turbulence intensity of the supply in the Fri-Jado cabinet is relatively low, since a velocity at supply of 0.35 ms^{-1} at the supply was measured with a hot-sphere anemometer. On the other hand, the shape of the supply velocity profile can be an interesting parameter for optimization purposes and will therefore be used in this study.

The deflection modulus can be used as a design parameter to reach the maximum effectiveness of the air curtain. The deflection modulus is defined by (Hayes & Stoecker, 1969) [40]

$$D_M = \frac{\rho_{amb} b u_{jet}^2}{g H_f^2 |\rho_{cons} - \rho_{amb}|} = \frac{b u_{jet}^2}{g H_f^2 \left(\frac{T_{jet}}{T_{cons}} - \frac{T_{jet}}{T_{amb}} \right)} \tag{14}$$

Where H_f is the frontal opening height of the cabinet as shown in figure 2. From equation (14) it is evident that a difference in density between the conservation space and surroundings and the momentum of the air curtain supply are the driving forces for deflection of the air curtain. If the density difference between the ambient and the conservation space decreases and the momentum of the supply supply remains constant, the deflection modulus will increase and the deflection (or bending) of the air curtain will decrease. Figure 16 shows a chart that was made by [40]. The chart depicts the deflection modules as a function of the ratio between the frontal opening height H_f and initial air curtain thickness b_0. Using this chart, one can determine the minimum supply velocity needed for supply, in order to guarantee an unbroken air curtain. However, because for this velocity the air curtain is borderline stable, usually a safety factor between 1.3 and 2 is applied to the deflection modulus.

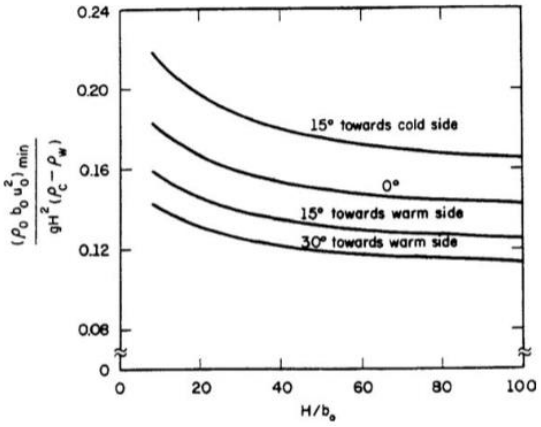

Fig. 16. Minimum outlet momentum required to maintain an unbroken air curtain. The different angles depicted for each line are the throw angles, which are discussed next. Adapted from Foster et al., (2006) [41].

On the other hand, Foster et al. (2006) [41] showed with experimental testing that the predicted optimum supply velocity of this chart wasn't very accurate. During experimental testing, they found that a safety factor of 2.2 gave the highest air curtain effectiveness. Finally, Gonzales & Kaye (2021) [42] used their theoretical model of thermal entrainment in a jet stream to calculate that an optimum air curtain effectiveness is reached for a deflection modulus of 1.26 times the critical deflection modulus. Therefore, no agreeable optimum value for the safety factor of the deflection modulus was found in literature. Because of the uncertainty for the optimum value of the safety factor, the deflection modulus will not be further used for this study.

Additional design parameters that were suggested by [38] are the offset angle γ (the angle of the supply with respect to the return) and the throw angle λ (the angle of the supply with respect to the vertical). The throw angle is equal to

$$\lambda = \gamma \pm \delta(\pm) \tag{15}$$

where δ is the angle shown in figure 17. Note that the sign in equation (14) is negative for $\delta(-)$ and positive for $\delta(+)$. The final design parameter mentioned in literature is the height of the opening over the air curtain width $\frac{H_f}{b}$. Note that for this study only the initial air curtain width b may be altered and not the frontal opening height H_f, due to design requirements.

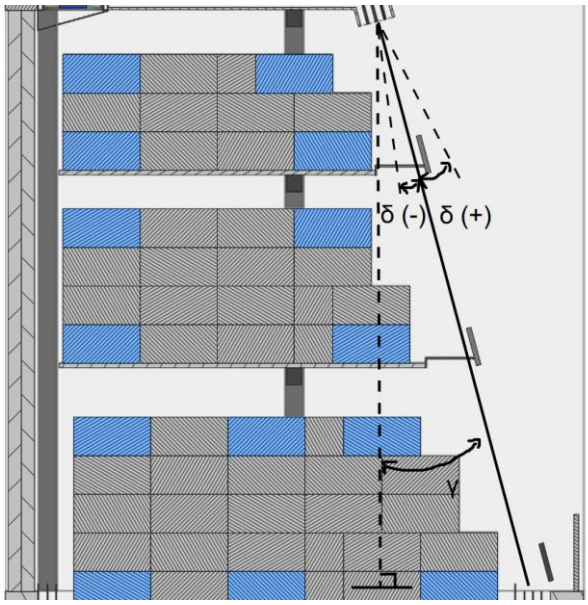

Fig. 17. Illustration of the offset ($\boldsymbol{\gamma}$), negative deviation of the throw angle ($\boldsymbol{\delta}(+)$) and positive deviation of the throw angle ($\boldsymbol{\delta}(-)$).

In the study of [38], a linear or quasi-linear trend was found between the infiltration ratio and the offset angle, while no specific trends were found for the other geometric parameters and the infiltration ratio. However, note that a different cabinet that included a PBP was used for this study, which differs from the Fri-Jado cabinet. Therefore, this relationship may not be valid. Nevertheless, altering the throw and offset angles would be an easy modification for optimization purposes. Therefore, these angles will be used as performance parameters.

In conclusion, the IR camera can be used to qualitatively evaluate the temperatures of the air curtain and the M-packages. In addition, multiple design parameters retrieved from literature were discussed and reviewed. The thermal entrainment ratio and infiltration rate can be helpful in assessing the performance of the cabinet in its current configuration (by simulation or experiment). Moreover, different Richardson numbers and Reynolds numbers will certainly affect the performance of the cabinet as well as different throw and offset angles. Table 2 shows an overview of the reviewed design methods / performance parameters that will and will not be further used in this study.

Table 2. Listed performance parameters that will be used in this study

Performance parameter	Symbol	Will the performance parameter be used?
Thermal entrainment ratio	α_T	Yes
Mass entrainment ratio	α_M	Yes
Richardson number	Ri	Yes
Reynolds number	Re	Yes
Turbulence intensity	I	No
Offset angle	γ	Yes
Throw angle	λ	Yes
Deflection modulus	D_M	No
Height over width ratio	$\frac{H_f}{b}$	No

2.4. The physics of the air curtain

In this section the physics of the air curtain are discussed. Experimental tests were performed to get a more specific picture about the entrainment of the air curtain. Because the main component of the thermal loading is mainly due to the thermal entrainment, only the frontal air curtain is considered.

2.4.1. Description Of The Air Curtain

Since the trajectory of the air curtain is mostly over solid M-packages and each slot of the supply has a rectangular opening, the air curtain can be modelled as a plane wall jet. For simplicity, the crossflow that is applied in the climate chamber is neglected. Moreover, only a single slot is considered.

Measurements with a hotwire anemometer (Testo 425) near the supply were performed. The averaged mean velocity that was measured is equal to approximately 0.35 $\mathrm{m\,s^{-1}}$, resulting in a Reynolds number of about equal to 1000. This indicates that the air curtain is initially laminar. Figure 18 shows the development of a turbulent plane isothermal wall jet. The jet flow is retarded on one side by the wall and on the other side by the quiescent fluid. The boundary layer that is formed on the wall is defined as the distance between the wall and the maximum velocity U_m. Both the boundary layer and the air curtain thickness increase approximately linear. When temperature effects are considered, buoyancy starts to play an important role in the shape of the air curtain and velocity profiles. As opposed to the isothermal case, the ejected air in the air curtain starts to accelerate because it has a lower temperature than its surroundings. The buoyant acceleration decreases with the streamwise direction of the air curtain, due to the thermal loading of the environment. Because the direction of the buoyancy force opposes the direction of the gravitational force, the air curtain is known as a buoyant jet. In addition, due to a density difference between the environment and the conservation space, a buoyancy force will push the curtain towards the conservation space. Besides buoyancy, the second force that can play an important role in the structure and development of the jet is the momentum force, caused by the fans upstream of the air curtain. One can make use of the Richardson number as described by equation (7) to determine which force is dominant. Assuming a jet temperature equal to 3 °C a Richardson number of 0.25 is calculated, indicating that both forced and natural convection play an important role in the air curtain flow.

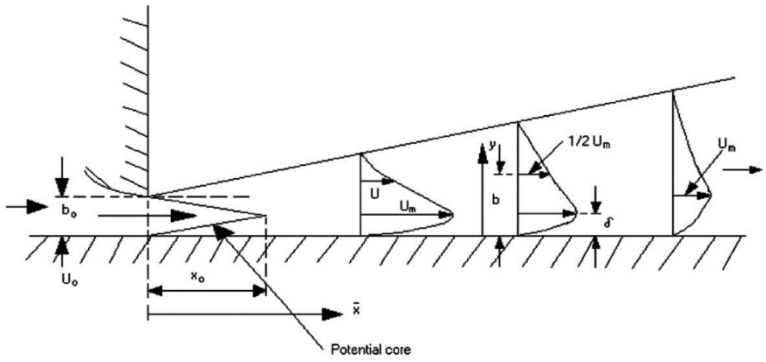

Fig. 18. Sketch of a turbulent plane isothermal wall jet. Where b_0 is the slot width, $\mathbf{U_0}$ the initial velocity, x_0 the potential core length, U_m the maximum velocity, δ the boundary layer and y and $\bar{x}$ spatial coordinates. Adapted from Sekula & Redondo (2008) [44].

The jet flow initially has a laminar irrotational potential core. However, due to friction with the quiescent fluid surrounding the jet, an inflection point in the air curtain velocity profile causes the Kelvin Helmholtz instability, with the consequence that vortices and turbulence are generated, dissipating the potential core of the jet. (Blevins, 1984)[43]. Due to the vortices, air from the ambient is suctioned in (the air is entrained) and the jet starts to grow.

In addition, intermittent turbulence can be observed for a real jet nearby the air curtain/ surroundings interface.

2.4.2. Infrared Imaging Of The Entrainment

To get a picture of the entrainment, infrared thermography was applied using a FLIR T200 camera in combination with a Perspex frame covered with zinc spray. The reflective temperature was set to 25°C, which is about equal to the climate room temperature. In addition, the infrared camera was tested for accuracy by using a calibration tape with an emissivity of 0.95 at 25 °C, which showed no strange temperature deviations. A CAD drawing of the frame is shown in figure 19. The frame was placed in-line with the thermocouples that were inserted into the M-packages, to create a 2D picture. Moreover, the emissivity of the zinc spray was calibrated with calibration tape with an emissivity of $\varepsilon = 0.95$. The calibrated emissivity of the grey zinc spray was consequently equal to $\varepsilon = 0.87$. Each IR photo was edited in FLIR Tools to modify the temperature range accordingly. Results of the infrared measurements on the frame are shown in figure 20. The black lines were sketched in the picture to give an indication of the frame contours. One can see from figure 20 that the temperature gradient from the conservation space to the ambient in the middle of the cabinet is higher than on the sides, indicating that there is more thermal entrainment at these locations, as supported by [39].

As mentioned in section 2.2, the increased entrainment at the sides is most likely to occur due to the end wall vortices that are generated by the crossflow, that is imposed by the climate chamber. Therefore, it is certainly tempting to create a 3D simulation that can capture all the characteristics of the flow. However, before making this decision, one should take into account the computational resources needed for such a simulation. Nevertheless, obtained temperatures from the thermocouples in the thermocouple frame will be compared with a 3D simulation of the entire cabinet in the next chapter. In addition, the next chapter will discuss the importance of performing a 3D simulation in more detail. Finally, remark that there is some distortion in the images, which is due to the irradiation coming from the air guidance strips.

One downside of this measurement is that there are some gaps between the frame and the M-packages. Because the frame was designed to clamp the air guidance strips at the front, there are gaps that do not capture the temperature profile of the air curtain. The frame could have been extended more inward the cabinet, to capture more of the air curtain. While these statements are true, the frame does show a good qualitative picture of the spatial dependency on thermal entrainment for the air curtain. In these pictures, it is made clear that the sides of the cabinet suffer more from thermal entrainment, as one can observe smaller temperature gradient in the direction from the conservation space to the ambient with respect to the center. This indicates that a larger amount of mixing occurs at the sides, thus more air from the ambient is entrained.

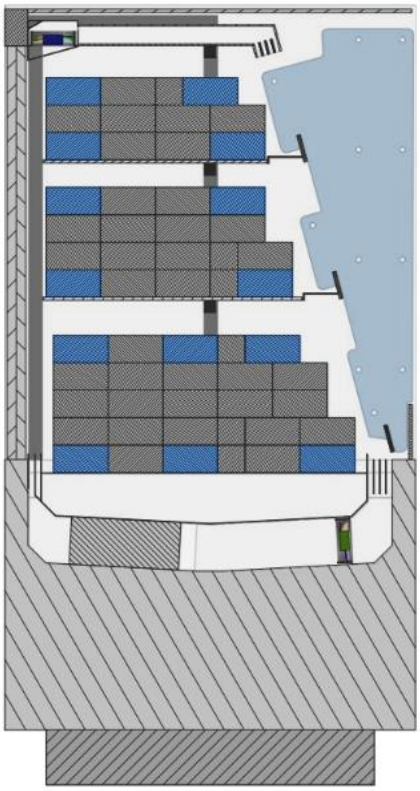

Fig. 19. IR frame design.

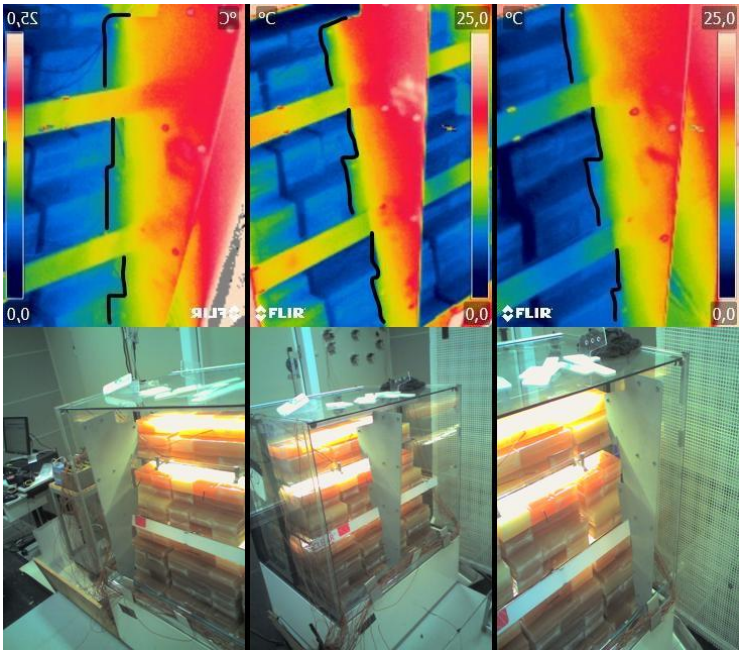

Fig. 20. Infrared images of the air curtain. The black line indicates the boundary of the frame. The temperature range varies from 0°C to 25°C. Note that the left IR picture is mirrored for better comparison with respect to the middle and right pictures.

In addition, infrared images were made of the M-packages, since these surfaces are expected to be mostly affected by thermal radiation [14]. By taking IR pictures of the bottom and top, left and right located M-packages, a qualitative view is made of the thermal loading on the frontal surfaces of the M-packages. The pictures were taken approximately perpendicular with respect to the frontal opening of the cabinet. The emissivity of the wrapper material of the plastic is equal to $\varepsilon = 0.9$ as specified by NEN-EN-ISO-23953-2. The results of the infrared images of the M-packages are shown in figure 21. One can see that the highest thermal loading on the M-packages is measured on the downstream side of the cabinet. As the external air current generated by the fans of the climate room travel downstream, more air seems to be entrained by the air curtain, which might be due to the crossflow.

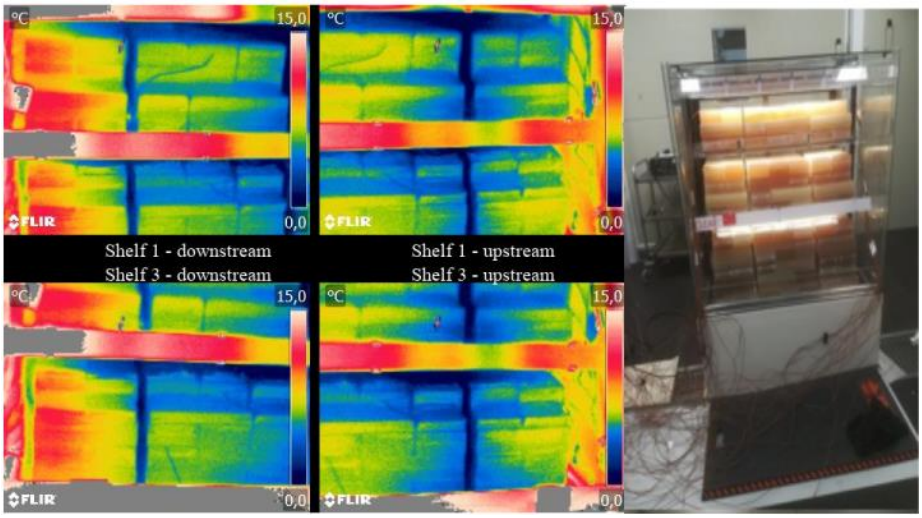

Fig. 21. Infrared images of the M-packages. The temperature range varies from 0°C to 15°C. In this figure, downstream and upstream refer to the direction of the external air current, generated by the fans of the climate room. The photo of the cabinet depicts the front view of the cabinet.

2.4.3. Thermocouple Temperature Profile Measurements In The Air Curtain

The temperature profile across the air curtain was measured by making use of the set of frames shown in figure 22. The frames were placed over different cross-sections in-line with the M-package thermocouple locations as well. In addition, the red dots represent the measurement locations where the thermocouples were inserted. Pictures of the frame can be seen in figure 23. To get a better picture of the interaction between M-packages and air curtain, additional thermocouples were used for the M-packages.

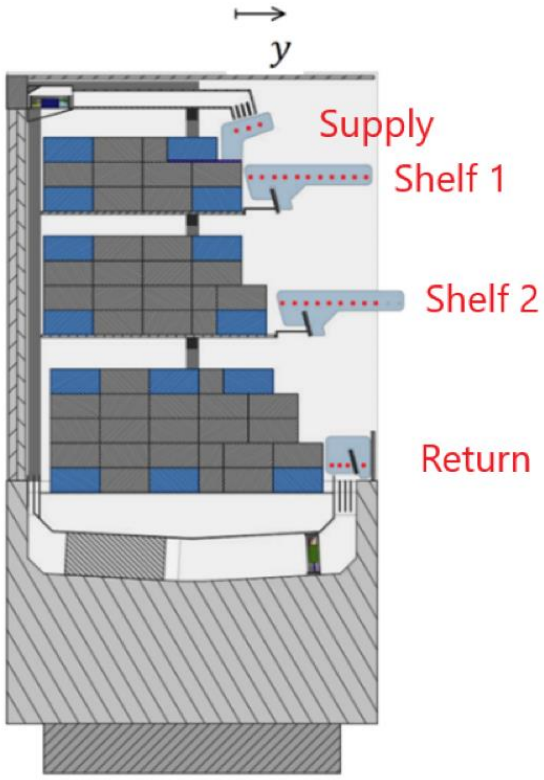

Fig. 22. The thermocouple measurement frame. Each red dot in the picture shows the location at which a thermocouple was inserted. The red dots are equidistantly spaced by 2.1 cm. The distance of the red dots in the top and bottom frame with respect to the supply and the return is 2.5 cm. Note that $\frac{\mathbf{y}}{\mathbf{b}} = 0$ at the far-left red dot.

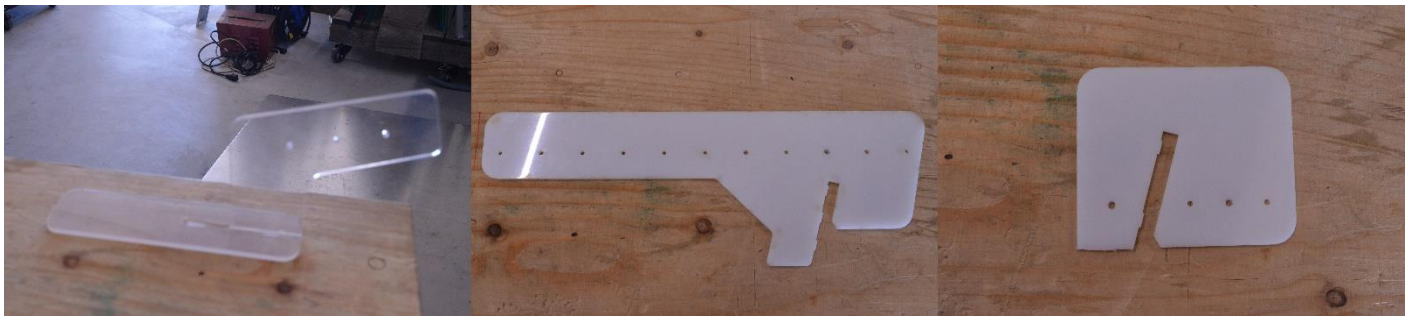

Fig. 23. The thermocouple frames produced for measuring the air curtain. From left to right: top frame, middle frame, bottom frame.

Figure 24 shows the temperature profiles that were measured with the set of frames. Note that figure 24 takes into account the offset of the placement of the frames. In addition, one can see that the highest temperature distributions are located at $\frac{x}{L} = 0.12$, again at the most downstream direction of the external air current, agreeing with the thermal images of the M-packages. Moreover, the frames positioned at shelf 1 and shelf 2 both converge to the ambient temperature, while the frames positioned near the supply and return don't. This means that more thermocouples for higher $\frac{y}{b}$ should have been placed to measure the entire temperature profile.

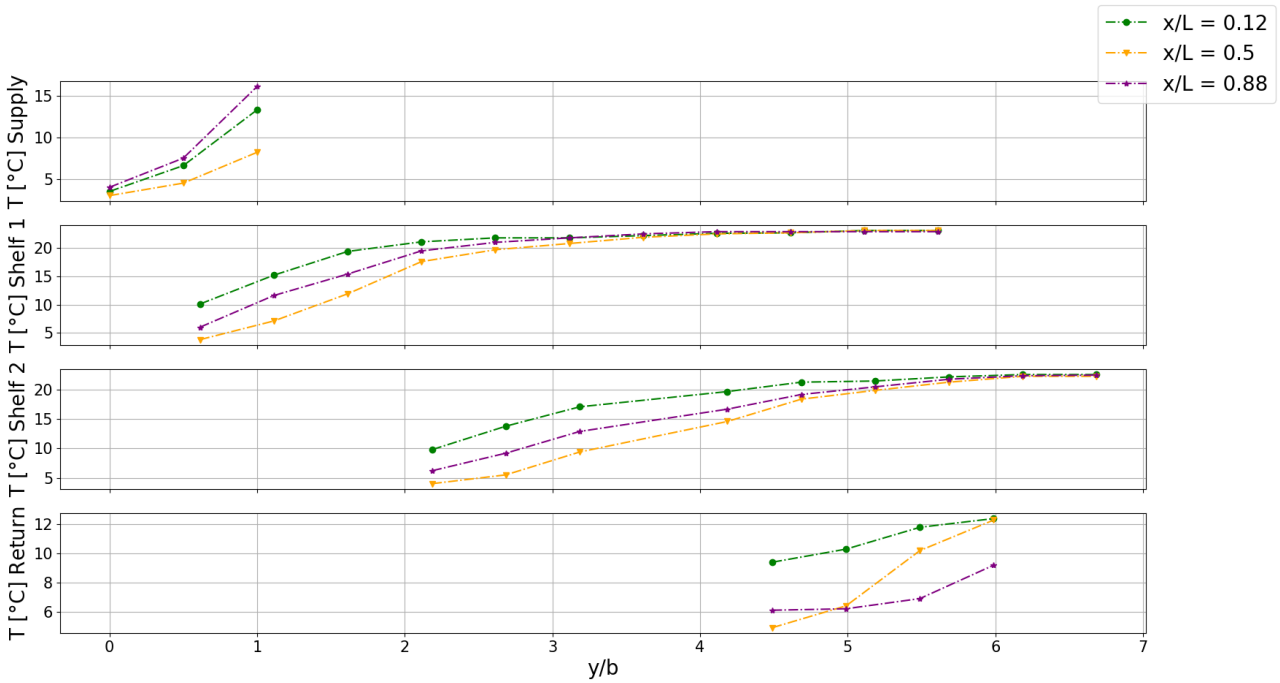

Fig. 24. Results of the temperature measurements using the set of frames shown in figure 22. The distance across the air curtain **y** is normalized with the slot width b. The different line colors indicate different locations with respect to the streamwise direction of the external air current. Refer to figure 10 for a better picture of the dimensionless coordinate $\frac{x}{L}$.

To get a final indication on the thermal entrainment, a thermocouple frame was used that positioned three thermocouples just outside the cabinet, at the height of the return, as shown in figure 25. For increasing $\frac{x}{L}$ the measured temperatures are: 15.6°C, 22.8 °C and 19.4°C, again showing that most cold air is spilled near the sides of the cabinet due to the increased entrainment. The supply temperature that was measured inside the supply is equal to 3.2°C.

In conclusion, it is shown that the air curtain can be represented as a buoyant jet, in which the driving forces are buoyancy and forced convection. Thermographic images and thermocouple measurements have shown the entrainment of ambient air in the air curtain, which is mostly present near the sides of the cabinet, showing that the thermal loading varies in all the three directions.

Fig. 25. Thermocouple frame that measures the spilled air temperature.

2.5. Additional Measurements

Additional measurements were performed during the experimental testing, to gather more data that could be of use for performing and evaluating the simulation. Table 3 shows the measurement tools that are in the inventory of Fri-Jado (FLIR, 2022; Testo, 2022; Atal, 2022)[45][46][47].

Table 3. Available measurement tools.

Name	Type	Quantity	Accuracy	Resolution	
FLIR T200	Infrared camera	1	2 °C	200 × 150 infrared	
Yokogawa	T-type thermocouple	58			
Testo 425	Thermal anemometer	2	0.03 m s^{-1}	0.01 m s^{-1}	0.1 °C
Atal ATV-11R	Temperature / humidity meter	2		0.1 °C	0.1% relative humidity
Ibiza	Fog machine	1			

2.5.1. Thermocouple Temperature Measurements In The Cabinet

Thermocouples were used to remeasure the M-package temperature distribution in the same configuration because during the previous test, the climate cell had clogged filters as mentioned in section 2.2.

Moreover, thermocouples were placed at the following locations described in table 4 and shown in figure 26, to measure air temperatures. In this figure, the thermocouples that have the number six assigned were used to measure the conservation space air temperature and were placed approximately in the middle for each shelf. Thermocouples with numbers 1,2 and 3 were placed inside the grilles, because over here the air was mostly mixed. Thermocouples with numbers 4 were attached to the BRAG inlet grille with tape, because these thermocouples could not be placed inside the grille since the fans were located over there. All thermocouples were placed along the x-direction, in-line with the thermocouples that were inserted in the M-packages and were measured over a period of 24 hours. The results of these temperature measurements can also be retrieved from table 4.

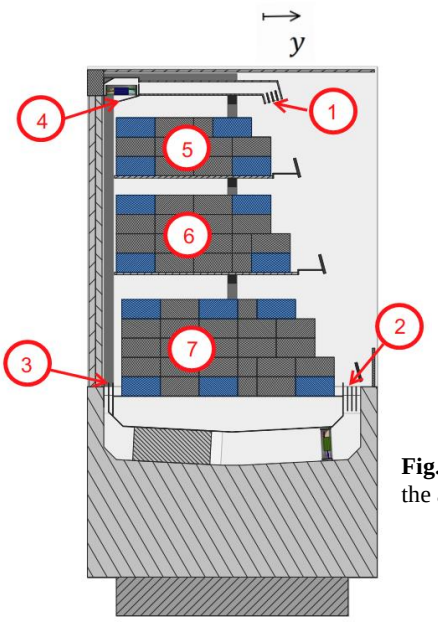

Fig. 26. Thermocouple locations, used for measuring the air temperature.

Table 4. Measured air temperatures of the discharge/ return grilles and of the conservation space for each shelf

		$\frac{x}{L}$					
		0.12		0.5		0.89	
Nr.	Property	Mean temperature [°C]	σ [°C]	Mean temperature [°C]	σ [°C]	Mean temperature [°C]	σ [°C]
1	supply	4.4	0.1	3.2	0.1	2.9	0.1
2	return	6.5	0	7.7	0	9.6	0
3	BDAG	-1.5	0.9	-2.8	0.5	-3.8	0.5
4	BRAG	3.1	0.2	0.8	0.6	1.7	0.3
5	Shelf 1	3.5	0.1	1.5	0.2	1.7	0.1
6	Shelf 2	3	0.1	0.6	0.7	4.7	0.1
7	Shelf 3	2.7	0.1	1.4	0.3	2.1	0.1

2.5.2. Hot-sphere Anemometry

Average velocities have been measured with the testo 425 hot-sphere anemometer at the same locations as the thermocouples in the top and bottom frame shown in figure 22. In addition, velocities were measured 2.5 cm from the BDAG and BRAG in the same planes as the frames, positioned approximately in the middle with respect to each grille. Each velocity was calculated by calculating the temporal average of 1 hour in between the defrosting cycles. The goal of these measurements was to get a reference with respect to the simulation, boundary conditions or for the use of the design parameters mentioned in section 2.2.

As mentioned in section 2.3, it is clear that more advanced measurement tools are needed to get a good indication of the turbulence intensity. The Testo 425 is only able to measure an average velocity since its response time is too slow to record velocity fluctuations caused by turbulence.

2.5.3. Relative Humidity Measurements

To gather further information for the boundary conditions of the simulation, relative humidity measurements were performed. One of the measurement locations are the centered red dots in the frames near the supply and return as shown in figure 22. Finally, the relative humidity was measured just behind the evaporator, at location 3 in figure 26.

2.5.4. Climate Chamber Measurements

During testing the temperature and relative humidity were measured as described in 2.2. Table 5 shows the measurement results of the climate chamber. It can be seen that the simulation is slightly lacking the 3M1 requirements. However, for the purpose of the simulation, these results will be used as boundary conditions.

Table 5. Measured room temperatures

Property	Unit	Mean value	Standard deviation
T_{CC}	°C	23.7	0.33
RH_{CC}	%	52.3	1.14

2.5.5. Fog Machine Test

During the experimental testing a Fog Machine was used to qualitatively describe the flow of the air inside the cabinet. Figure 27 shows the experimental setup. This test was repeated for a loaded and unloaded cabinet as a comparison. The smoke machine was placed approximately 0.5 meter away from the frontal opening of the cabinet and smoke was discharged for approximately 5 seconds. Smoke movement inside the cabinet was recorded during the tests from the side and the top of the cabinet with a digital camera, to get a clearer picture of the air movement in each direction. To better highlight the smoke,

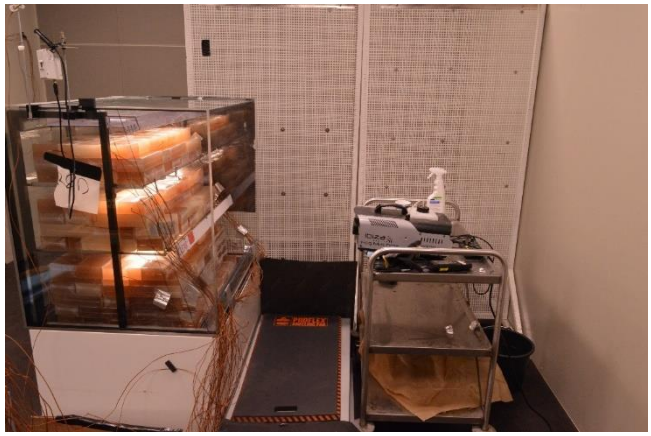

Fig. 27. Experimental setup of the fog machine test.

black coverage was placed on top of the air deflector and on the sides of the cabinet.
Figure 28 shows the top and side view of the cabinet. Unsteady air curtain fluctuations were observed in the y-direction, especially near the supply. Moreover, because the air discharged at the supply is a buoyant jet, the air curtain spreads causing the air to not be completely conducted in between the air guidance strips and shelves, finally leading to air spillage at the height of the return. In addition, air spillage is partly suspected to be coming from the increased momentum caused by cold air that is conducted from the back to the front. The air in the conservation space is coldest neighboring the BDAG, which is nearest to the evaporator. Because of its higher density most cold air is circulated to the air curtain at the bottom part of the conservation space.
While cold air enters the conservation space from the BDAG, air coming from the air curtain and surroundings enters the conservation space from the other side. From the top view of figure 28, a vortex outside the cabinet nearby the upstream side wall adjacent to the frontal opening plane was visible, which is also described by [20]. Nearby the downstream sidewall, air seemed to be less affected by a vortex, while only bending into the streamwise direction of the external air flow.

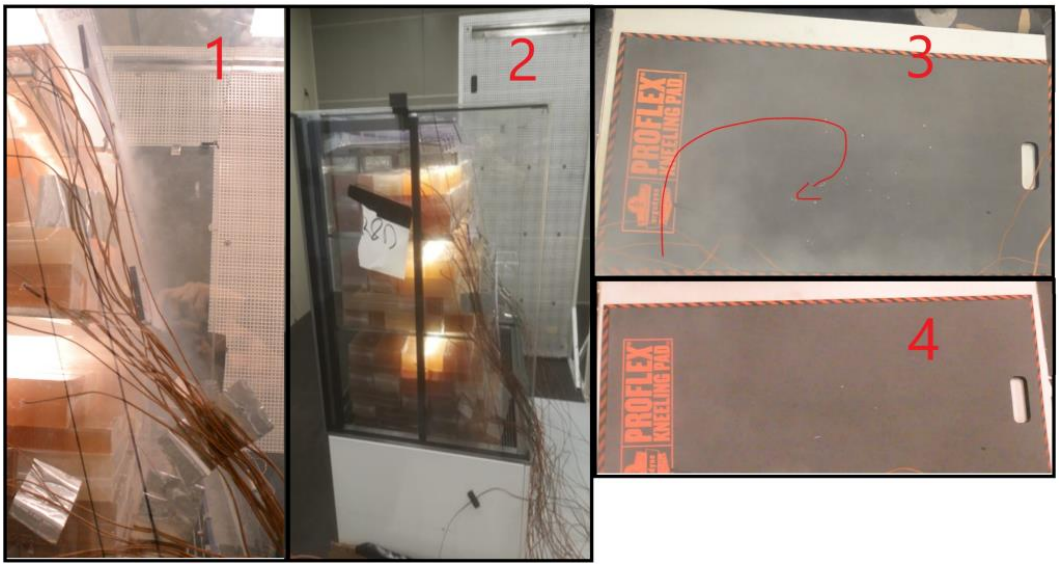

Fig. 28. Sideview and top view of the smoke test (1 – sideview with smoke; 2 – sideview with no smoke; 3 – topview with smoke; 4 – topview with no smoke). Note that the top view depicts the air that exits the frontal opening above the air deflector.

2.5.6. Discharged Condensate

The discharged condensate was measured to get an indication on the amount of ambient air that infiltrates the cabinet. It is important to remark that most of the condensate is discharged during the defrosting cycle. Therefore, the measurement started and ended at the beginning of a defrosting cycle. The condensate was collected over a period of 21 hours or 7 defrosting cycles. On average, 0.066g/s of condensate was discharged. Assuming an enthalpy of condensation equal to 2250 $\frac{J}{g}$, the latent heat load to condensate the water vapor present in air equals approximately 150W, which is significant considering the fact that the average refrigerating power in the cabinet is about equal to 650W.

2.6. Final Remarks

Some of the design parameters that were discussed in section 2.3 were calculated based on the values that were measured in the experiment. Each performance parameter with it corresponding value is listed in table 6. These obtained values can be used as a reference for the simulation.

Table 6. Calculated design parameters based on the experimental measurements

Performance parameter	Symbol	Value
Thermal entrainment ratio	α	0.22
Richardson number	Ri	0.25
Reynolds number	Re	1000
Condensate discharge	β	0.066 g/s
Offset angle	γ	15°
Throw angle	δ	15°
Height over width ratio	$\frac{H_f}{b}$	17

In addition, further information that is available for the acquired data, such as the velocity and relative humidity for the air curtain and wall temperatures can be found in appendix B. The figure in appendix B also clearly shows that temperatures of the air curtain are higher nearby the sidewalls, which again confirms the previous findings with regard to thermal entrainment. This effect appears to also happen in between the BDAG and BRAG looking at these temperature plots. Finally, the measured M-package temperature data and more specific thermocouple locations can be retrieved in appendices C and D.

3. Review of Previous Simulations related to Air curtains

It is known that there are several important choices to be made when performing a simulation, such as the temporal dependency, if the simulation should have a 3D or 2D domain etc. In addition, many different researchers have performed simulations on similar cabinets. Moreover, Simscale also performed a 3D simulation of the Fri-Jado cabinet. Therefore, this chapter aims to further investigate these simulation setup decisions that have to be made by reviewing the simulations retrieved from literature and the simulation provided by Simscale.
The importance of temporal dependency of the simulation is discussed in section 3.1, the relevance of performing a 3D simulation in which the effects of implemented turbulence models are taken into account is discussed in section 3.2, a review of benchmark tests that were previously performed by Simscale are discussed in section 3.3 and options for demarcation of the flow domain are discussed in section 3.4.

3.1. The Importance Of Temporal dependency

[20] compared multiple simulations that took into account the conservation space, air curtain and ambient for a cabinet. These simulations were a 2D steady-state simulation, a 2D transient simulation and a 3D transient simulation. They concluded that their 2D steady-state simulation gave qualitative poor results, while their 2D transient simulation captured some more physical flow features such as transient larger scale vortices. Finally, they concluded that their 3D transient simulation gave a more reliable prediction of the air curtains flow pattern, having an 8W difference in refrigeration power with respect to their experimentally obtained refrigeration power. While the result for the refrigerating power looks accurate, no advanced measurements were performed that capture the velocity field or temperature field of the domain, giving no validation to whether the computed temperature field and velocity field is accurate. Therefore, it is not clear whether the performed 3D transient simulation represents reality.
A transient simulation has the advantage that it includes large scale fluctuations in the air curtain, where a steady-state model only accounts for thermal entrainment by small scale turbulent diffusion. As mentioned before, the M-packages in the cabinet never reach a true steady-state and stay within a temperature window of 0.5°C during the stable period. In addition, the air curtain clearly showed transient behavior during experimental testing.
Computing a transient simulation while maintaining a constant time step can prove to be difficult due to the temporally changing flow field. In such cases the Courant number provides help. A simple definition of the Courant number is

$$\mathrm{Co} = \frac{\mathrm{U}\Delta\mathrm{t}}{\Delta\mathrm{x}} \tag{16}$$

Here, a courant number smaller than 1 indicates that the distance a fluid travels in a single time step, doesn't exceed the size of a single mesh cell. The Courant number can be used for automatically determining the size of the time step, in order to avoid a diverging solution [26]. However, it might take considerable computational resources if the mesh size is small. Despite the fact that transient simulations give a more accurate solution of the cabinet, there are multiple studies that have shown that a steady state simulation is sufficient for optimization purposes. In these studies, a 2D steady-state model was developed for a cabinet. These results showed that the refrigeration power deviated by 13.6% with respect to the experimentally obtained values (Artico, Mousset & Fortini, 2008) [48][10]. While these deviations for the refrigeration power are significantly more than for the 3D transient simulation performed by [20] (which was only a 0.29% deviation), it still is an acceptable result for optimization purposes. Moreover, transient simulations have to converge for each timestep, which typically require more time (Smale, Moureh & Cortella, 2006)[49]. Besides, a steady state solution only generates a single solution of the flow field, while a transient generates solutions for multiple time steps. Considering the CFD optimization process, ease of use and efficiency, a single solution is much easier for getting a structured overview than when one has to analyze multiple solutions for different timesteps. Therefore, a steady-state simulation will be performed first and compared with experimental results. If this simulation is not satisfying enough for optimization purposes, a transient simulation will be designed.

3.2. The Importance Of A 3D Simulation

Another 3D simulation that was performed by [27], compared the effect of using air guidance strips, with the effect of no air guidance strips. The simulated domain consisted of the entire simplified cabinet geometry, including a crossflow according to NEN-EN-ISO-23953-2. Note that the simulation was not experimentally validated. Therefore, one can assume that it is hard to get a proper validation of a 3D simulation of a cabinet.

Finally, a 3D conjugate heat transfer simulation of the cabinet, without crossflow was performed by [23]. The flow domain of the simulation is shown in blue in figure 29. One downside of the use of Simscale is the fact that the built-in code that is used, is not visible for the user. Therefore, the process of assessing the Simscale software is limited. The 3D model was generated using an unstructured grid that consisted of both tetrahedral and hexahedral elements. The used turbulence model is $\mathbf{k-\omega\ SST}$, which is a combination of the $\mathbf{k-\omega}$ model (for near wall treatment) and the $\mathbf{k-\varepsilon}$ model (turbulence models are further discussed in section 4.5). While it is known that the air is initially laminar (as mentioned section 2.4), it is also known that in general RANS models are more adapted to fully developed turbulence profiles. Moreover, the production term in the $\mathbf{k-\varepsilon}$ model only takes into consideration the mean flow gradients, neglecting velocity fluctuations caused by the Kelvin Helmholtz instability. Therefore, the underprediction of the turbulent production can lead to inaccuracies when using a RANS turbulence model (Moureh & Yataghene, 2017) [50].

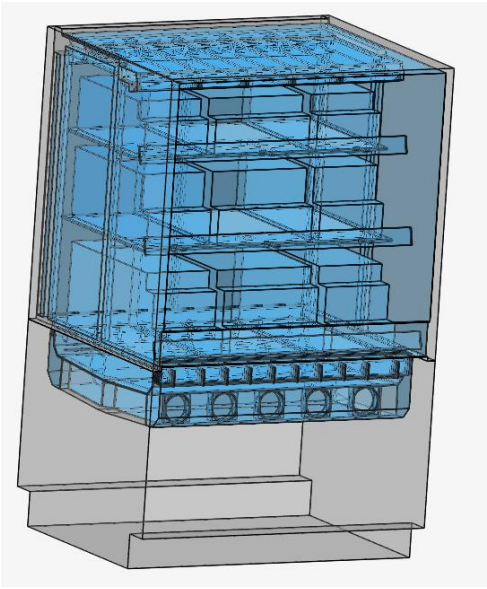

Fig. 29. The domain used for the simulation performed by Simscale, as indicated by the blue colored regions.

3.2.1. Comparison of simulated and experimental M-package temperatures

As mentioned before, Simscale performed a 3D simulation of the cabinet, using the geometry shown in figure 29. Additional M-package temperature measurements were performed according to NEN-ISO-23953-2 to obtain a new dataset for a climate chamber that was not affect by the clogged filter problem mentioned in sections 2.2 and 2.5.1. However, it has to be mentioned that during the M-package temperature measurements an older version of the BDAG was used, that did not include the inclined compartments (figure 7) which lead to a reduced cooling performance of the cabinet with respect to the M-package temperature measurements described in section 2.2.

The no-slip boundary condition in combination with a fixed heat flux was prescribed to the outside walls. For the inside walls, the no-slip boundary condition in combination with a fixed temperature was used. In addition, a natural convection boundary condition was applied to the frontal opening plane, which is a built-in boundary condition available in Simscale. Finally, a constant momentum source was applied to the top and bottom fans and a constant heat sink was applied to the evaporator, which was modelled using a porous medium model. The heat sink was assigned a value of 600W, based on the average heat transfer of the evaporator.

The simulated M-package temperatures were compared with the experimental testing and are shown in figures 30 and 31. One can see that for some subplots, the temperature distributions are qualitatively comparable. E.g. in figure 31 the temperature changes in a similar fashion for increasing $\frac{\mathbf{x}}{\mathbf{L}}$, when comparing simulation to experiment. The same change can be observed for different subplots in figures 30 and 31.

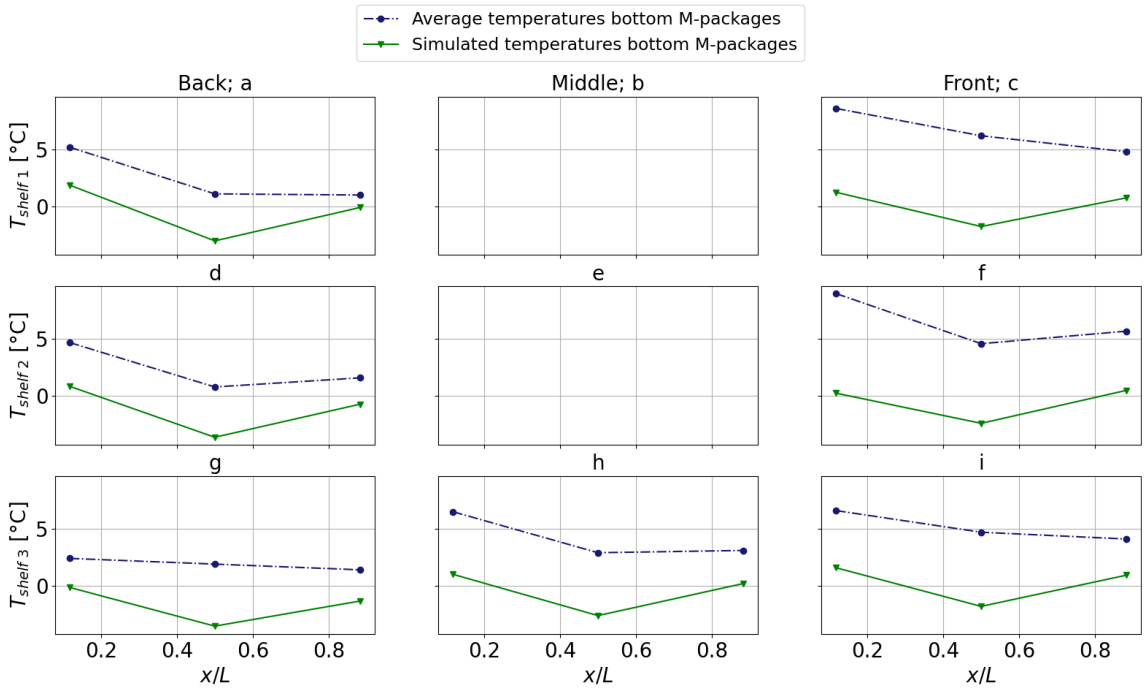

Fig. 30. Temperature distribution of the bottom M-packages located on each shelf field (see figure 10 for more information about the coordinate axis). The blue line represents the experimental values and the green line represent the simulated values. Each marker in the plot represents the temperature that was measured with a thermocouple in the center of a M-package. Note that the upper two graphs in the middle are empty because no thermocouples were placed for these M-packages.

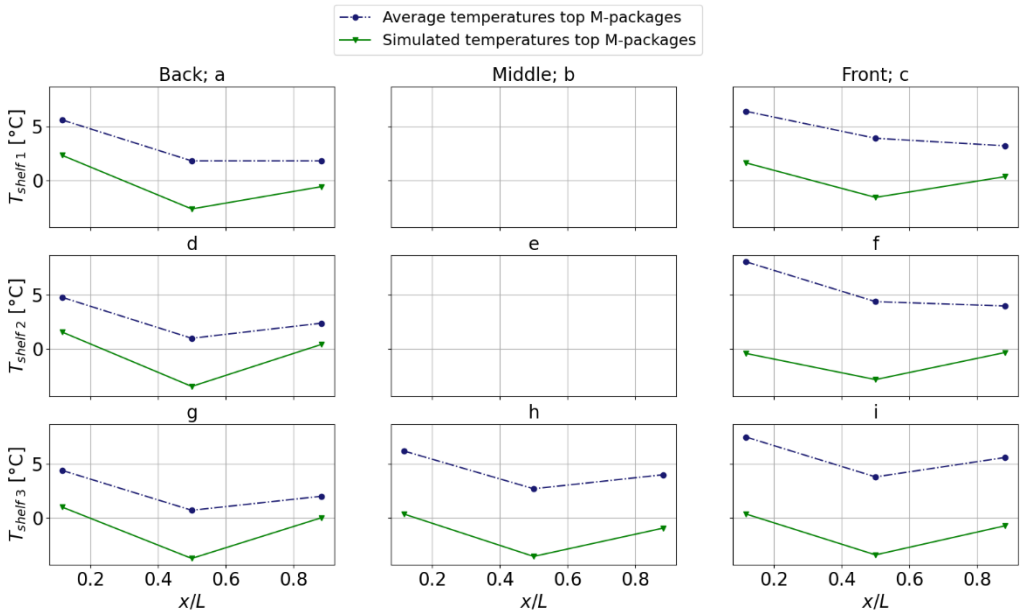

Fig. 31. Temperature distribution of the bottom M-packages located on each shelf field (see figure 10 for more information about the coordinate axis). The blue line represents the experimental values and the green line represent the simulated values. Each marker in the plot represents the temperature that was measured with a thermocouple in the center of a M-package. Note that the upper two graphs in the middle are empty because no thermocouples were placed for these M-packages.

In addition, figure 32 shows a comparison of the simulated temperature profiles of the air curtain and the measured temperature profiles that were discussed in section 2.4.3. When studying this figure, one can see that the best agreement between simulation and experiment is found for shelf 1, where the shape of the temperature profile is predicted somewhat correctly. However, it has to be emphasized that the temperature gradient for the simulation results is much steeper than the obtained experimental results, indicating that the cooling performance of the air curtain is overestimated. The temperature profiles for shelf 3 seem only to agree in a qualitative sense, looking at the shape of

the temperature distribution, but again the error is large. Finally, shelf 2 and the supply show no agreement between simulation and experiment, since the shape of the temperature distributions are not of similar shape.
In conclusion, by making a step-by-step comparison from the supply to Shelf 3, the qualitative agreements between simulation and experiment vary somewhat randomly (i.e. bad agreement for the supply, okay agreement for shelf 1, bad agreement for shelf 2, bad agreement for shelf 3). To improve the accuracy of the air curtain temperatures one could decouple the flow domain, which is further discussed in section 3.3.
As mentioned before, no velocity measurement tools with a high enough resolution were available in order to compare experimental and simulated velocity profiles, making the comparison incomplete. Besides, remark that significant assumptions were made during the setup of the simulation, such as a constant momentum applied by the fans and a constant amount of heat exchanged by the evaporator.

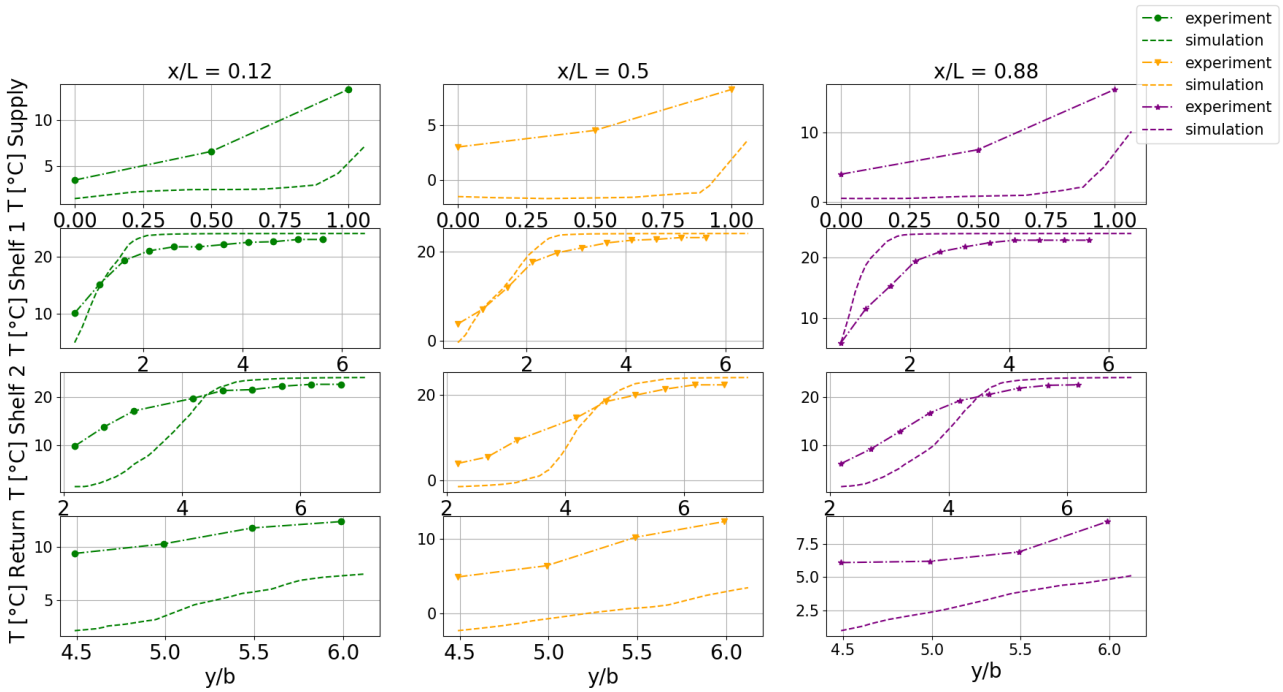

Fig. 32. Comparison of simulated and experimental air curtain temperature profiles, by making use of the thermocouple measurement frames which are shown in figure 22. Each row of subplots represents the supply, Shelf 1, Shelf 2 and the return, while for each column the temperature is plotted versus the y coordinate (The y axis can be retrieved in figure 2) normalized by the slot width b.

3.2.2. Comparison Of A 3D Large Eddy Simulation (LES) And The Simscale Simulation

[50] attempted to make a 3D transient simulation in combination with a Smagorinsky-Lilly LES turbulence model, for an experimental scaled down isothermal air curtain with a crossflow. The results of the simulation were compared with PIV and LDV measurement results. The domain is shown in figure 33. The LES simulation showed excellent agreement between the simulation and the experimental results for the initial jet profile, the halfwidth growth of the jet and the jet decay rate of the maximum streamwise velocity. However, more downstream of the air curtain (in x-direction) only a reasonable agreement was achieved for the jet velocity profile and the airflow patterns. Moreover, the root mean square values of the velocity fluctuations were only partly in qualitative agreement. In conclusion one can say that the simulation of a scaled down isothermal air curtain has at least partially the ability to quantitatively represent the experimental case. In spite of this, no temperature effects were captured which is necessary for the studied air curtain. Furthermore, a total amount of 1.253520 million cells were needed to perform the simulation, in order to resolve an acceptable number of eddies generated in the flow field. Therefore, one can imagine that in order to resolve an acceptable number of eddies for the entire cabinets flow field, a very large number of cells is needed for the simulation. As a comparison, it took 157.1 core hours to mesh and simulate a grid of 14 million cells in the 3D steady-state Simscale simulation. Taking into account these computational costs and the lack of accurate measurement techniques such as PIV or LDV, it proves to be a difficult and costly process to make an assessment of such a big simulation domain.

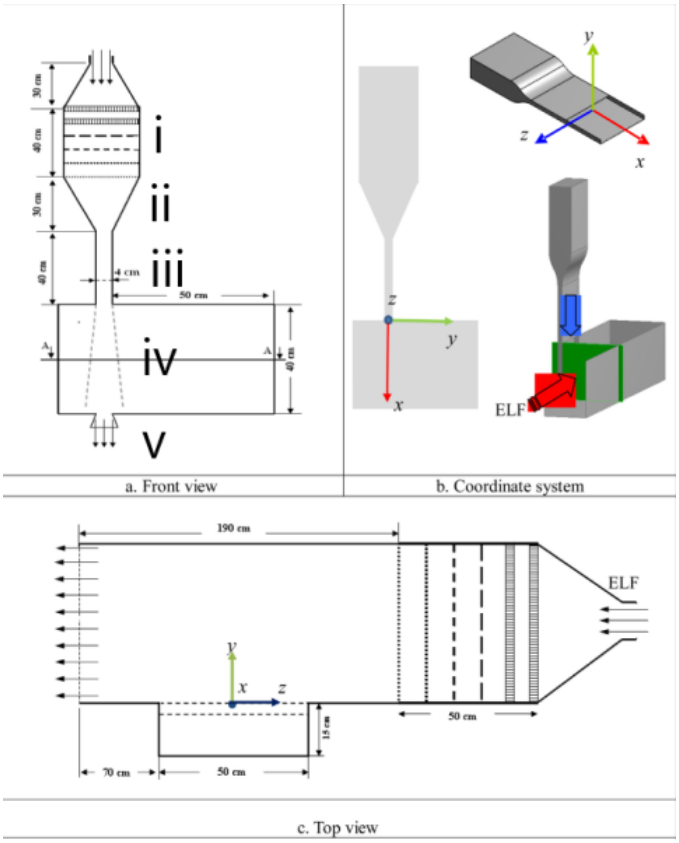

Fig. 33. a) front view of the domain, where i) is the settling chamber, ii) the smooth contraction nozzle, iii) the rectangular channel. Note that parts i), ii) and iii) are used to create the jet. Furthermore, iv) is the cavity and v) the jet exit. ELF is the external lateral flow (crossflow) applied on the air curtain and can be viewed from the top view c). Finally, the coordinate axes are shown in b). Adapted from [50].

3.3.3. Final Remarks On The Simscale Simulation

Even if this simulation would be accurate, it would be a highly expensive process of improving the cabinet (e.g. by assuming the 54 iterations needed to improve the cabinet as mentioned in section 2.2), taking into account the fact that Fri-Jado purchased a 10000 core hour package. In addition, no LES turbulence model is available in the Simscale package that was purchased by Fri-Jado. Therefore, the author will focus on performing a 2D simulation of the air curtain, using a RANS turbulence model.

While it is true that the simulation will become a more qualitative representation of the air curtain, the author believes that for the sake of optimizing the cabinet, using a 2D simulation is much more effective in the sense that the optimization will take less computational costs and time. Furthermore, Fri-Jado's product development has a busy daily schedule, in which other important jobs, such as CAD drawings have to be delivered by the end of the day. Hence, performing 2D simulations is also a much better fit for Fri-Jado looking at the daily work routine, the easier simulation setup and the reduced computational costs.

3.3. Demarcation Of The Flow Domain

To safe more computational costs, further demarcation of the domain can be considered. [9] decoupled the internal domain (PBP duct, fan & evaporator spaces) from the external domain (conservation space and surroundings), while Foster, Madge & Evans (2005) [51] went even a step further by only considering the effect of the air curtain on a single shelf.

The approach of demarcating the air curtain/ ambient domain from the internal domain eliminates the need for modelling the fan and has the advantage that less computational resources are needed, while not being constrained to a certain fan type. Moreover, it could increase the accuracy of the air curtain temperatures as mentioned in section 3.2.1.

On the other hand, inaccuracies can occur because parts of the cabinet are left out of the simulation which can have significant interaction with the demarcated domain. However, as argued in the previous section, the simulation will used for optimization purposes, which mitigates the importance of obtaining an accurate solution of the flow fields. Therefore, the supply will be used as an inlet and the return as an outlet, neglecting the evaporator space and fans. Because the flow domain is now greatly simplified, an easier validation of the simulation will be possible due to its reduced complexity. To implement this demarcation of the flow domain, new boundary conditions such as the velocities at the inlet and outlet grilles must be specified.

3.4. Benchmark Tests Performed By Simscale

To further assess the performance of Simscale, benchmark tests provided on the Simscale website were reviewed. While no validation cases for air curtains were present on the Simscale website, two interesting validation cases were found that had similarities to the physics that are involved in the air curtain. The investigated benchmark tests are shown in table 7 and are further discussed in this section.

Table 7. Interesting benchmark tests performed by Simscale. The reference was used by Simscale to validate their simulation.

Name of the benchmark test	Reference
Airflow in a data center	Wibron, Ljung & Lundström (2018) [52]
Buoyant flow: Natural Convection Between Heated Plates	Betts & Bokhari (2000) [53]

3.4.1. Airflow In A Data Center

The airflow in a data center is interesting because it involves the convection of air, which is also applicable for the air curtain. [52] compared the $\kappa - \varepsilon$ model with simulations that used more advanced turbulence models (Reynolds Stress Model (RSM) and Detached Eddy Simulation (DES)) and experimental results. The turbulence model that was used by Simscale for the validation is the $\kappa - \omega$ SST model. Figure 34 shows a 2D representation of the geometry of the problem. The 3D geometry is a rectangular space, containing four computer air conditioning (CRAC) units (C) and ten server racks (R). Each rack has a hot inlet and a cold outlet. For the CRAC units, a constant velocity and temperature were prescribed for the inlets and the outlets were fixed at a gauge pressure of 0 Pa. All walls were prescribed with a no slip and adiabatic boundary conditions. The comparison of velocity profiles for the line plot L1 at the cold inlet and the comparison of the velocity profiles for the line plot L5 that were obtained for the different turbulence models are shown in figures 35 and 36. From these figures, one can see that for L1 it looks like the $k - \omega$ SST performs best, while for L5 DES seems the most accurate. Note that only three data points were used for L1 and four for L5, which were measured with a hot-sphere anemometer. Due to the small number of velocity measurements, it is difficult to get a complete picture of the velocity profile. Therefore, the performed comparison is not very significant.

In general, it is known that more advanced turbulence models such as DES are more accurate than RANS turbulence models. By assuming that the velocity profile for L1 is a linear profile as depicted in figure 35, the $k - \omega$ SST, only predicts the change in velocity qualitatively. In addition, it must also be emphasized that a simplified geometry for the data center was used.

In conclusion, the comparison that was made, did show some qualitative agreement with the experimentally obtained velocities. However, a much better comparison would be obtained if more experimental data was available (e.g. more data for the temperature and velocity). Right now, this benchmark test is not very significant.

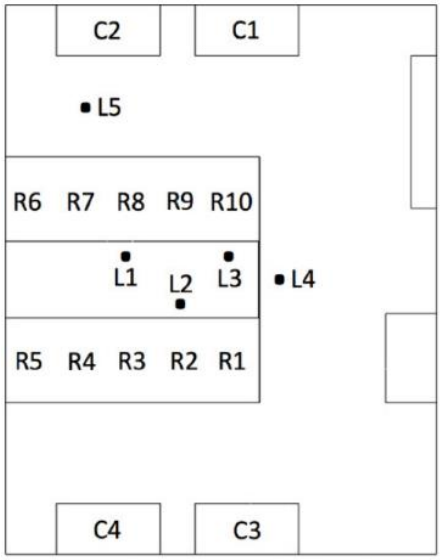

Fig. 34. Labeled CRAC units, server racks and measurement locations. Adapted from Wibron, Ljung & Lundström (2018) [52].

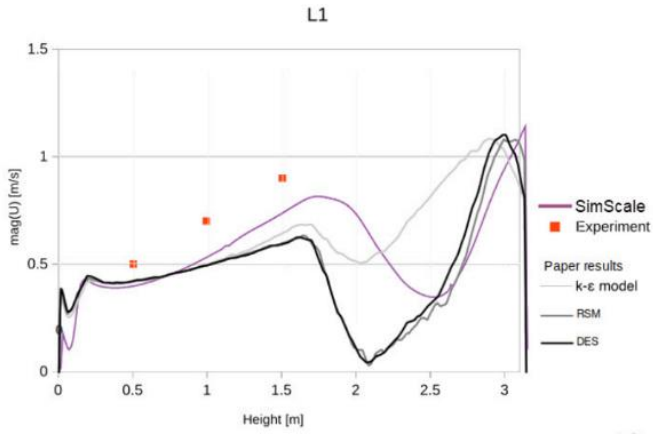

Fig. 35. Comparison of velocity profiles along lineplot L1 for different turbulence models. Adapted from Simscale [26].

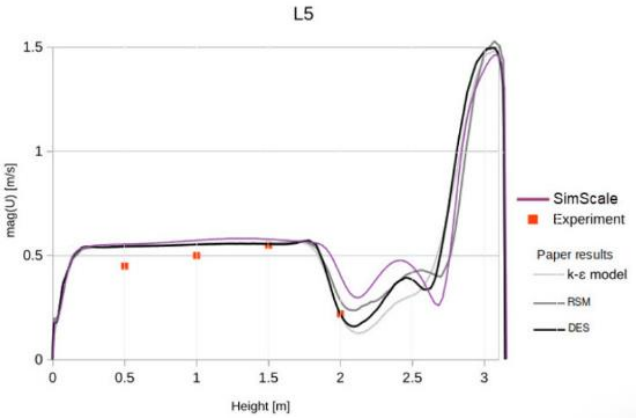

Fig. 36. Comparison of velocity profiles along lineplot L5 for different turbulence models. Adapted from Simscale [26].

3.4.2. Buoyant flow: Natural Convection Between Heated Plates

As experimentally determined in section 2.4, the air curtain is also affected by natural convection. Therefore, the typical benchmark test that involves turbulent natural convection between heated plates is reviewed in this section. The geometry that was used is again a rectangular space, although with different dimensions. The geometry with its coordinate axis is depicted in figure 37. The boundary conditions for this geometry are no slip walls with full resolution and fixed temperatures. The used turbulence model is the $k-\omega$ SST turbulence model.

The y-velocity profiles between the front and the back wall were experimentally measured by [53] for a Rayleigh number equal to $0.86 \cdot 10^6$. The simulated y-velocity profiles at the bottom ($y = 0.109\text{m}$) and at the top ($y = 1.09\text{m}$) were compared with the experimental measurements and are shown in figures 38 and 39. Finally, the temperature profile at $y = 0.109\text{m}$ was compared with the experimentally measured temperature profile and is shown in figure 40. All the figures show a reasonable agreement. One can see that near the walls, the prediction of the velocity profiles and temperature profiles become less accurate, which can be caused by the applied wall treatment. The topic of resolving the flow nearby the wall is further discussed in section 4.3 . Furthermore, no complete comparison was made for the temperature profiles at different heights, which is remarkable. Finally, note that the comparison was made for $Ra = 0.86 \cdot 10^6$. The Rayleigh number for the Fri-Jado cabinet was calculated to be equal to $971 \cdot 10^6$ being three orders of magnitude greater. Hence one cannot validate that natural convection is correctly predicted for such Rayleigh numbers. Finally, note that the Fri-Jado cabinet deals with mixed convection. Unfortunately, no benchmark tests that included mixed convection were performed by Simscale.

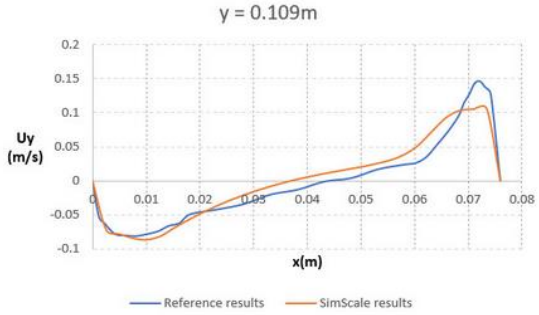

Fig. 38. Comparison of the velocity profiles at the bottom of the cavity. Adapted from Simscale [26].

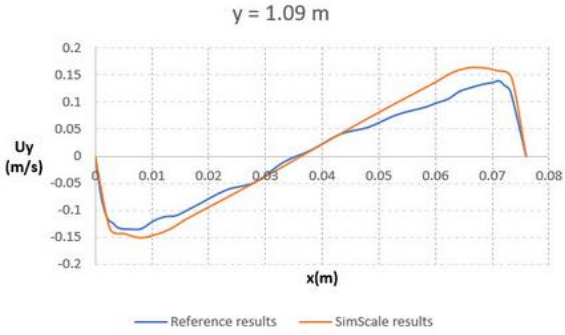

Fig. 39. Comparison of the velocity profiles at the top of the cavity. Adapted from Simscale [26].

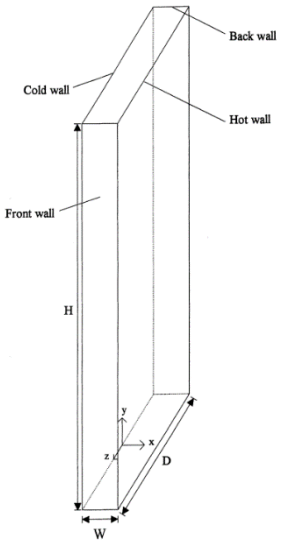

Fig. 37. Geometry for the benchmark test: Natural Convection Between Heated Plates. Adapted from Simscale [26].

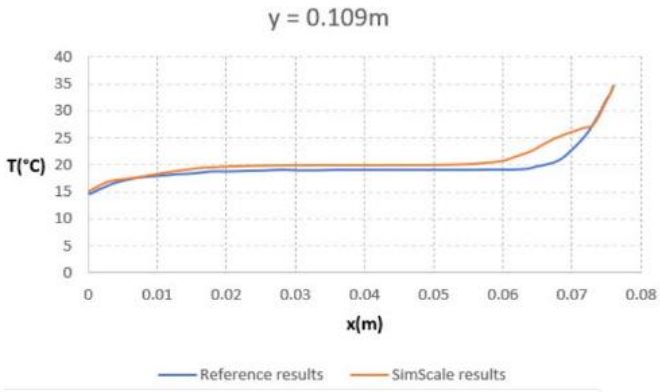

Fig. 40. Comparison of the temperature profiles at the bottom of the cavity. Adapted from Simscale [26].

3.5. Final Remarks

It has to be stressed that the physics of the air curtain of the case study cabinet are a mixed convection case. No mixed convection benchmark tests are available on the Simscale website. In addition, no literature was found that performed a mixed convection benchmark test of an air curtain, using Simscale. Therefore, additional benchmark tests for the air curtain will be performed with mixed convection in this study. Once these simulations are validated, a more representable CFD model can be designed. Before running these simulations, a more in depth look on the numerical methods in Simscale should be performed, to get a better picture of the discretization of the simulation.

4. Numerical methods In The Commercial Simscale Package

As mentioned in section 3.5, a more in depth look at the numerical methods will be performed to get a better picture of the discretization of the simulation. While it is known that Simscale integrates OPENFOAM® into their platform, no access to the built-in code was provided by Simscale due to commercial interests. Therefore, there is a limitation to the extent of knowledge on the built-in code that is provided in this section. Note that this section assumes a steady state incompressible flow for the air curtain. This assumption was made based on the conclusions made in the previous chapter.
The available mesh generators are discussed in section 4.1. The governing equations and finite volume method used for the discretization are discussed in section 4.2. The available methods for resolving the boundary layers are discussed in section 4.3, the relevant solvers in section 4.4 and the available turbulence models in section 4.5.

4.1. The Available Mesh Generators In Simscale

After the import of the CAD file into the Simscale platform is completed, the first step is to mesh the geometry. The mesh can be generated using three different mesh generators. The first mesh generator is called the standard mesh generator, which generates a 3D unstructured mesh. The second mesh generator is called the automatic Hex-dominant mesh generator. Finally, the third mesh generator is called the parametric Hex-dominant mesh generator. Both the automatic and parametric Hex-dominant mesh generator are based on the SnappyHexMesh mesh generator that is used in OPENFOAM®. SnappyHexMesh first creates a hexahedral tessellated box shaped mesh that surrounds the object that has to be meshed. Next, the box shaped mesh is modified iteratively by an algorithm that splits the hexahedral elements to better adjust the mesh shape to that of the object. The difference between the automatic and parametric hex-dominant mesh generators is the assignment of the mesh settings. In the automatic hex-dominant mesh generator the user only has to define the meshing mode (i.e. an internal mode for meshing inside the body and external mode for meshing outside the body), the mesh sizing, whether boundary layers have to be assigned automatically and finally the number of cores that are used for the mesh generation, which is further described in the next section. In the parametric hex-dominant mesh generator the user can define the number of cells in each direction for the box shaped mesh. In addition, this mesh generator provides features such as the max number of mesh adaptation iterations, the tolerance and custom boundary layer setup. Finally, also note that Simscale does not provide any other option for generating a 2D grid, besides setting the number of cells equal to one in the third direction for the parametric Hex-dominant mesh generator. The standard mesh generator creates an unstructured mesh that consists of tetrahedral and hexahedral elements. A tetrahedral mesh has the general advantage that it can be better adapted to a complex geometry than hexahedral mesh, while a hexahedral mesh is computationally less expensive. In addition, hexahedral elements are preferred over tetrahedral elements for boundary layer flows, because tetrahedral element can cause crosswind diffusion.
The standard mesh generator in Simscale provides a better diversity in cell types, including tetrahedral cells which are in general less skewed than hexagonal cells. This can lead to a mesh that facilities better stability when compared to the hexagonal dominant mesh generators. On the other hand, the standard mesh generator cannot generate a 2D mesh, which leads to the question what dimensions the flow domain for the CFD simulation should have. Further decision making in selecting the correct mesh generator is discussed in the next chapter.

4.2. The Governing Equations & Finite Volume Method

The governing equations that describe the flow field are the continuity equation (17), momentum equations (18) and the energy equation (19).

$$\nabla \cdot \mathbf{u} = 0 \tag{17}$$

$$\nabla \cdot (\mathbf{uu}) = -\frac{1}{\rho}\nabla p + \nabla \cdot (\nu \nabla \mathbf{u}) + \mathbf{g} \tag{18}$$

$$\nabla \cdot (\rho \mathbf{u} c) = -\nabla \cdot \mathbf{q} + S_c \tag{19}$$

where $\mathbf{g}$ is the gravity. Because Simscale uses OPENFOAM®, it is assumed that the second order finite volume method is used. For the derivation of the finite volume discretization method is assumed that flow variables vary linearly across each cell. Furthermore, OPENFOAM® uses a collocated grid, in which each flow variable is stored in the cell centroid. Simscale makes use of the finite volume method to discretize the momentum equations. Firstly, all terms in equation (18) are integrated over the cell volume

$$\int_V \nabla \cdot (\mathbf{uu})\, \mathrm{dV} = \int_V -\frac{1}{\rho} \nabla p \mathrm{dV} + \int_V \nabla \cdot (\nu \nabla \mathbf{u}) dV + \int_V \mathbf{g} \mathrm{dV} \tag{20}$$

Constant source terms such as gravity and linear source terms are easier to integrate than non-linear source terms. Non-linear source terms are resolved by linearizing. To increase the stability of the solver, Simscale uses an implicit-explicit treatment for the source terms. In this treatment. source terms that give a positive contribution to the diagonal of the magnification matrix are allocated to the right hand side in the magnification matrix, while source terms that give a negative contribution are allocated to left hand side of the equation.
Convection terms $\nabla \cdot (\mathbf{uu})$ and diffusion terms $\nabla \cdot (\nu \nabla \mathbf{u})$ require a different treatment and are integrated using the divergence theorem. E.g. if the convection term is integrated using divergence theorem, one obtains

$$\int_V \nabla \cdot (\mathbf{uu})\, \mathrm{dV} = \int_A \mathbf{u} (\mathbf{u} \cdot \hat{n}) \mathrm{dA} \tag{21}$$

Where $(\mathbf{u} \cdot \hat{n})\mathrm{dA}$ is the volume flow rate out of the cell surface. The surface integral in equation (21) can be rewritten as the summation over a finite number of surfaces

$$\int_A \mathbf{u} (\mathbf{u} \cdot \hat{n}) \mathrm{dA} = \sum_{i=1}^{N} \int_A \mathbf{u_i} (\mathbf{u_i} \cdot \hat{n_i}) \mathrm{dA_i} \tag{22}$$

Because the variation across the faces is linear, the surface integral of each face can be approximated as the value at the face center f (Jasak, 1996)[54], i.e.

$$\sum_{i=1}^{N} \int_A \mathbf{u_i} (\mathbf{u_i} \cdot \hat{n}) \mathrm{dA_i} \approx \sum_{i=1}^{N} \mathbf{u_{fi}} (\mathbf{u_{fi}} \cdot \hat{n}_{fi}) A_i \tag{23}$$

where the face center velocity can be obtained by using an interpolation scheme. Equation (23) can now be used for resolving the flow. However, because flow variables are stored at the cell centroid, differencing schemes are needed to interpolate to the face values of the cell. Before moving on to differencing schemes, the importance of mesh non-orthogonality is discussed in the next section.

4.3. Available Methods For Resolving The Boundary Layers

Because flow variables such as velocity have non-linear variation close to the wall, it is important to emphasize that the variation from the owner cell to the neighboring cell is linear, as mentioned in section 4.1. Therefore, resolving boundary layers with only a basic mesh size is not sufficient. To resolve boundary layers, two types of methods are offered by Simscale, which are the use of wall functions and inflation layers.
Figure 41 shows the non-linear behavior of the velocity nearby the wall. Note that there are three different regions close to the wall in which the velocity change is different. The dimensionless velocity can be described by the following set of equations (Liu, 2016) [55]

$$U^+ = \begin{cases} y^+ & y^+ < 5 \\ \frac{1}{\kappa}\log(Ey^+) & 30 < y^+ < 200 \end{cases} \quad (24)$$

where κ and E are equal to 0.4187 and 9.793 respectively. Note that there is no description for the region $5 < y^+ < 30$. Hence an approximation has to be performed. One method is to apply non-linear empirical equations known as wall functions to the cells adjacent to the wall in order to predict the flow. Because the y^+ value switches during the convergence of the simulation, the CFD code will switch between wall functions once the y^+ value changes its value from e.g. the logarithmic region to the buffer layer. This switching behavior might cause inaccuracies during the convergence. Therefore, it is recommended that the centroid of the cell adjacent to the wall has an y^+ value that is at least equal to 30 to prevent the switching of wall functions. The advantages of using wall functions are a lower cell count and better cell quality/ aspect ratios than when resolving the flow with inflation layers. However, a disadvantage of using wall functions is that they become inaccurate when there is separation, curvature and/or adverse pressure gradients in the flow. For this study, the use of inflation layers is preferred. How the dimensioning of inflation layers is determined, will be discussed in the next chapter.

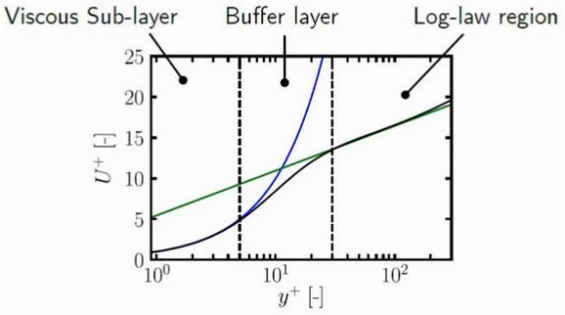

Fig. 41. Typical Dimensionless mean velocity profile U^+ as a function of the dimensionless wall distance y^+.

4.4. Solvers

In this section, the numerics of the solvers that are used by the so-called analysis types are discussed. Taking into account the physics of the air curtain, only the analysis types applicable to the air curtain are further discussed.

The steady-state incompressible analysis is based on the simpleFoam solver, while the steady state convective heat transfer analysis type is based on the buoyantBoussinesqSimpleFoam/ buoyantSimpleFoam solver, which solve the compressible Navier Stokes equations. Moreover, buoyantBoussinesqSimpleFoam uses the Boussinesq approximation to model natural convection, which is discussed in this section. In addition, solvers that use the system of equations of the different flow variables are discussed. Therefore, this section will further focus on explaining the numerics of these solvers.

4.4.1. The Gauss-Seidel and the geometric agglomerated algebraic multigrid (GAMG) methods

In order to solve a linear system of equations $\mathbf{Ax} = \mathbf{b}$ with a square matrix **A** that is positive definite or diagonally dominant (i.e. $\mathbf{x^T Ax} > \mathbf{0}$ and $|a_{ii}| \geq \sum_{i \neq j} |a_{ij}|$ where a_{ij} is an element of the matrix **A)**, the Gauss-Seidel method can be applied. In this method, all the off-diagonal components of the matrix **A** are brought to the right hand side. Consequently, these terms are guessed for the initial iteration. Next, the components of the vector **x** are calculated sequentially, where the calculated components of the previous rows are used for the computation of the component in the next row, which is different than Jacobi since in this method the components are calculated in parallel. The Gauss-seidel method is most commonly used in Simscale and is standardly applied for the computation of the velocity, temperature, turbulent kinetic energy and specific dissipation rate when using the incompressible and convective heat transfer analysis types. However, for the computation of the pressure the GAMG method is used, which is used to reduce the convergence time of the simulation. The GAMG method is set as a standard solver for the pressure in the aforementioned analysis types in Simscale.

4.4.2. The Semi-Implicit Method for Pressure Linked Equations (SIMPLE) algorithm

The simpleFoam solver is used for steady-state, incompressible, turbulent flow using the SIMPLE algorithm to solve the momentum equations and realizes a coupling between the velocity and pressure field. Firstly, equation (18) can be rewritten as

$$\nabla \cdot (\mathbf{uu}) - \nabla \cdot (\nu \nabla \mathbf{u}) = -\frac{1}{\rho}\nabla p + \mathbf{g} \tag{25}$$

Which can be written as a matrix equation, with a known diagonal matrix **A**, a known off-diagonal matrix **H** and an unknown matrix for the velocities

$$\mathbf{AU} - \mathbf{H} = \frac{1}{\rho}\nabla p + \mathbf{g} \tag{26}$$

Equation (26) can be rearranged to get

$$\mathbf{U} = \mathbf{A^{-1}H} - \frac{1}{\rho}\mathbf{A^{-1}}\,\nabla p + \mathbf{A^{-1}g} \tag{27}$$

which can be substituted in the continuity equation and rearranged to obtain

$$\nabla \cdot \left(\frac{1}{\rho}\mathbf{A^{-1}}\nabla p\right) = \nabla \cdot (\mathbf{A^{-1}H} + \mathbf{A^{-1}g}) \tag{28}$$

to compute the pressure. Initially the velocity is computed by equation (25) by providing an initial guess for the pressure. Hereafter, the corrected pressure is computed by equation (28). Consequently, the velocity is recalculated. This cycle is repeated until both continuity and conservation of momentum are satisfied.

4.4.3. Modelling Natural Convection

In this section, the Boussinesq approximation and the weakly compressible flow are discussed for modelling natural convection.

4.4.3.1. The Boussinesq approximation

To account for buoyancy forces in the simulation, a variable density should be considered in the governing equations. However, computing the density for each term would be computationally expensive and lead to highly non-linearized equations, which can cause instability issues. One way to solve this problem is by assuming that density variation is mainly important in the buoyancy term and can be neglected for the other terms. The density can be expressed as

$$\rho = \rho_0 + \Delta\rho \tag{29}$$

where ρ_0 is the reference density and $\Delta\rho$ is the density difference. Using equation (29) and assuming that density changes only affect the gravity term, one can rewrite equations (18) as

$$\nabla \cdot (\mathbf{uu}) = -\nabla p + \nabla \cdot (\mu \nabla \mathbf{u}) + \frac{\rho \mathbf{g}}{\rho_0} \tag{30}$$

Note that an increase in temperature (at constant pressure) leads decrease in density. This relationship can be expressed with the thermal expansion coefficient

$$\beta = -\frac{1}{\rho_0}\left(\frac{\partial \rho}{\partial T}\right)_p \tag{31}$$

by discretizing equation (31) and using a reference temperature T_0 one can write

$$\frac{\rho \mathbf{g}}{\rho_0} \approx [1 - \beta(T - T_0)]\mathbf{g} \tag{32}$$

which can be substituted in equation (30). Note that the boussinesq approximation gives errors less than 1% if the temperature change for air is less than 15℃ (Ferziger & Peric, 2002)[56]. Therefore, one can expect higher errors for greater temperature fluctuations.

4.4.3.2. Weakly Compressible flow

Alternatively, one can solve for a weakly compressible flow by assuming that air can be modelled as an incompressible ideal gas. In this approach density is inversely proportional to temperature and not a function of pressure. Hence the equation of state becomes

$$\rho = \frac{P_{ref}}{RT} \tag{33}$$

Where in the case of the cabinet the reference pressure is equal to the atmospheric pressure.

4.5. Turbulence modelling

Another important step in the simulation setup is the selection of the correct turbulence model. Therefore, in this section the available turbulence models in Simscale are reviewed. As mentioned before, the purchased commercial Simscale package only contains Reynolds-Average-Navier-Stokes (RANS) turbulence models [**26**]. Therefore, the LES turbulence model is not reviewed in this section.

The RANS equations are derived by applying a Reynolds decomposition to the Navier-Stokes equations, in which the steady state solution is decoupled from time varying fluctuations in the system. Using the Einstein summation convention, the resulting RANS equations are

$$\frac{\partial \bar{u}_i}{\partial x_i} = 0 \tag{34}$$

$$\frac{\partial(\bar{u}_i \bar{u}_j)}{\partial x_j} = -\frac{1}{\rho}\frac{\partial \bar{p}}{\partial x_i} + \frac{\partial}{\partial x_j}\left[\nu\left(\frac{\partial \bar{u}_i}{\partial x_j} + \frac{\partial \bar{u}_j}{\partial x_i}\right) - \overline{u_i' u_j'}\right] + F_{b,i} \tag{35}$$

where the bar refers to the fact that the quantities in the equations are averaged, u' are the fluctuating velocities and $F_{b,i}$ is the external body force (including gravity). The Reynolds stress tensor is a symmetric tensor that has 6 unknowns. Moreover, the unknown pressure and velocities lead to a closure problem with 4 equations and 10 unknowns. To solve this problem, one can make use of so-called eddy viscosity models in which it is assumed that the Reynolds stresses are determined by the mean flow gradients $\frac{\partial u_i}{\partial x_j}$

$$\overline{u_i' u_j'} \approx \frac{2}{3} k \delta_{ij} - \nu_t \left(\frac{\partial \bar{u}_i}{\partial x_j} + \frac{\partial \bar{u}_j}{\partial x_i} \right) \tag{36}$$

Hence, the number of unknowns is reduced to 5, where only the turbulent eddy viscosity ν_t has to be calculated. This is where turbulence models come into play. Simscale offers three turbulence models, the $k-\varepsilon$ model, the $k-\omega$ model and the $k-\omega$ SST model. These models will be further discussed in the following sections.

4.5.1. The $k-\varepsilon$ model

The steady state $k-\varepsilon$ model is defined by the transport equation for the turbulent kinetic energy k

$$u_j \cdot \frac{\partial k}{\partial x_j} = P_k + P_b - \varepsilon + \frac{\partial}{\partial x_j} \left[\left(\nu + \frac{\nu_t}{\sigma_k} \right) \frac{\partial k}{\partial x_j} \right] \tag{37}$$

where P_k turbulent kinetic energy production due to mean velocity shear and P_b is the turbulent kinetic energy production due to buoyancy. Furthermore, the steady state transport equation of the turbulent dissipation is defined by

$$u_j \cdot \frac{\partial \varepsilon}{\partial x_j} = C_{\varepsilon_1} \frac{\varepsilon}{k} \left(P_k - C_{\varepsilon_2} \varepsilon + C_{\varepsilon_3} P_b \right) + \frac{\partial}{\partial x_j} \left[\left(\nu + \frac{\nu_t}{\sigma_\varepsilon} \right) \frac{\partial \varepsilon}{\partial x_j} \right] \tag{38}$$

Once the transport equations have been solved for k and ε, the turbulent eddy viscosity can be computed by

$$\mu_t = C_\mu \frac{\rho k^2}{\varepsilon} \tag{39}$$

For the standard $k-\varepsilon$ model by Launder & Spalding (1983)[57] the model coefficients are $\sigma_k = 1, \sigma_\varepsilon = 1.3, C_{\varepsilon_1} = 1.44, C_{\varepsilon_2} = 1.92$ and $C_\mu = 0.09$. Furthermore, note that for a round jet $C_{\varepsilon_1} = 1.6$, but this is not the case for a plane jet. In addition, it has to be remarked that the use of the $k-\varepsilon$ has its limitations. As one knows, the viscosity in the viscous sub-layer near the wall reduces the mixing length of the turbulent eddies. In addition, the above transport equations alone don't take into account the mixing length reduction near the wall. Therefore, the standard $k-\varepsilon$ model makes use of so-called damping functions. The damping functions in the standard $k-\varepsilon$ model are equal to (Launder & Sharma, 1974)[58]

$$f_2 = 1 - 0.3 \exp\left(-Re_T^2\right) \tag{40}$$

$$f_\mu = \exp\left(-\frac{3.4}{1 + \left(\frac{Re_T}{50} \right)^2} \right) \tag{41}$$

where the turbulent Reynolds number equals

$$Re_T = \frac{\rho k^2}{\mu \varepsilon} \tag{42}$$

Consequently, the new turbulent viscosity is computed by taking the product of equation (39) and equation (41) i.e.

$$\mu_t = f_\mu C_\mu \frac{\rho k^2}{\varepsilon} \tag{43}$$

Note that when the new turbulent viscosity is computed it is not only applied to the adjacent cells to the walls. Instead, all the cells in the mesh make use of the damped turbulent viscosity. Moreover, note that f_μ is a function of the turbulent Reynolds number, where $f_\mu \to 1$ as $Re_T \to \infty$, meaning that the turbulent eddy viscosity remains undamped for cells far away from the walls (also called the high Reynolds number formulation). The damping function f_2 is multiplied with the term $C_{\varepsilon_2}\varepsilon$ in equation (38) such that turbulent dissipation increases near the wall. Consequently, the dissipation of turbulent kinetic energy is increased. A downside of the use of damping functions in the $k-\varepsilon$ is the fact that the prediction becomes inaccurate when flow separation is involved. On the contrary, the $k-\omega$ model can accurately predict boundary layers with flow separation.

4.5.2. The $k-\omega$ model

The $k-\omega$ model is defined by the same transport equation for the turbulent kinetic energy ((38)). The specific turbulent dissipation can be written as (Wilcox, 1998) [59]

$$u_j \cdot \frac{\partial \omega}{\partial x_j} = \frac{\gamma}{\nu_T} P_k - \beta \rho \omega^2 + \frac{\partial}{\partial x_j}\left[\left(\mu + \frac{\mu_T}{\sigma_k}\right)\frac{\partial \omega}{\partial x_j}\right] \tag{44}$$

where β and γ are model coefficients and

$$\omega = \frac{\varepsilon}{C_\mu k} \tag{45}$$

In addition, the $k-\omega$ model doesn't need any damping functions. While the $k-\omega$ is a good fit for wall bounded flows with flow separation, it cannot be accurately resolve free shear flows. However, free shear flows are accurately be resolved by the $k-\varepsilon$ model. Therefore, the $k-\omega$ SST is invented, which uses the $k-\omega$ for the near wall flow and the $k-\varepsilon$ model for the free shear flow. In between the near wall flow and the shear flow a blend of both turbulence models is used, by using blending functions.

5. Validation Of The Simulation

As concluded in section 3.4, a benchmark test for the physics of the air curtain should be performed, such that the performance of the commercial Simscale package can be analyzed. Therefore, this chapter will discuss in detail the air curtain benchmark test which is simulated in Simscale.
The first step in the simulation setup is the determination of the flow domain. As discussed in section 3.3, it would be a good decision to validate the simulation in combination with measurements tools that are more accurate than available in the current Fri-Jado inventory. Therefore, the decision was made to resort to literature that performed experimental measurements on similar cabinets, using more accurate measurement tools than the TESTO 425 that was used in the experimental testing. Luckily, relevant literature is provided by [32] and Field and Loth (2004) [60] in which PIV was performed on a wall bounded air curtain that was generated by a cabinet. The experimental testing in these articles was under a controlled environment and the geometry of the cabinet is relatively simple in these tests, which make these experiments suitable for validation of the air curtain simulation in the commercial Simscale package.
After the benchmark tests are completed, a more advanced flow domain that is more relatable to the Fri-Jado geometry will be validated by comparing the experimentally measured temperature profiles with the simulated temperature profiles.

5.1. Benchmark Test - Simulation Geometry

To create the wall jet configuration that was used in [32] and [60] , a wall was mounted to the front of the shelves to represent a cabinet that was fully stocked with food products, as shown in figure 42. The geometry was recreated using Ansys SpaceClaim and is shown in figure 43. Note that in this figure, the used boundary conditions are indicated by the colored edges. The boundary conditions will be further discussed in section 5.3. Also note that the outlet which had an initial length of 120mm was modified to include all the area up to the solid wall to pull the air curtain straight, resulting in enlarging the outlet to 240mm. To model the entrainment of ambient air into the air curtain, a part of the environment is included in the flow domain. In addition, to reduce the recirculation caused by the open boundary, a geometry with an inclined boundary was prepared for the test, shown in figure 44. The effect of an inclined open boundary is compared for the entrainment velocity in section 5.5.4.

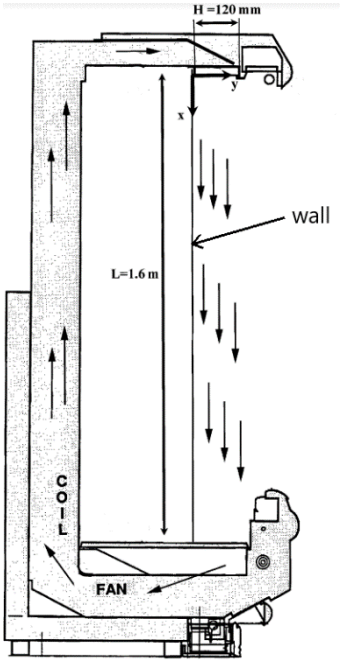

Fig. 42. Wall jet configuration used in the experiments of Field and Loth. Adapted from [32]

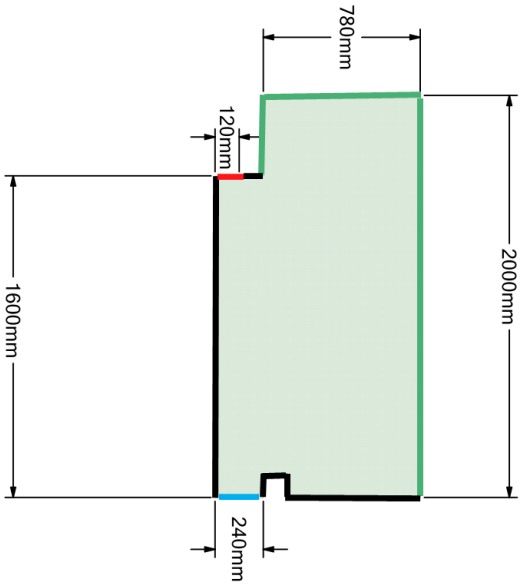

Fig. 43. Representation of the wall jet configuration in Spaceclaim. The black lines represent walls, the red line the air supply, the blue line the air return and the green lines open boundaries

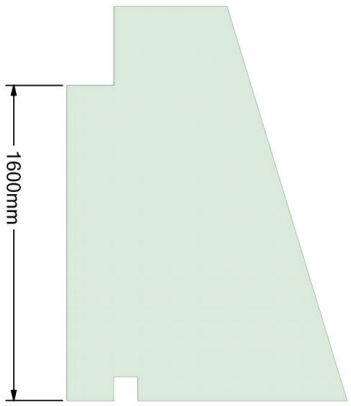

Fig. 44. The wall jet geometry with an inclined open boundary to reduce recirculation. Note that the applied boundary conditions are equal to the boundary conditions described in figure 43.

5.2. Benchmark Test - Generating The Mesh

As mentioned in section 4.2, the Simscale mesh generators can only be properly used for the generation of 3D grids, since the parametric hexagonal mesh generator is the only one that can generate a 2D grid (by setting the number of cells in the third direction equal to one). The downside of the parametric hexagonal mesh generator is the fact that only (split) hexagonal cells are generated, which can reduce the stability as the non-orthogonality is increased by these elements. In addition, Simscale recommends using other CFD softwares for generating 2D meshes. Therefore, the used mesh generator is the standard Ansys mesh generator. To convert the output filetype (.msh) to the accepted Simscale input filetype, the OPENFOAM® command fluentMeshToFoam was used.

Before initiating the meshing process, the analysis type in Ansys was set to 2D and physics preference was set to CFD. The fineness of the internal cells was firstly determined by looking at the boundary layer flow along the wall to which the air curtain is bounded, to guarantee a smooth transition. While section 2.4 mentioned that the air curtain is initially laminar, for the sake of modelling with RANS it is assumed that the entire air curtain is a fully developed turbulent flow.

To determine the height of the first cell layer adjacent to the wall, one has to consider the y^+ value, which is the dimensionless distance normal to the wall. To account for possible flow separation, the $k-\omega$ SST turbulence model is used in combination with inflation layers to model the near wall behavior. Therefore, the aim is to generate a first layer cell height, that is present in the viscous sublayer of the wall bounded air curtain i.e. $y^+ < 5$. To increase the odds of obtaining a first layer height below $y^+ = 5$, the y^+ value for the initial guess was set equal to unity. The initial guess for the cell height of the adjacent cells to the wall is computed with Schlichtings equation for the skin friction in a turbulent boundary layer for a flat plate, which is equal to (Schlichting, 2003)[62]

$$C_f = [2\log_{10}(Re_L) - 0.65]^{-2.3} \quad \text{for} \quad Re_L < 10^9 \tag{46}$$

where the Reynolds number is equal to

$$Re_L = \frac{uL}{\nu} \tag{47}$$

Note that equation (46) is used because it is applicable for a fully developed turbulent boundary layer. The reference length scale L was set equal to 1.6m, which is equal to the length of the wall to which the air curtain is bounded. Consequently, the wall shear stress equals

$$\tau_w = \left(\frac{1}{2}\rho u^2\right) C_f \tag{48}$$

The friction velocity is then computed with

$$u_\tau = \sqrt{\frac{\tau_w}{\rho}} \tag{49}$$

which leads to the distance of the centroid of the cell adjacent to the wall

$$y_p = \frac{y^+ \mu}{\rho v_\tau} \tag{50}$$

The calculated values for equations (46)-(50) are shown in table 8.

Table 8. Calculated values for making an initial guess of the first cell layer adjacent to the wall to which the air curtain is bounded.

Benchmark	Property	C_f	Re_L	τ_w	v_τ	y_P	y_H
	Unit	-	-	Pa	$m\,s^{-1}$	m	m
Isothermal	Calculated	0.0065	61333	0.00129	0.033	$4.5\cdot 10^{-4}$	$9.0 \cdot 10^{-4}$
Non-isothermal	value	0.0058	105263	0.00347	0.053	$2.8 \cdot 10^{-4}$	$5.6 \cdot 10^{-4}$

Finally, when applying boundary layers in the Ansys mesh generator, the first layer height y_H has to be specified, meaning that one has to multiply equation (50) by a factor of 2. Once the simulation is finished, one can use a postprocessor to assess the y^+ along the wall. Consequently, a convergence study for different first layer cell heights can be applied to assess the accuracy of the model. To realize this, the total cell layer height can be calculated by

$$y_T = y_H \frac{1 - G^N}{1 - G} \tag{51}$$

where G is the growth factor and N the number of inflation layers. The growth factor G is the factor by which each inflation layer grows in the direction normal from the wall. The standard recommended value of 1.2 was used for the growth factor. Moreover, one can approximate the turbulent momentum boundary layer thickness for a fully developed isothermal plane jet by [43]

$$\delta_{99} = 0.014x \tag{52}$$

According to equation (52), the maximum boundary layer thickness for the air curtain is equal to 0.0224m. Because it is assumed that a thinner boundary layer for the non-isothermal air curtain occurs due to buoyant acceleration, equation (52) is used for the approximation of the boundary layer of the non-isothermal air curtain as well.
By equating (51) to (52) and solving for N one obtains a number of 10 inflation layers at $y^+ = 1$ for the isothermal air curtain and 12 inflation layers at $y^+ = 1$ for the non-isothermal air curtain. The inflation layers consist of rectangular cells, while the remaining internal cells consist of a quadrilateral dominant mesh for both benchmark tests. Quadrilateral cells were preferred over triangular cells because for the same refinement length scale quadrilateral cells cover more area, reducing computational resources. In addition, the internal cell size was set to $1 \cdot 10^{-2}$m for the isothermal case and $4 \cdot 10^{-3}$ because no further improvements were observed at the post-processing for smaller mesh sizes. As mentioned in appendix E, one can use a non-orthogonal correction to improve the stability. In order to determine whether a non-orthogonal correction is needed, the skewness and non-orthogonality were checked in the Ansys mesh generator. In Ansys, the orthogonal quality is obtained by computing

$$\theta_{cell} = \max[\cos^{-1}\left(\frac{\mathbf{d} \cdot \hat{n}}{|\mathbf{d}||\hat{n}|}\right), \cos^{-1}\left(\frac{\mathbf{c} \cdot \hat{n}}{|\mathbf{c}||\hat{n}|}\right)] \tag{53}$$

where both angles were explained in appendix E. In Ansys, an acceptable cell skewness is smaller than 0.94, where a skewness of 0 is excellent. In addition, an acceptable orthogonal quality is greater than 0.15, where the ideal orthogonal quality equals 1. Therefore, the skewness and orthogonal quality were both assessed in the Ansys mesh generator.
Pictures of the mesh used for the isothermal case are shown in figures 45 and 46. From these figures, one can see the orthogonality of the mesh.

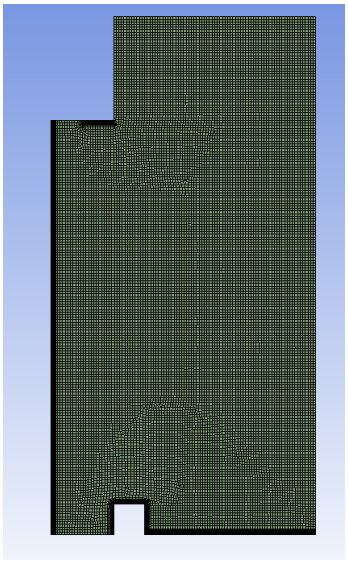

Fig. 45. Unstructured mesh of the benchmark isothermal air curtain

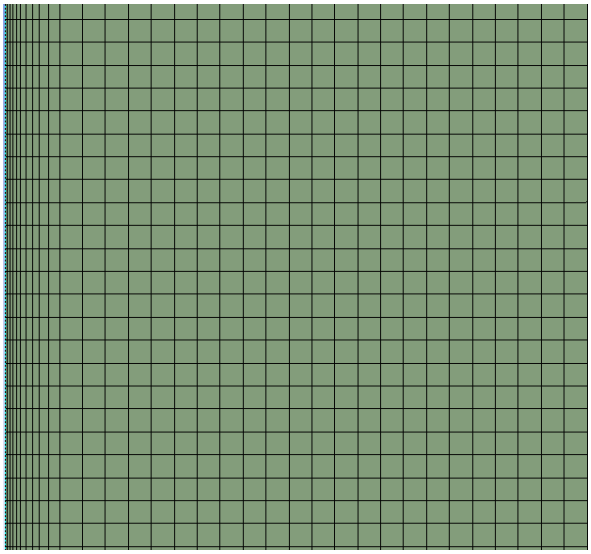

Fig. 46. Boundary layers in the isothermal air curtain benchmark mesh

For the isothermal air curtain mesh, 20969 cells out of 21930 cells had a orthogonal quality approximately equal to 0.96, while most remaining cells had a distribution over an orthogonal quality of 0.72-0.9. The reference length scale used for the isothermal mesh was equal to 0.01m. For the non-isothermal air curtain mesh, out of 125546 elements 123537 elements had an orthogonal quality equal to 0,97, while most remaining cells had a distribution over an orthogonal quality of 0.69-0.92. The reference length scale used for the isothermal mesh was equal to 0.004m and was reduced with respect to the isothermal air curtain because it showed improvement in the results. Note that some triangles were present in the mesh, while most elements were squares, which is due to the quadrilateral dominant mesh method that was selected in Ansys. Finally, the option for making the right open boundary inclined was considered, however no significant changes were observed with respect to the mesh depicted in figure 45 after analyzing the post-processed results.

5.3. Benchmark Test - Boundary Conditions

Figure 43 shows the edges of the geometry to which each boundary condition is applied. The streamwise velocity and RMS velocity profiles nearby the inlet at $\frac{x}{H} = 1$ were measured by using PIV. The measured velocity profile for the isothermal air curtain is shown in figure 47.

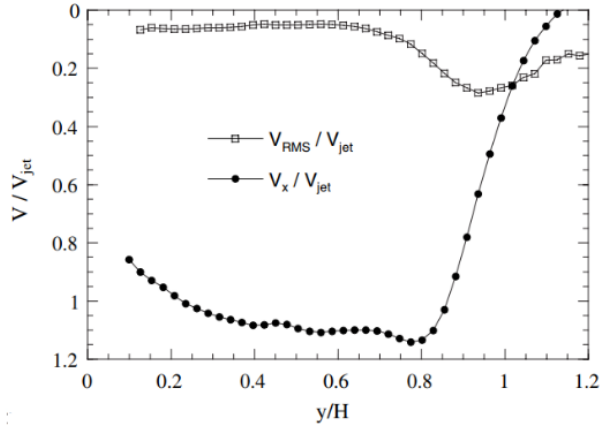

Fig. 47. Initial streamwise velocity and RMS velocity profiles of the air curtain for $\frac{x}{H} = 1$ and $Re = 4600$. Note that V_{jet} corresponds to the Reynolds number. Also note that in the experiments described in literature, the streamwise coordinate is equal to x and the air curtain thickness coordinate is y. Furthermore, note that the slot width in the figure is equal to H. Adapted from [60].

To validate the isothermal and non-isothermal models of the air curtain, the given velocity profiles will be used as an velocity inlet boundary condition. A pressure outlet is used for the return air boundary. For the isothermal model, an entrainment boundary condition is formulated for the open boundary by combining a total pressure condition for the pressure and a pressure inlet-outlet velocity condition for the velocity. The total pressure condition is defined by

$$p = \begin{cases} p_0 & \text{for outlfow} \\ p_0 - \frac{1}{2}\rho|\mathbf{u}|^2 & \text{for inflow} \end{cases} \tag{54}$$

where p_0 is the stagnation pressure. Hence, for the inflow the velocity is equal to

$$u = \sqrt{\frac{2(p_0 - p)}{\rho}} \tag{55}$$

where the pressure is constant for the outflow, which is similar to a pressure outlet.
The entrainment boundary condition for the non-isothermal air curtain uses an inlet/outlet boundary condition that was added for the temperature, which gives a zero gradient boundary condition when the velocity vector of the neighboring cell points outside the domain and a fixed value of 24 °C when the velocity vector of the neighboring cell points inside the domain. The zero gradient boundary condition copies the flow variables stored inside the internal cell that is adjacent to the boundary cell, with the result that the normal gradient between the boundary and the neighboring cells is equal to zero. The zero gradient condition was also applied to the turbulent kinetic energy and specific dissipation rate at the open boundaries. The turbulent kinetic energy and specific turbulence dissipation rate for the initialization of the flow domain were calculated by

$$k = \frac{3}{2}(I|u|)^2 \tag{56}$$

and

$$\omega = \frac{k^{0.5}}{C_\mu^{0.25} L} \tag{57}$$

where a turbulence intensity and velocity equal to the inlet conditions were used. Finally, all the walls were modelled with a no slip boundary condition and an adiabatic boundary condition for the non-isothermal air curtain. To initialize the simulation, the temperature was set to 11 °C, which is approximately in between 24°C and -2 °C. The turbulent kinetic energy and specific dissipation rate were initialized for all internal cell centroids using equations (46) and (47), using the average inlet velocity.

5.4. Benchmark Test - Numerical methods

The standard recommended Simscale solvers that are used are the Gauss-Seidel smooth solver for the velocity, turbulent kinetic energy and specific dissipation rate and the geometric agglomerated algebraic multigrid solver for the pressure field as previously discussed in section 4.4.1. Furthermore, the discretization of the diffusion and convection terms were realized with the Gauss scheme, as discussed in section 4.2. For the Laplacian terms e.g. $\nabla \cdot (\nu \nabla u)$, ν is linearly interpolated while gradient schemes make use of the second order least squares method as discussed in appendix E. The least squares method is used for computing the gradient, since it reduces the skewness error that occurs when the mesh is not completely orthogonal. The face values of the divergence terms are computed by the bounded upwind scheme. To further increase stability, a non-orthogonal correction (as described in appendix E1) with

a limiter coefficient equal to 0.5 was applied. Finally, both the Boussinesq approximation and the weakly compressible flow were applied to the non-isothermal benchmark test and compared.

5.5. Benchmark Test - Assessment Of The Accuracy

Once the mesh was constructed and the simulation was ready, the postprocessor was opened to assess the accuracy of the simulation.

5.5.1. Assessment Of The y^+ Values

To validate the cell height of the first cell layer adjacent to the wall, the goal was to generate y^+ values smaller than 5, as supported in section 5.1. This goal was achieved for both the isothermal and non-isothermal air curtains with the aforementioned mesh as can be depicted from figure 48. The highest value for the isothermal air curtain is closest to the inlet and just exceeds 2.5, while the highest value for the non-isothermal air curtain is also closest to the inlet and just exceeds 3. In addition, for both benchmarks the y^+ values decrease significantly once $\frac{z}{b}$ increases with respect to the inlet and decreases with respect to the outlet. Therefore, for both air curtains the modelling approach of the determination of the first cell layer height, was deemed successful and no additional iterations for smaller inflation layer sizes were needed.

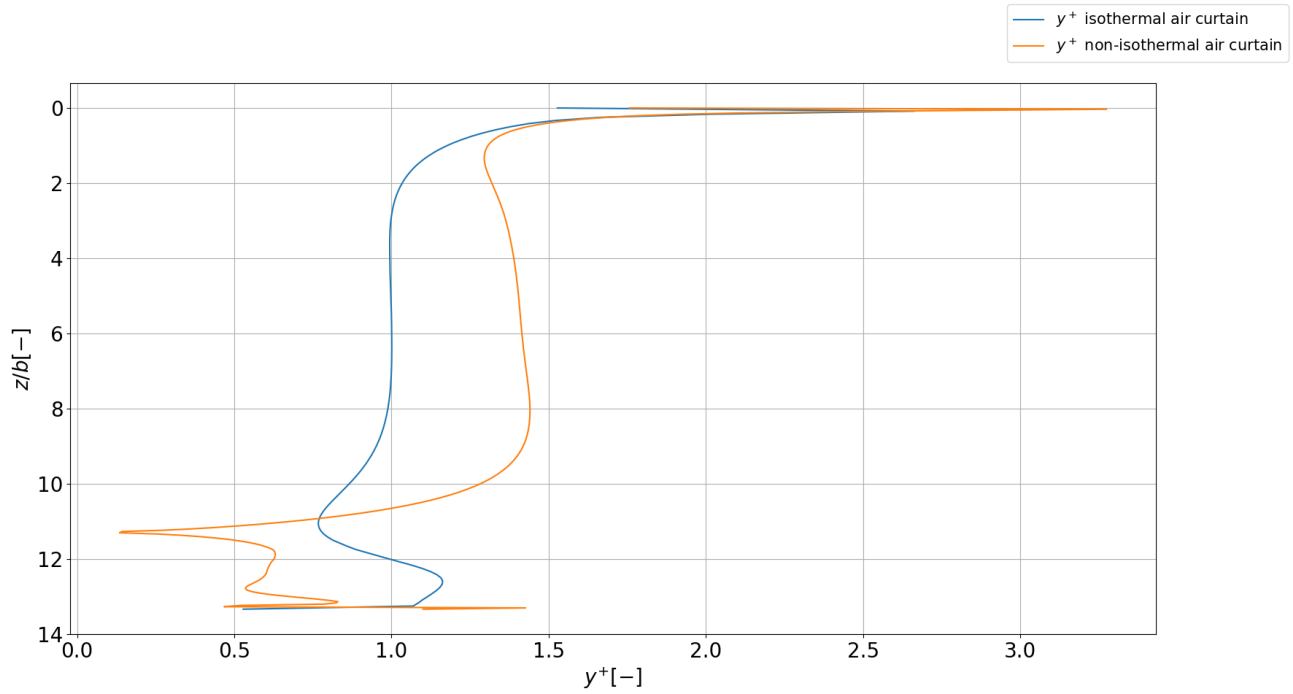

Fig. 48. The postprocessed y^+ values measured along the wall to which the air curtain is bounded in the streamwise $\frac{z}{b}$ direction for the isothermal (blue line) and non-isothermal (orange line) air curtain. Note that $\frac{z}{b} = 0$ is upstream at the supply.

5.5.2. Comparison with the experimentally measured velocity profiles

The accuracy of the simulation was assessed by comparing the simulated downstream air curtain velocity profiles with the experimental ones. The experimentally obtained velocity profiles are shown in figure 49 for the isothermal air curtain and figure 50 for the non-isothermal air curtain.

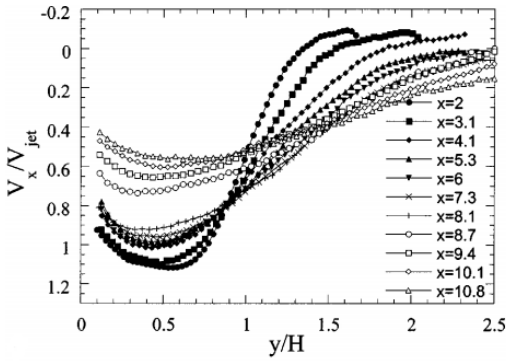

Fig. 49. Evolution of streamwise velocity profiles for Re=4600. Note that x is the streamwise coordinate, H is the slot width and the Reynolds number is based on the average streamwise velocity V_{jet} at $\frac{x}{b} = 1$. Adapted from [60].

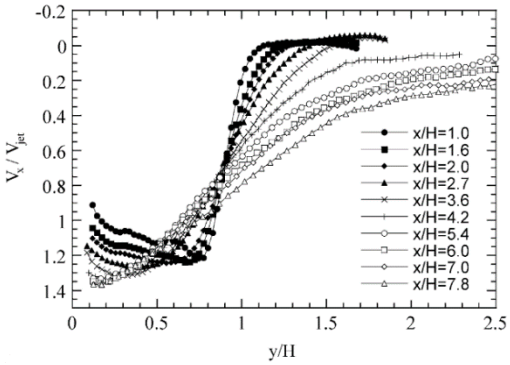

Fig. 50. Evolution of streamwise velocity profiles for Ri = 0.13 and Re = 8000. Note that x is the streamwise coordinate, H is the slot width and the Reynolds number is based on the average streamwise velocity V_{jet} at $\frac{x}{b} = 1$. Adapted from [32].

5.5.2.1. The Isothermal Air Curtain

The contour plot of the velocity in the x direction (from inlet to outlet) for the isothermal air curtain is shown in figure 51. One can see that the red colored velocity of the contour plot starts to decrease around mid-way in the direction of the outlet, which is about 6-7 slot diameters considering the length of the wall to be equal to 1.6m. In addition, one can observe the linear growth of the jet when looking at figure 51.

The contour plot of the turbulent kinetic energy is depicted in figure 52. One can see that the most turbulent kinetic energy is produced at the shear layer, which is at the interface of the jet and the ambient. In addition, the turbulent decreases as it flows downstream due to the decrease of the streamwise velocity. Finally, the turbulent kinetic energy causes the jet to grow in width linearly, which is in accordance with the expected behavior of the jet [43].

Fig. 51. Contour plot of the velocity in the x direction for the isothermal air curtain.

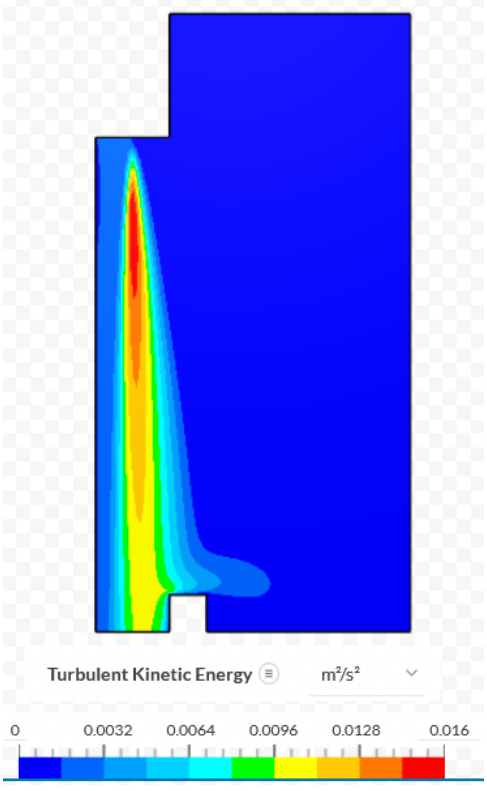

Fig. 52. Contour plot of the turbulent kinetic energy for the isothermal air curtain.

Figure 53 shows the simulated velocity profiles that are compared with the velocity profiles that are shown in figure 49. From the subplots in figure 53, one can see that the velocity profiles initially show a good agreement. However, from $\frac{z}{b} = 8.7$ onward one can see that the velocity profiles decay faster greater than in the simulation.
The first reason that one can expect is that the simulation is performed in a 2D domain instead of 3D domain which is applicable to the real flow. As turbulence is characterized by high levels of fluctuating vorticity, the absence of important vorticity-maintenance mechanisms such as vortex stretching guarantee that turbulence cannot be completely captured by a 2D CFD model that uses the $k - \varepsilon$ model, which assumes isotropic time-averaged turbulence (Tennekes & Lumley, 1972)[61].
A second reason one can expect is the fact that the $k - \omega$ SST turbulence model generates inaccuracies. [50] performed a 3D simulation of an air curtain in a cross-stream according to the geometry depicted in figure 33, using the $k - \varepsilon$ model. In the simulation of [50], the velocity profiles were also overpredicted. As mentioned in section 3.2, the reduced decay of the velocity profiles can also be ascribed to the fact that the production term in the $k - \varepsilon$ model only considers the mean flow gradients, neglecting velocity fluctuations caused by the Kelvin Helmholtz instability. The Kelvin Helmholtz instability generates vortices that transition into turbulence, leading to diffusion of the velocity profiles as observed from experiment.

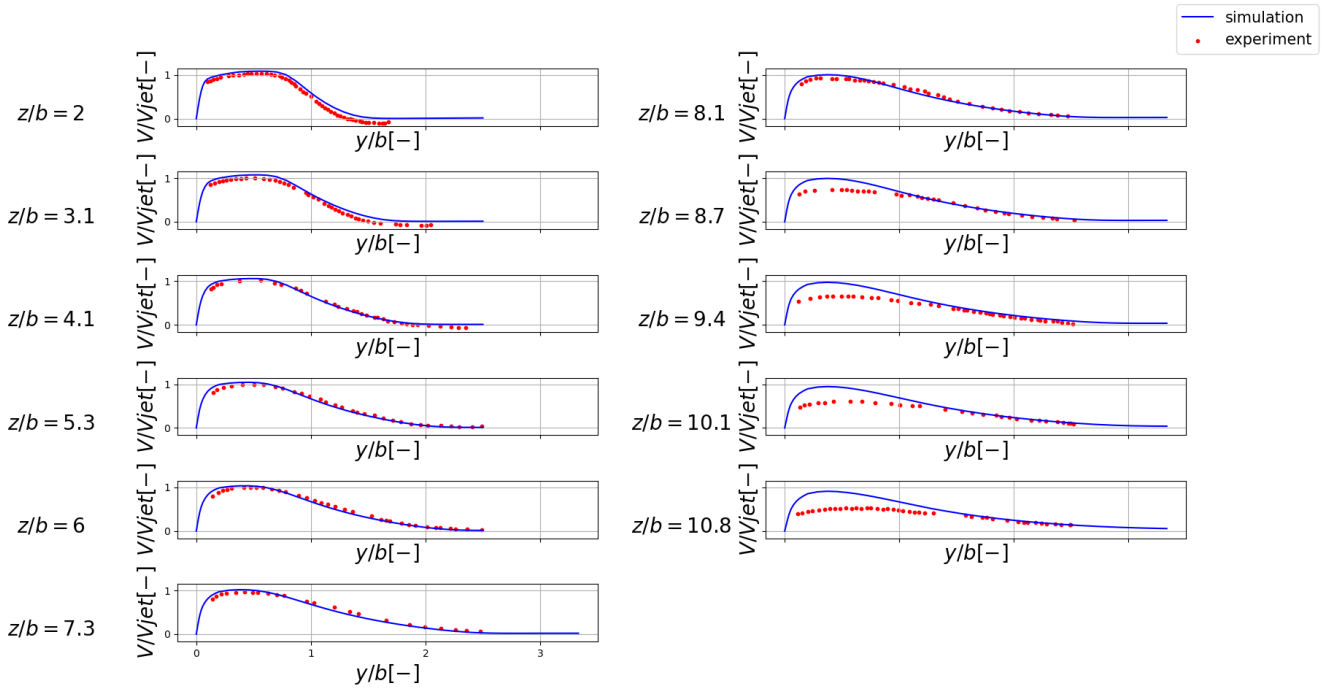

Fig. 53. Comparison of experimental (red dots) and simulated (blue line) velocity profiles for the isothermal air curtain, for $Re = 4600$.

5.5.2.2. The Non-isothermal Air Curtain

Figure 54 shows the contour plot for the velocity in the x-direction for the non-isothermal air curtain. This time, one can see that the velocity profiles initially increase in magnitude, which is due to the buoyant acceleration caused by density differences. The turbulent kinetic energy of the non-isothermal air curtain is shown in figure 55. As for the isothermal air curtain, the most turbulent kinetic energy is at the location where the velocity is highest, causing the maximum value for the turbulent kinetic energy in the air curtain to shift in downstream direction. Finally, observe that near the open boundaries there are fluctuations in velocity and turbulent kinetic energy. This is the effect of the used boundary condition and is unphysical, since in reality the ambient was quiescent. However, because the open boundary is sufficiently far from the air curtain, these unphysical perturbations do not affect the air curtain.

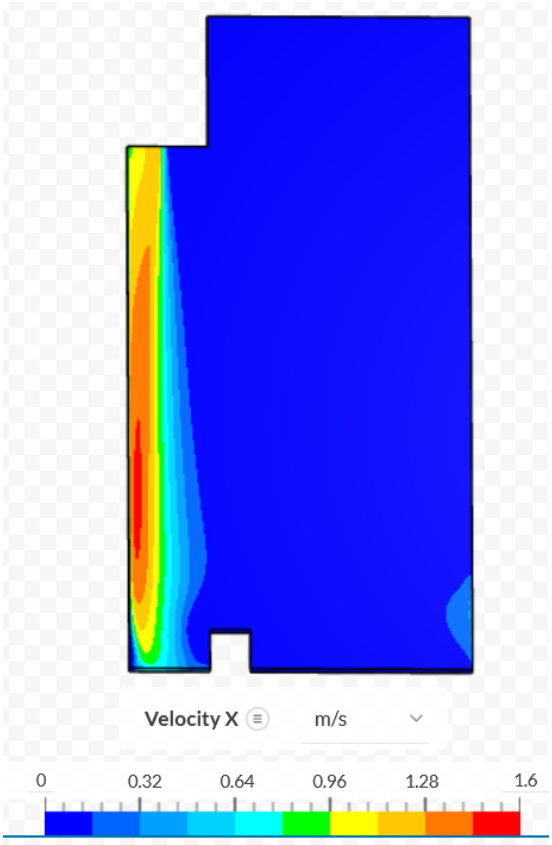

Fig. 54. Contour plot of the velocity in the x direction (from inlet to outlet) for the non-isothermal air curtain (weakly compressible).

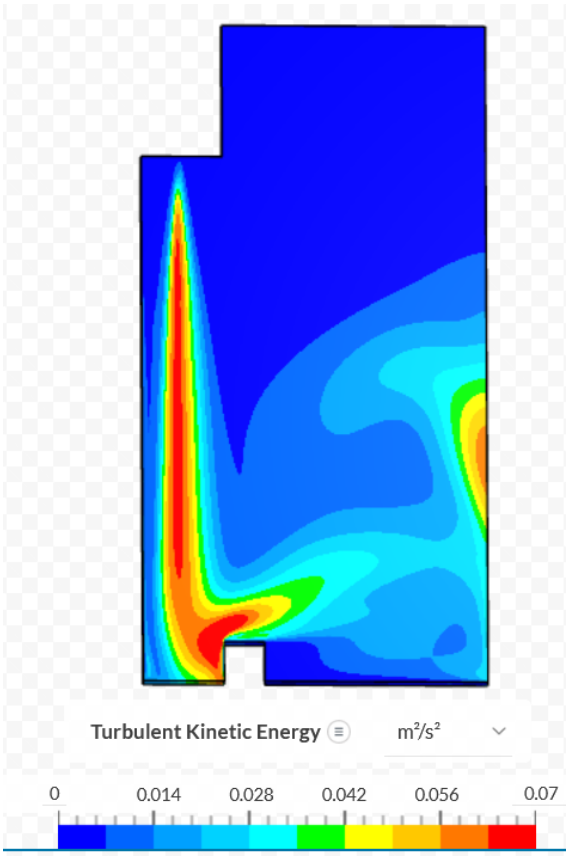

Fig. 55. Contour plot of the turbulent kinetic energy for the non-isothermal air curtain (weakly compressible). Note that the red color was shifted to the left to better illustrate the mixing layer. This was necessary because the highest values for the turbulent kinetic energy were at the right open boundary.

Figure 56 shows the simulated velocity profiles for the non-isothermal air curtain for $Ri = 0.13$ and $Re = 8000$. As mentioned in section 2.4.1, the non-isothermal air curtain accelerates due to the buoyancy force, which is also visible in figure 56 . In addition, peak velocities can be observed nearby the wall because turbulent diffusion has not yet affected this region. One can observe a good agreement until $\frac{z}{b} = 3.6$. Again, the mass flow is smaller in the experiment than in the simulation for large $\frac{z}{b}$ due to the 2D domain and the production term in the $k - \varepsilon$ model. However, the overprediction of the velocity profiles of the non-isothermal air curtain is less than the overprediction for the isothermal air curtain, due to the effect of the buoyant acceleration [33]. Finally, no big difference was observed between the simulation that used the Boussinesq approximation and the simulation that used the weakly compressible flow.

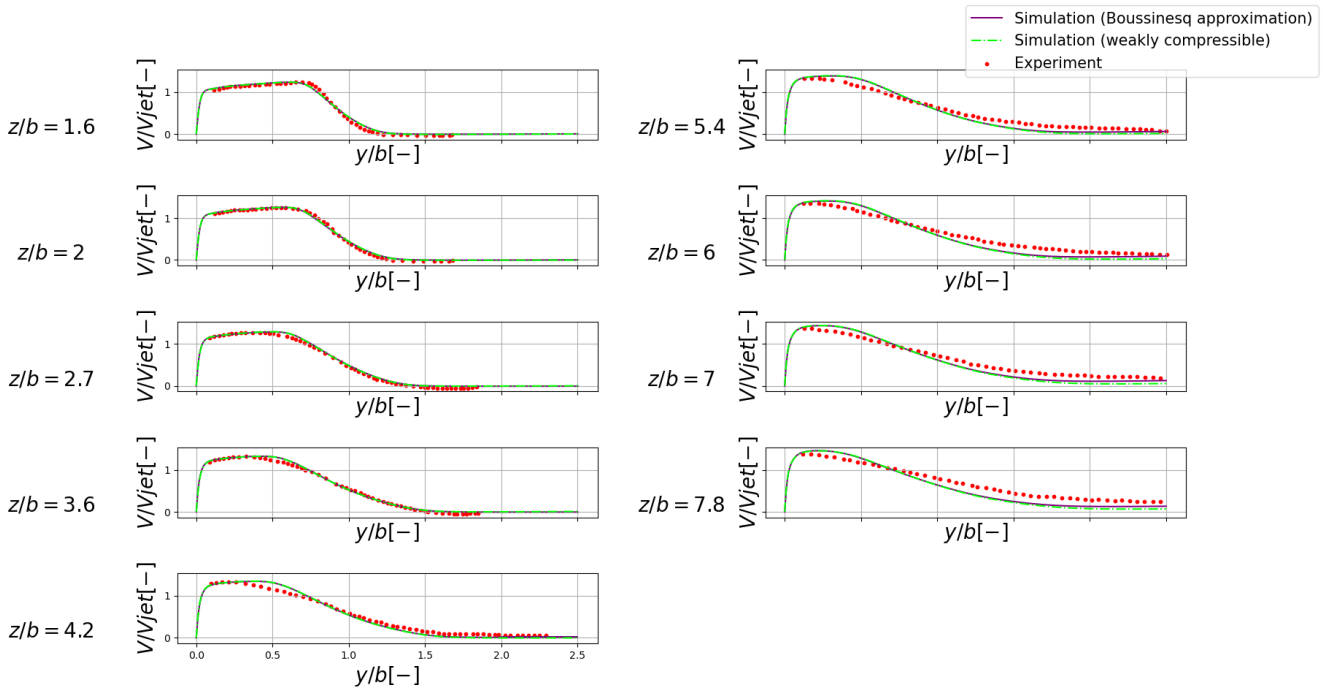

Fig. 56. Comparison of experimental (red dots) and simulated (blue line) velocity profiles for the non-isothermal air curtain for Re = 8000 and Ri = 0.13.

5.5.3. Comparison Of The Air Curtain Thickness

In addition, the evolution of the air curtain thickness was compared. In this case, the air curtain thickness is defined as $\delta(x) = y$ at $\frac{V_x(y)}{V_{x,max}} = 0.25$. The measured air curtain thickness is depicted in figures 57 and 58, for different Reynolds numbers. Note that for the validation case, the author of this report only considered the inlet velocity profiles shown in figures 49 and 50. Also note that for the non-isothermal case, the air curtain thickness decreases for an increasing Richardson number. A higher Richardson number indicates a higher temperature difference and thus a higher buoyant acceleration, which decreases the separation of the air curtain with respect to the wall.

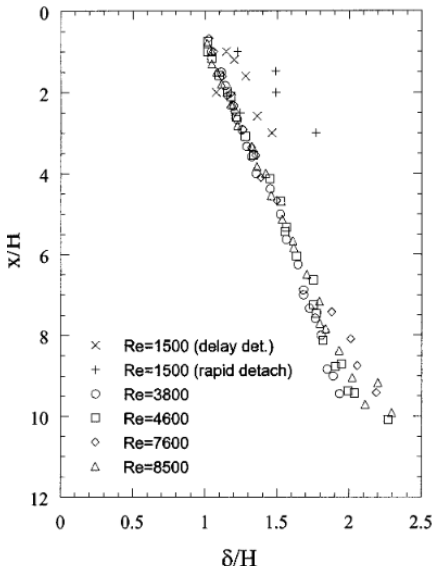

Fig. 57. Air curtain thickness development for the isothermal air curtain. In the experiment [60] measured for different Reynolds numbers. For the benchmark, the author only considers Re = 4600.

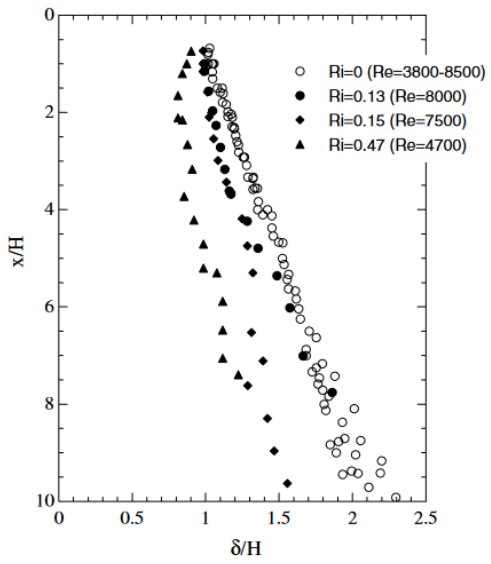

Fig. 58. Air curtain thickness development for the non-isothermal air curtain. In the experiment [32] measured the air curtain thickness for different Reynolds numbers. For the benchmark, only Re = 8000 is considered.

5.5.3.1. The Isothermal Air Curtain

Figure 59 shows the simulated versus experimentally obtained evolution of the isothermal air curtain thickness and supports the findings for the velocity profiles figure 53. One can see that until $\frac{z}{b} = 3.1$ the air curtain thickness of the simulation is greater than that of the experiment. Firstly, the velocity profile at $\frac{z}{b} = 1$ of the experiment was taken as the inlet velocity profile for the simulation. Meaning that there is an offset error in the prediction of the air curtain thickness. In the experiment, Kelvin-Helmholtz instabilities are initially generated and later transfer their kinetic energy into smaller scale eddies, meaning that it takes some pathlength along the $\frac{z}{b}$ direction before additional turbulence is generated and the air curtain velocity profile starts to decay. Therefore, one can see that after $\frac{z}{b} = 3.1$ the simulated air curtain thickness is underpredicted, once additional vorticity is generated in the experiment. Finally, notice that after $\frac{z}{b} = 9.4$, the prediction of the air curtain thickness leads to an error that exceeds 10%, which becomes significantly inaccurate. The air curtain thickness is therefore in reasonable agreement with experiment until $\frac{z}{b} = 9.4$. To assess the accuracy of the air curtain thickness, the relative error for the simulated values with respect to the experimental values was computed by

$$\bar{e}_{\phi_{\text{relative}}} = \frac{\delta_{\text{experiment}} - \delta_{\text{simulation}}}{\delta_{\text{experiment}}} \cdot 100 \tag{58}$$

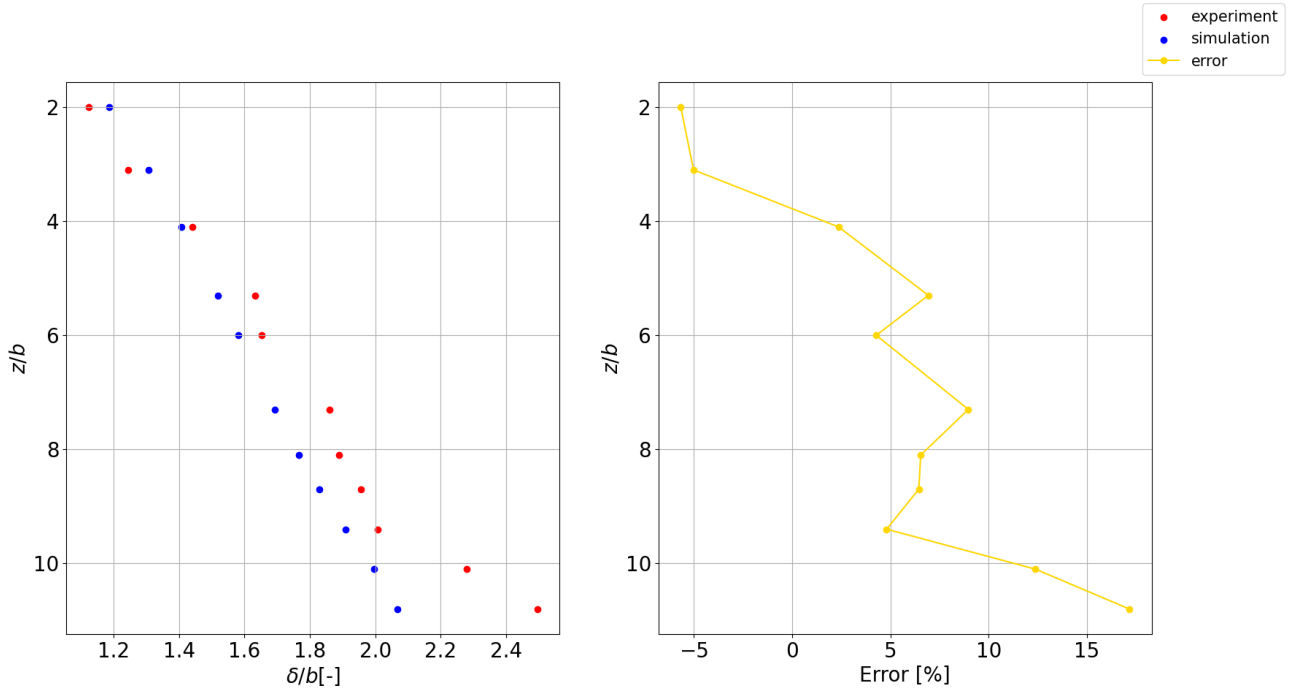

Fig. 59. Comparison of experimental (red dots) and simulated (blue dots) evolution of the air curtain thickness for the isothermal benchmark test. Note that the sign changes of the error changes when $\delta_{\text{experiment}} > \delta_{\text{simulation}}$.

5.5.3.2. The Non-isothermal Air Curtain

Figure 60 shows the non-isothermal air curtain thickness for the simulation that used the Boussinesq approximation, the simulation that used the weakly compressible flow and the experiment. Note that for both simulations the air curtain thickness is initially overpredicted, which is due to the same offset error as for the isothermal case, caused by the use of the velocity profile at $\frac{z}{b} = 1$ as a velocity inlet boundary condition. After $\frac{z}{b} = 3.6$, one can observe that the experimental air curtain thickness increases at a much faster rate than both simulations, showing that the RANS turbulence modelling greatly underpredicts. For both simulations after $\frac{z}{b} = 5.4$ the error passes the 10% mark, which

is significantly more upstream than the air curtain thickness prediction for the isothermal case, which passed the 10% error margin after $\frac{z}{b} = 9.4$. In addition, both the simulations output about the same quantities for the air curtain thickness. Recall that according to [56], the Boussinesq approximation is only valid for temperature differences smaller than 15°C. While the Boussinesq approximation appears to perform slightly better than the weakly compressible flow at first sight, it has to be noted that the error with respect to the experiment increased for the Boussinesq approximation when the number of iterations were increased, meaning that the Boussinesq approximation takes longer to converge than the weakly compressible flow. Therefore, it appears that the convergence error in the simulation with the Boussinesq approximation dampens the modelling error, since the total error with respect to the experiment increases. Because the weakly compressible flow has a lower convergence time than Boussinesq approximation, a lower number of computational resources is required. Therefore, the implementation of the weakly compressible flow is preferred over the Boussinesq approximation.

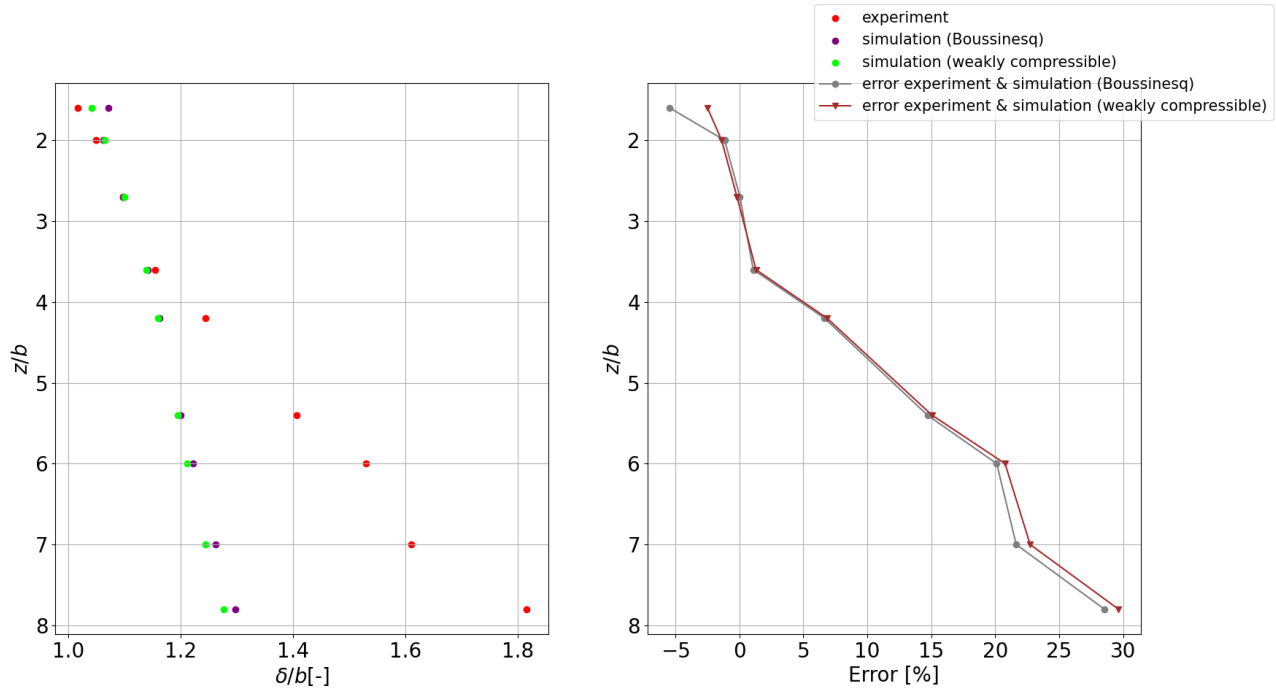

Fig. 60. Comparison of experimental (red dots) and simulated (blue dots) evolution of the air curtain thickness for the non-isothermal benchmark test. Note that the sign changes of the error changes when $\delta_{experiment} > \delta_{simulation}$.

5.5.4. The Entrainment Velocity

Figure 61 shows the entrainment velocity which is plotted for the isothermal and non-isothermal air curtain over the line $(\frac{y}{b} = 2, \frac{z}{b} = 0)$ until $(\frac{y}{b} = 2, \frac{z}{b} = 12.33)$ i.e. the opening of the cabinet. From this plot the negative entrainment velocities show for both the isothermal and non-isothermal air curtain that air is entrained until $\frac{z}{b} \approx 10$, where the velocity becomes zero. After $\frac{z}{b} \approx 10$ the entrainment velocity is positive, meaning that the air curtain spills air. Note that the entrainment velocity for the non-isothermal air curtain has a higher magnitude than the isothermal air curtain, due to the buoyant acceleration and because of the higher Reynolds number. In addition, note that for the isothermal air curtain the amount of spilled air is less than the amount of entrained air, which is unphysical because mass is not conserved.

For the non-isothermal air curtain simulations, one can observe that after $\frac{z}{b} \approx 10$ the entrainment velocity significantly increases, which happens because a certain amount of air is unable to flow through the pressure outlet. Consequently, the air mass leaves the open right open boundary. Note that this observation is also true for the isothermal air curtain, although less significantly. In addition, the Boussinesq approximation and the weakly compressible flow show approximately the same entrainment velocities, again indicating the similarity in results between both simulations. Furthermore, the non-isothermal air curtain that applies the weakly compressible flow in combination with the inclined open boundary (orange) shows a reduced entrainment velocity with respect to the weakly compressible simulation

with the straight boundary (lime), especially between $\frac{z}{b} = 4$ and $\frac{z}{b} = 10$. The reduced entrainment velocity indicates that the effects of recirculation due to the open boundaries is somewhat mitigated. However, one can observe that the entrainment velocity is not very significantly affected.
Finally, figures 62, 63, 64 and 65 show the streamlines of the isothermal and non-isothermal simulations. From these figures one can see recirculation occurring in the region at the right side of the air curtain. When comparing the recirculation for the weakly compressible flow simulations (figures 63 and 65), one can see that the recirculation for the simulation with the inclined boundary is slightly less, since a smaller amount of air is directed upwards. Hence, this comparison again validates that the use of an inclined boundary has a beneficial impact on the recirculation effects caused by the open boundary, although not a very significant one.

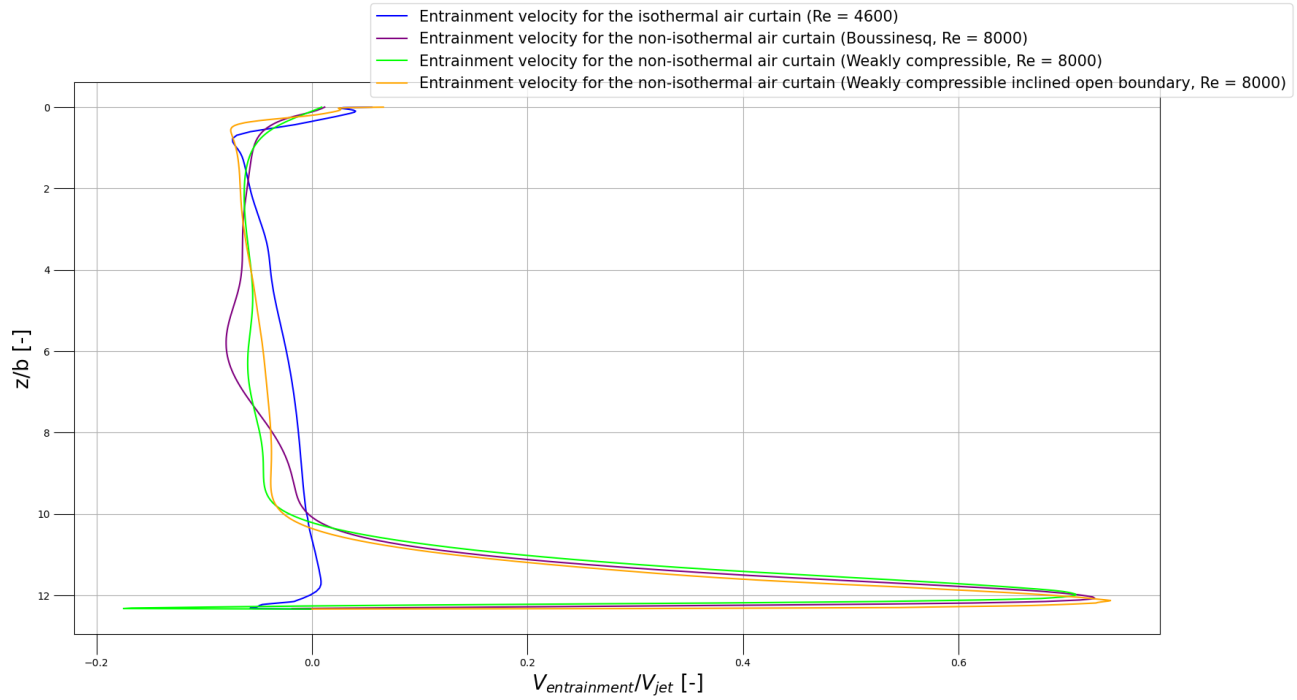

Fig. 61. Entrainment velocity of the isothermal and non-isothermal air curtain.

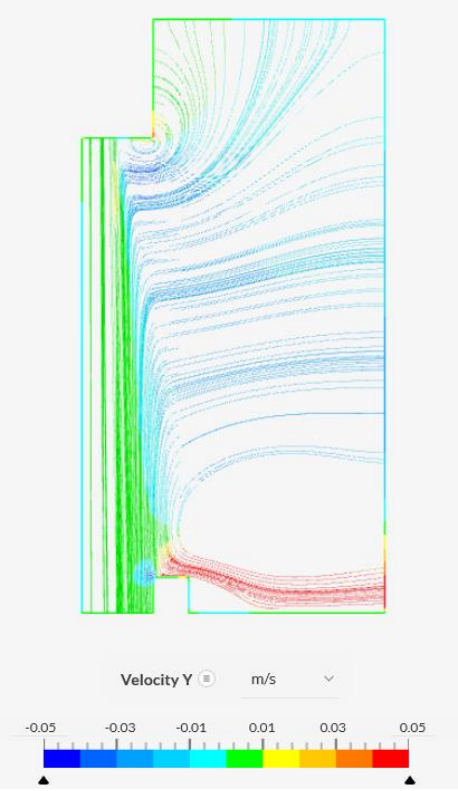

Fig. 62. Streamlines for the isothermal air curtain. The colors in the contour plot represent the velocity in the y direction. Note that a green color represents a positive y velocity and a blue color represent a negative y velocity.

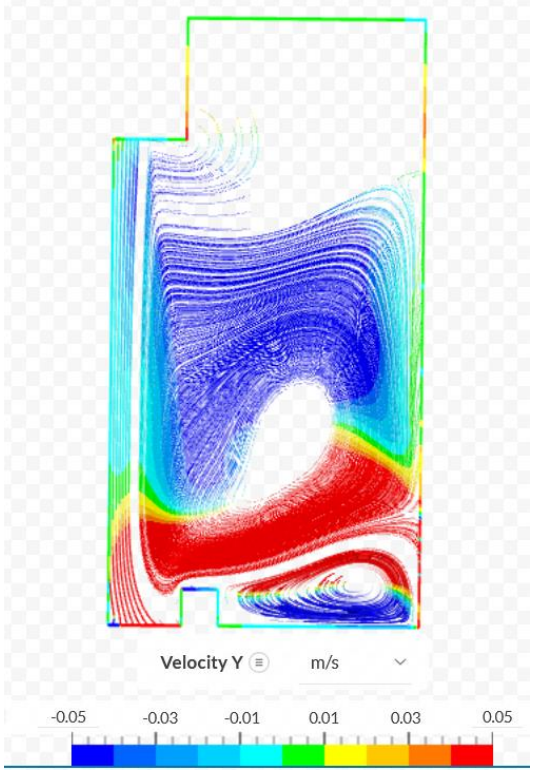

Fig. 63. Streamlines for the non-isothermal air curtain (Weakly compressible flow). The colors in the contour plot represent the velocity in the y direction. Note that a green color represents a positive y velocity and a blue color represent a negative y velocity.

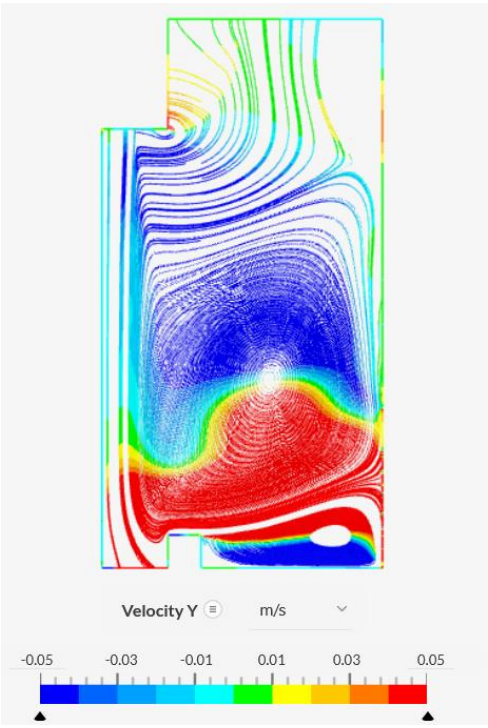

Fig. 64. Streamlines for the non-isothermal air curtain (Boussinesq approximation). The colors in the contour plot represent the velocity in the y direction. Note that a green color represents a positive y velocity and a blue color represent a negative y velocity.

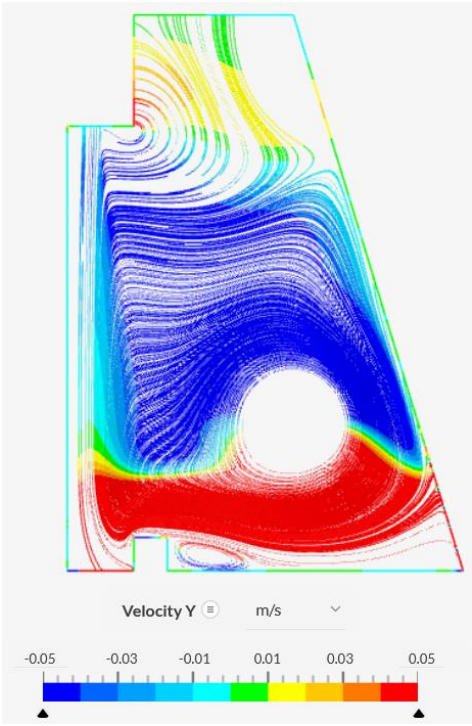

Fig. 65. Streamlines for the non-isothermal air curtain with the inclined open boundary (Weakly compressible flow). The colors in the contour plot represent the velocity in the y direction. Note that a green color represents a positive y velocity and a blue color represent a negative y velocity.

5.5.5. Mass Conservation Check

The inlet, outlet and entrainment velocity profiles were extracted by the postprocessor and integrated over each boundary to check for mass conservation. Velocities were numerically integrated by using Riemann summation. The values for each benchmark are shown in table 9. Note that for the entrainment boundary the net flowrate was calculated since mass flows in and out of this boundary. For simplicity, a constant density for the non-isothermal air curtain was assumed. Note that due to the integration, there exists some error. Moreover, there probably is some discretization error, which lead to mass not being conserved in the domain. However, from the integration one can conclude that this difference is negligible, since mass is approximately conserved.

Finally, one can see in table 9 that the net flow rate over the frontal opening of the isothermal air curtain is higher than for the non-isothermal case, indicating that mass at the frontal opening is better conserved for the non-isothermal case than for the isothermal case. One reason, for this could be the coarser mesh that was used for the isothermal simulation.

Table 9. Flowrates at different boundaries for the isothermal and non-isothermal air curtain. A negative sign indicates air flowing out the domain and a positive sign indicates air flowing in the domain

Boundary	Flow rate isothermal ($\frac{m^2}{s}$)	Flow rate non-isothermal (Boussinesq) ($\frac{m^2}{s}$)	Flow rate non-isothermal (weakly compressible) ($\frac{m^2}{s}$)
Inlet	0.066	0.12	0.12
Outlet	-0.089	-0.11	-0.11
Frontal opening	0.021	0.01	0.01

5.5.6. Assessment of the temperature

Figures 66 and 67 show the contour plot of the temperature field for the Boussinesq approximation and the weakly compressible flow. Note that the air curtain spills a lot of cold air, which is due to the combination of the pressure outlet and entrainment boundary conditions. Unfortunately, no experimental data was available to compare with the temperature field.

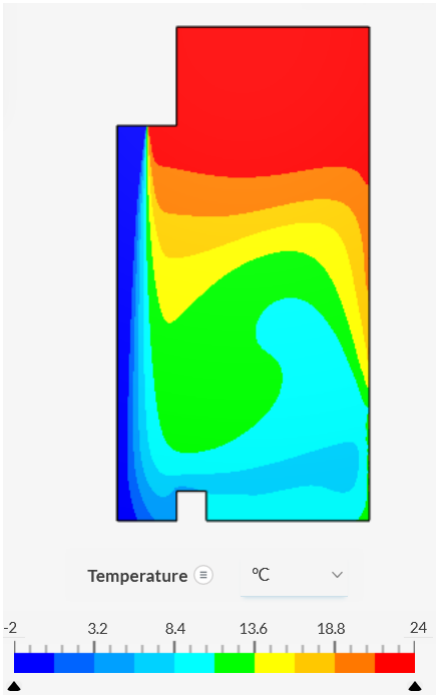

Fig. 66. Contour plot of the temperature field in **°C** (Boussinesq approximation).

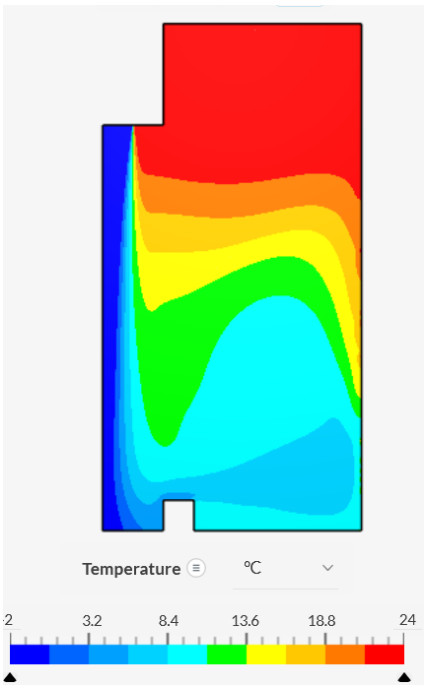

Fig. 67. Contour plot of the temperature in °C (weakly compressible).

5.6. Fri-Jado Geometry – Simulation Geometry

As previously discussed, an isothermal and non-isothermal benchmark test were performed and partly validated. Moreover, no comparison for the simulated air curtain temperatures with the measured experimental values was possible since this data was not available in literature. In addition, no analysis of the discretization error has yet been performed.

Therefore, this section will perform a comparison with the experimentally obtained temperature profiles and a mesh convergence study to assess the discretization error, for the more complex Fri-Jado geometry.

Figure 68 depicts the Fri-Jado geometry, which is a basically a demarcation of the 2D cross-section of the cabinet as shown in figure 2. The domain was created by performing a Boolean subtract between the 3D model and the plane. In addition, figures 69, 70 and 71 show a detailed view for the different mesh sizes that were used for the mesh convergence study. Note that the gap between the top M-package and the shelf is modelled as a wall for simplicity. Finally, note that the same methodology as described in section 5.2 was used for determining the boundary layer mesh. The average orthogonal quality for the coarse, medium and fine meshes were equal to 0.96, 0.97 and 0.98.

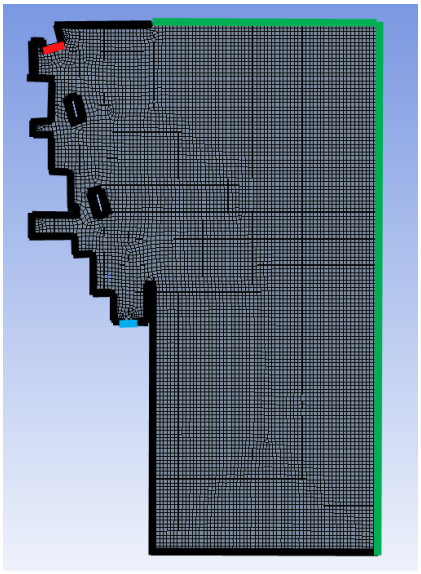

Fig. 68 The entire flow mesh of the Fri-Jado OVRDC. The black lines represent walls, the red line the air supply, the blue line the air return and the green lines open boundaries.

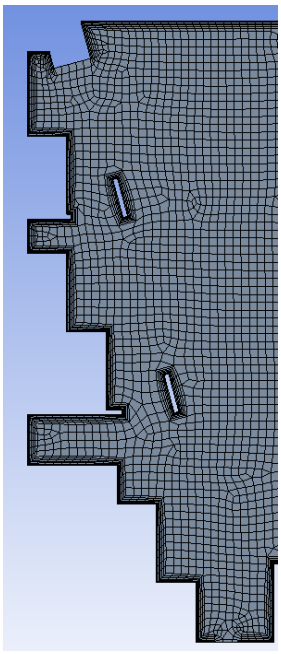

Fig. 69. Detailed view of the coarse mesh.

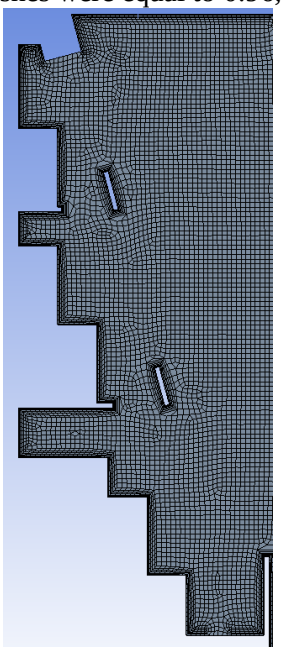

Fig. 70. Detailed view of the medium mesh.

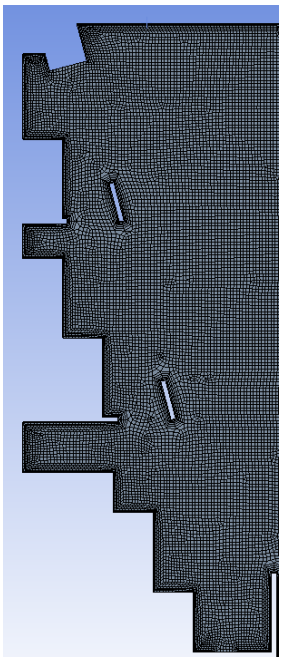

Fig. 71. Detailed view of the fine mesh.

5.7. Fri-Jado Geometry – Boundary Conditions & Numerical methods

For the Fri-Jado geometry a velocity outlet instead of a pressure outlet was used to mitigate the effect of bending of the air curtain near the outlet which was observed for the benchmark tests, as discussed and shown in section 5.5.4. Moreover, fan curve data was present for both the bottom and top fans that were used in the Fri-Jado cabinet during the experiment. To determine the magnitude of the velocity, the simplified assumption was made that the fans operated at their optimum, resulting in a total flowrate of 240 $m^3\ hour^{-1}$ for the bottom fans and a total flowrate of 150 $m^3\ hour^{-1}$ for the top fans (Ebm Papst, 2022)[64]. Next, the flowrate was converted by dividing the total flowrate by the flowthrough area of the inlet/outlet, resulting in a velocity magnitude equal to 1.6 $m\ s^{-1}$ for the return and 1.1 $m\ s^{-1}$ for the supply. These velocities were assigned to the velocity outlet at the return and V_{jet}.

One can convert each velocity in a velocity profile by

$$v_2 = \frac{Re_2}{Re_1} \cdot \frac{b_1}{b_2} \cdot v_1 \tag{59}$$

The dimensionless inlet velocity profile from figure 47 was converted using equation (59) and assigned to the velocity inlet of the Fri-Jado geometry, using the aforementioned value for V_{jet}. The same boundary conditions were used for the walls and the open boundaries that were used for the benchmark test, as described in section 5.3. The assigned boundary conditions for each edge of the geometry are shown in figure 68. Finally, the same numerical methods as described in 5.4 were used. Note that in reality an additional 90 $m^3/hour$ of air is discharged from the conservation space to the air curtain. Since the inlet and outlet velocities were different, the outlet size of the return was modified to reduce the outlet mass flowrate to the inlet mass flowrate.

5.8. Fri-Jado Geometry – Mesh Convergence Study

In a mesh convergence study, one compares a flow variable for at least three different mesh refinements, which are necessary for the assessment as will be explained in this section.
For the mesh convergence study, the average reference length scale of the cells was used for comparison instead of the number of cells since for an infinitely fine mesh the number of cells approaches infinity, while the representative length scale approaches zero. The representative cell length for a 2D mesh is calculated by

$$h = \frac{1}{N}\sum_{Cells} A_p^{0.5} \tag{60}$$

where N is the number of cells and A_p the average area of the cell. The mesh convergence study was applied for the temperature profiles that were probed at the same locations as the thermocouples that were placed in the thermocouple measurements frame (figure 22).
According to Celik et al. (2008) [63], the representative cell length should be at least 30% between each mesh, which can be written as

$$r_{32} = \frac{h_3}{h_2} > 1.3 \text{ and } r_{21} = \frac{h_2}{h_1} > 1.3 \tag{61}$$

where subscripts 1,2 and 3 refer to the fine, medium and coarse meshes. The representative length scale, number of cells and average orthogonal quality of the generated meshes are shown in table 10 .

Table 10. Mesh data

Mesh	Number of cells [-]	Representative cell length [m]	Average orthogonal quality [-]
Coarse	12464	$8.9\cdot 10^{-3}$	0.95
Medium	31330	$5.7\cdot 10^{-3}$	0.97
Fine	68106	$3.9\cdot 10^{-3}$	0.98

Figure 72 shows the y^+ plotted for the first two vertical walls at the shelf 1 (i.e. $\frac{z}{b} = 4.4$ where $b = 42.4\cdot 10^{-3}$m for the Fri-Jado cabinet as mentioned in section 2.1), for the different representative cell lengths. No big difference is observed for the different meshes because an equal first layer height was used for the different mesh sizes. Hence an acceptable transition from the inflation layers to the internal cell nodes was assumed for each mesh. Moreover, note that the peaks in the y^+ occur at the intersection of the horizontal horizontal and vertical walls at shelf 1, which means that the shelves have significant impact on the mesh quality. Although these y^+ are significant, it was observed that they don't surpass $y^+ = 5$ for the entire cabinet length.

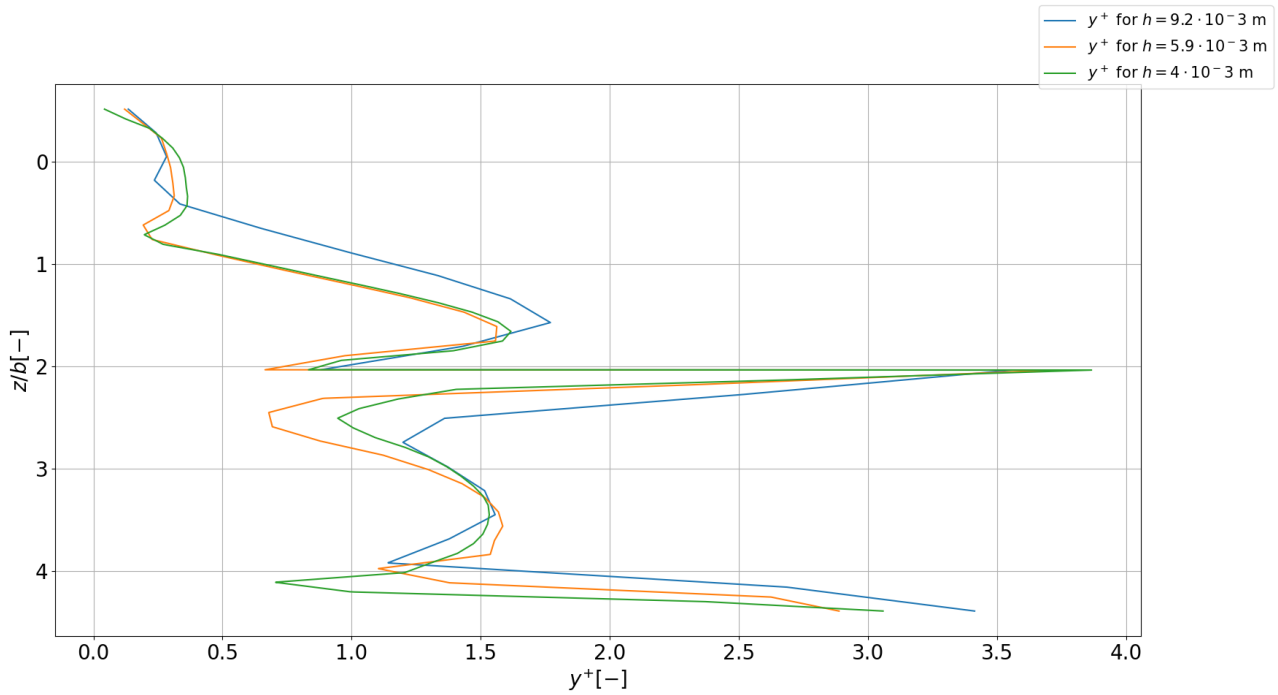

Fig. 72. The postprocessed $\mathbf{y^+}$ values measured along the wall to which the air curtain is bounded in the streamwise $\frac{\mathbf{z}}{\mathbf{b}}$ direction for different representative length scales.

One can approximate the solution of a flow variable using Richardson extrapolation

$$\phi = \phi_0 + ch^p \tag{62}$$

where ϕ_0 is the extrapolated value that estimates the solution for an infinitely fine mesh, c is a constant and P is the order of convergence. Note that $P = 2$ for an ideal CFD calculation when only second order numerical schemes would be applied. However, due to events such as numerical diffusion, numerical dispersion or bounded variables one has to carefully select his/her numerical scheme for discretization. Consequently, one could decide to pick discretization schemes that have an order of convergence below 2. E.g. for the discretization of convection one could pick upwind differencing, in which the variation across the cell is constant. When the mesh is refined using upwind differencing, the error with respect to the real value doesn't reduce proportional to h^2. Therefore, in most real CFD simulations, the order of convergence is below 2. To calculate the order of convergence, one can use

$$p = \frac{1}{\ln(r_{21})} |\ln\left|\frac{\epsilon_{32}}{\epsilon_{21}}\right| + q| \tag{63}$$

where ϵ is the difference between the solution variable of the different meshes and q is equal to

$$q = \ln\left(\frac{r_{21}^p - s}{r_{32}^p - s}\right) \tag{64}$$

and s is equals

$$s = \text{sign}\left(\frac{\epsilon_{32}}{\epsilon_{21}}\right) \tag{65}$$

To solve equation (63) numerically the bisection method was used. To obtain the values c and ϕ_0 one needs three meshes such that a system of two equations can be obtained for equation (62). Rewriting these equations results in

$$c = \frac{\phi_1 - \phi_0}{h_1^P} \tag{66}$$

and

$$\phi_0 = \frac{\left(r_{21}^P \phi_1 - \phi_2\right)}{r_{21}^P - 1} \tag{67}$$

Finally, one can obtain the relative (extrapolated) discretization error by

$$e_{10} = \frac{|\phi_1 - \phi_0|}{\phi_1} \tag{68}$$

5.9. Fri-Jado Geometry – Assessing The Discretization

As mentioned in section 5.5.6, no proper assessment of the accuracy of the temperature profile prediction for the non-isothermal benchmark test could be made because no temperatures were measured in [32]. However, as described in section 2.5.1 experimental measurements for the Fri-Jado cabinet were performed, which can be used to assess the total error. In addition, by applying the mesh convergence study which is described in the previous section to these temperature profiles an indication of the discretization error can be made.

Figure 73 shows the comparison of the air curtain temperature profiles of the 2D simulations and experiment. In addition, the temperature profiles generated by the 3D Simscale simulation (as described in section 3.2) were added to figure 73 for comparison. The temperature profiles measured in the middle of the cabinet (at $\frac{x}{L} = 0.5$) were used in the comparison, since the effects caused by the generated vortices generated at the side walls were smallest in the middle of the cabinet and the 2D simulations cannot include sidewall effects.

Firstly, one can see that the temperature profiles at the supply and return are more accurately corresponding to the experimental values than the 3D simulation. This improved accuracy is caused most likely by the combination of the demarcation of the flow domain (as discussed in section 3.3) and the used boundary conditions.

In addition, one can observe for shelf 1 and shelf 2 that the temperatures of the air curtain nearest to the conservation space are underpredicted for the 3D simulation, while being quantitatively correct for the 2D simulation. One cause for the underprediction in the 3D simulation can be the constant cooling load of 650W that was assigned to the evaporator. For the 3D conjugate heat transfer simulation, it was experienced that the value for the cooling load needed to be tuned, in order to simulate M-package temperatures that were in some agreement with the experimentally measured values of the M-packages of the cabinet (figures 30 and 31**)** . However, for shelf 1 and shelf 2 and increasing $\frac{y}{b}$ one can see for all the simulations that the temperature gradient is greater than the temperature gradient obtained from experimental measurements, which indicates a thicker air curtain for the experiment. The same effects as for the simulations of the benchmark test cause an underprediction of the air curtain thickness, as was previously described for in sections 5.5.2 and 5.5.3.

The red dots in figure 73 display the extrapolated values that were calculated from the previously described method in section 5.8. One can see that for each mesh size there is no big difference between the mesh sizes in the predicted temperature. Therefore, the mesh convergence study was only applied to 5 locations as shown in figure 73, where a relatively high difference for the temperature between each mesh and experiment was observed. The computed data for the extrapolated values P1 to P5 is shown in table 11. One can observe that the coarse mesh is for most temperatures closer to the experimental values than the medium and finer meshes. This indicates that the discretization error reduces the total error. Therefore, it was decided that to use the coarse mesh for optimization purposes, especially because a coarser mesh has lower computational costs.

Finally, note that the used geometry has some big simplifications. In reality, there are gaps between the M-packages and the shelves as can be observed from figure 73. In reality air is recirculated through these gaps and impose an opposing force to the inward bending of the air curtain. In the simulation these gaps were closed and modelled as walls, because it was assumed that the opposing force was negligible. In addition, the sidewalls of the cabinet are not included in the 2D simulation. As mentioned in section 2.4, air that enters and exits the cabinet near the sidewalls generate vortices that cause additional entrainment of ambient air. These vortices are generated due to the high angle

of attack of the crossflow with respect to the sidewalls, which lead to separation. For the 2D simulation such effects are not included.

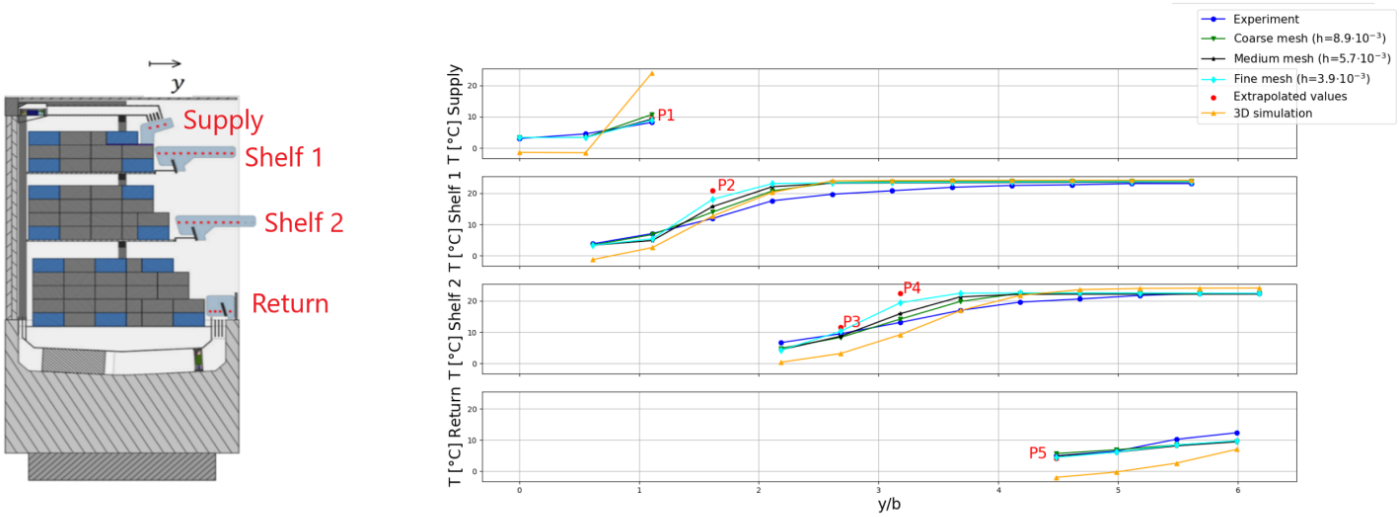

Fig. 73. Comparison of the air curtain temperature profiles of the 2D simulations, 3D simulation and experiment.

Table 11. Results Of The Mesh Convergence Study

Location	Relative extrapolated error [%]	Order of convergence [-]	Convergence Mode	Extrapolated value [°C]
P1	3.0	2	Monotonic	8.7
P2	13.4	1.57	Monotonic	20.8
P3	11.7	2	Monotonic	11.7
P4	13.3	2	Monotonic	22.4
P5	9.7	2	Monotonic	4

Figures 74 and 75 show contour plots of the temperature field and y velocity field. In these figures one can clearly see that there is an overspill of air near the velocity outlet indicated by the green colored temperature and the red colored y-velocity. The air curtain overspill was also observed at the lower end of the frontal opening of the cabinet during the smoke experiment, as discussed in section 2.5.5. Figure 76 shows the streamlines of the Fri-Jado geometry. Note that again recirculation is visible at the bottom of the simulation domain. However, this time the recirculation region is located farther away from the air curtain due to the extended bottom boundary, having less impact on the entrainment of the ambient air. Finally, figure 77 shows a comparison between the IR image of the frame placed in the middle of the cabinet and the simulated temperature field of the air curtain. From this figure, one can see again that the air curtain thickness is underpredicted by the simulation as a higher temperature gradient from the conservation space to the ambient environment can be observed. Nevertheless, figure 77 shows a reasonable agreement. In conclusion, temperature profiles of the 2D simulation correspond better to the experiment than the 3D simulation due to the more accurate inlet velocity profile and the demarcation of the flow domain. However, it was observed that the total error of the 2D simulation with respect to the experiment decreased with a decreasing mesh fineness. This indicates that there are some modelling errors, which can be partly due to the simplified geometry. In addition, no other comparisons were made for other solution variables, due to the lack of measurement tools during the experiment. Hence no complete validation was possible. Because the temperatures of the 2D coarse mesh are closest to the experimental temperature profiles, this simulation setup will be used for the optimization.

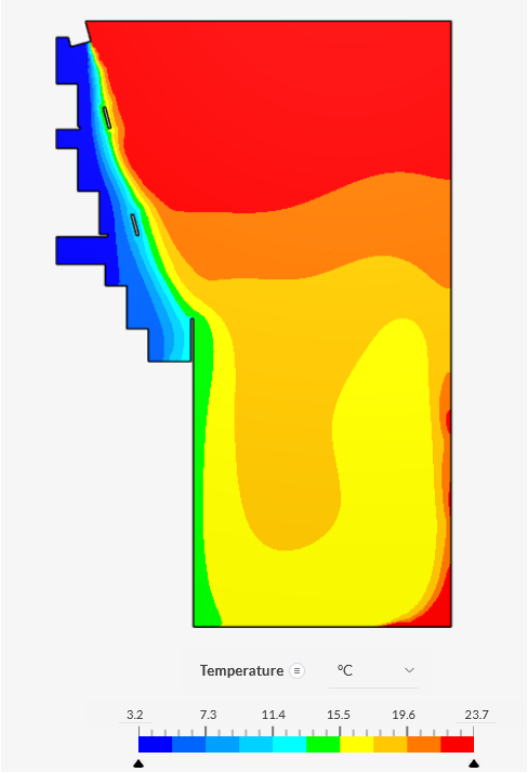

Fig. 74. Contour plot of the temperature field of the Fri-Jado geometry.

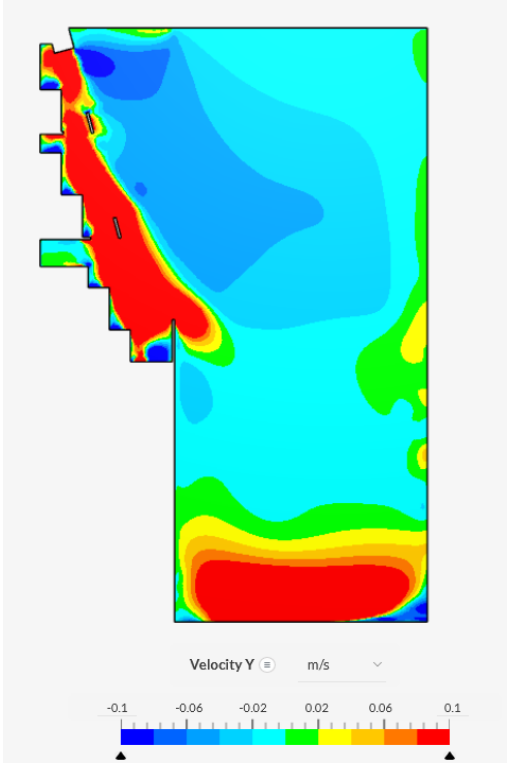

Fig. 75. Contour plot of the y-velocity field of the Fri-Jado geometry.

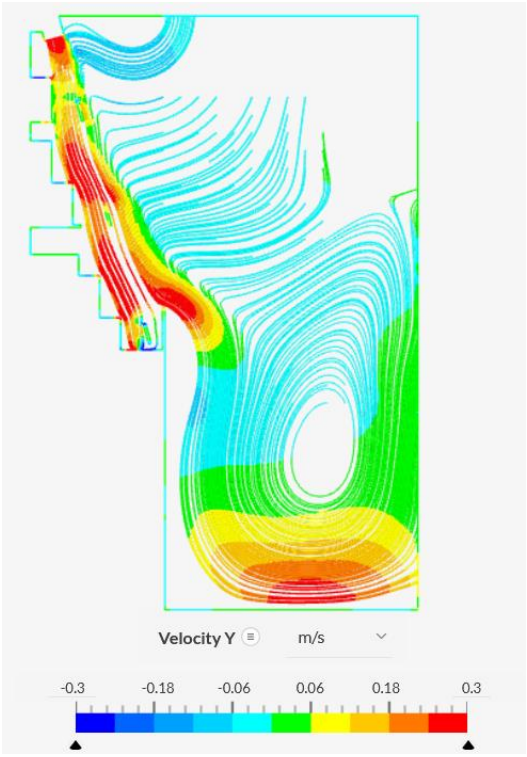

Fig. 76. Streamlines for the Fri-Jado geometry. The color of the streamlines indicates the y velocity magnitude.

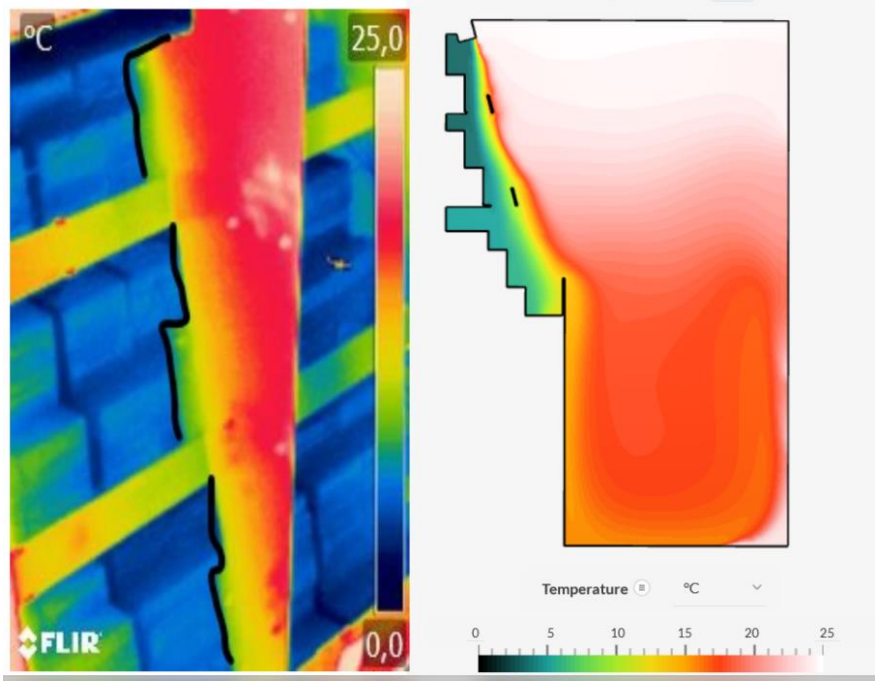

Fig. 77. Left: IR image of the air curtain in the middle of the cabinet. Right: Temperature field of the simulated air curtain

6. Optimization

In this chapter, an attempt to optimize the original Fri-Jado cabinet is performed. As discussed in section 2.3, several performance parameters will be used in this study to optimize the cabinet. The thermal entrainment ratio (equation (5)) and the mass entrainment ratio (equation (10)) can both aid in assessing the performance, while the geometric parameters i.e. the throw (equation (15)) and offset angle change the performance of the Fri-Jado geometry. Note that this study will not focus on optimization by changing the Reynolds number based on V_{jet}, which is affected by changing the rotational speeds of the fans and the slot width. Instead, the influence of a stepped velocity profile will be investigated, which is shown together with the uniform velocity profile in figure 78. As discussed by [33] and Navaz et al. (2006) [65], varying the internal geometry of the upper fan space and the supply can result in different shapes of inlet velocity profiles, which in turn affect the entrainment of the air curtain. To generate these velocity profiles, different types of deflectors can be used in the fan space before the supply, which are a constant gradient deflector for a uniform velocity profile and a twin bend deflector for a stepped velocity profile. In addition, [33] showed experimentally that the stepped velocity profile for the inlet reduced the entrainment of ambient air, which will be tested in this study. Note that the velocity profiles in figure 78 were measured just below the supply with PIV. Therefore, after $\frac{y}{H} \approx 0.8$ (indicated by the black solid line) one can observe the inflection points and the reduction of the velocity to zero, which occurs due to shear with the environment. Therefore, after $\frac{y}{h} \approx 0.8$ is considered to be not a part of the uniform and stepped velocity profiles.

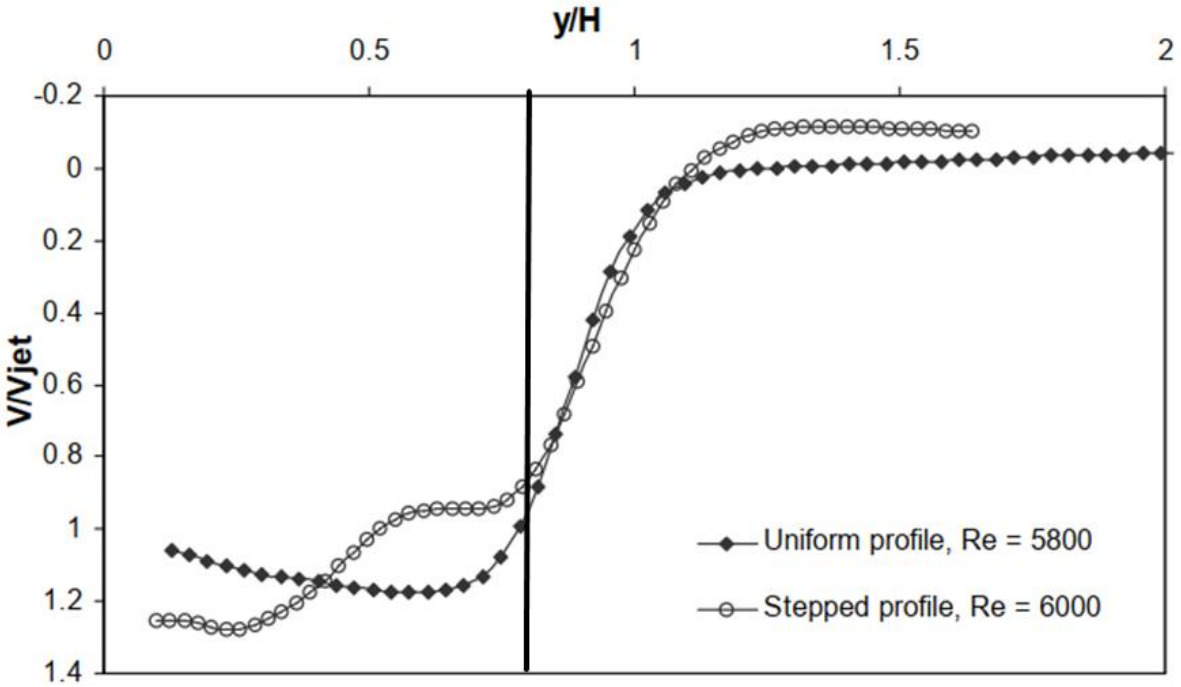

Fig. 78. Uniform and stepped velocity profiles. Adapted from [33]. The part of the velocity profile left of the black solid line is considered to be part of the uniform and stepped velocity profiles.

6.1. Comparison of the Thermal Entrainment and The Mass Entrainment

As a reference the Fri-Jado geometry that was validated in the previous chapter was used to compute the thermal and mass entrainment. The offset angles were varied for 5°, 10° and 15° and the throw angles for 5°,15°,25°,35°,45°. In addition, for each combination of offset and throw angle, the uniform and stepped velocity profile were applied. Note that for a varying throw angle, the velocity in the y direction was calculated with $v_y = v \cdot \sin(\lambda)$ and the velocity in the x-direction with $v_x = v \cdot \cos(\lambda)$, where v is the velocity for a throw angle equal to 0°.

As mentioned in [32], the net thermal entrainment energy loss alone is characterized by the product of the Reynolds number and the thermal entrainment ratio αRe . However, since the Reynolds number was kept constant only the thermal entrainment ratio was used for the comparison.
Figure 79 shows the calculated mass entrainment and thermal entrainment ratios for each configuration. Note that the original configuration of the Fri-Jado geometry had an offset and throw angle of both 15°. In addition, both the relative mass entrainment and thermal entrainment were summed and ordered to represent a total score to assess the performance on the configuration, based on the entrainment parameters. No specific trend was found during optimization. However, the results suggest that an offset angle of 10°, a throw angle of 25° and a stepped velocity profile perform best.

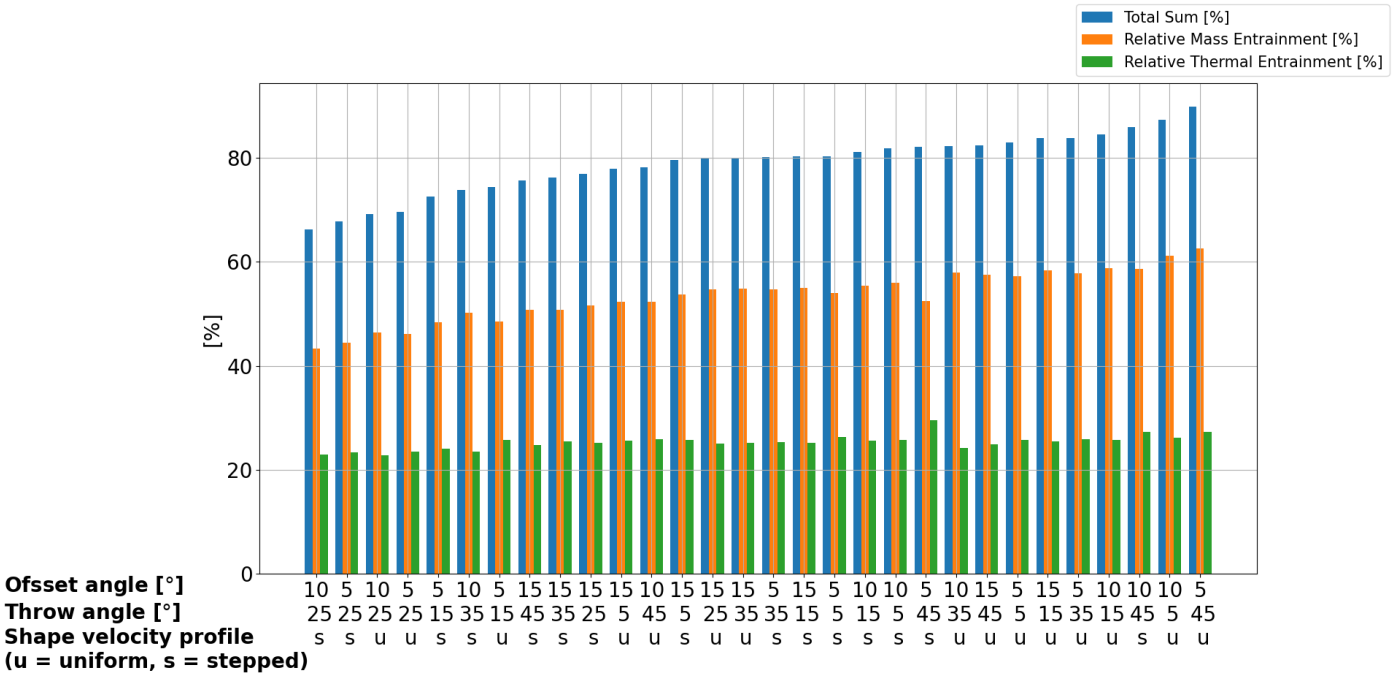

Fig. 79. Relative mass entrainment and thermal entrainment for different throw angles and offset angles. Note that the color changes with the offset angle. In addition, circles represent a uniform velocity profile and squares represent a stepped velocity profile.

7. Discussion, Conclusion & Recommendations

The goal of this research was to provide an answer to the main research question:

How can the air curtain of an open vertical refrigerated display cabinet design without a PBP be optimized, by making use of the hybrid CFD method?

for which the relevance is stated in chapter 1. In addition, eight different sub-questions were formulated to support the main research question. Therefore, this chapter provides an answer to the main research question by answering and discussing the sub questions.

7.1. What performance parameters can be used for optimization of the cabinet?

In section 2.3 literature was reviewed that discussed experimental techniques and performance parameters. In total, nine different performance parameters were identified, which are listed in table 2. It has to be noted that these performance parameters and experimental techniques can be of use for optimization in different ways i.e. performance parameters that evaluate a design and performance parameters that are used to modify the design.

Performance parameters that evaluate the design are the thermal entrainment ratio and the mass entrainment ratio, as they give an indication on the amount of (ambient) air that infiltrates or is spilled by the air curtain. Experimentally, one can get an indication on the infiltration by measuring the amount of condensate coming from the evaporator, because a lot of condensate is coming from the ambient. It was found that on average a total of 0.066 g/s condensate was discharged by the Fri-Jado cabinet, which is equal to a significant latent heat load of 150W in comparison with a total average refrigeration power that is equal to 650W. Considering the fact that the climate cell conditions were 24°C and 55% RH i.e. approximately 10.3 $\frac{\text{g water}}{\text{kg air}}$, the absolute infiltration rate of ambient air equals 6.4 $\frac{\text{g air}}{\text{second}}$ which is about 8% of the air flow sucked in at the return. This finding stresses the relevance of the infiltration problem.

For the simulation, one can evaluate the amount of ambient air that infiltrates the air curtain by using equation (10). In addition, equation (5) describes the thermal entrainment ratio which can be used both experimentally and in the simulation. For the experiment it should be stressed that the temperatures are measured in a well-mixed flow i.e. before the supply and after the return.

Performance parameters that modify the design are the remainder of the parameters which are listed in table 2. In addition, the inlet velocity profile was varied. For this study, the only geometric parameters that were used were the throw and offset angles. However, it would also be interesting to see the effects of varying the slot width on the air curtain because it will certainly have an effect on the air curtain performance. Besides these geometric parameters, varying the fan speeds would also be an interesting optimization study.

7.2. What are the physics of the air curtain?

In section 2.4, the physics of the air curtain were discussed. The Fri-Jado air curtain is known as a buoyant jet, where the air starts to accelerate due to density differences of the cold supplied air with respect to the ambient. Moreover, because of Kelvin-Helmholtz vortices the potential core disappears. Based on the data gathered during the experimental testing a Richardson number of 0.25 was calculated, indicating that both natural and forced convection play a role in the physics of the air curtain. These types of cons were present in the simulation.

Besides measuring the condensate discharge of the Fri-Jado cabinet, the entrainment of ambient air was also proven by applying infrared thermography, which is described in section 2.4.2. Using this experimental technique in combination with a grey zinc spray coated frame, thermal images of the air curtain were made. These images showed that entrainment is certainly present in the cabinet, albeit that lower temperature gradients over the frame were observed near the sides of the cabinet. Note that an air curtain starts to grow in width by sucking air. Consequently, the air gets entrained by mixing and the temperature gradient across the air curtain reduces as the air curtain thickness increases. The increased entrainment near the sides of the cabinet is likely to occur due to the lateral crossflow, which generates vortices near the sides of the cabinet, causing an additional amount of ambient air that is drawn in.

7.3. What Benchmark Tests Are Needed To Validate The Commercial Simscale Package?

Chapter 3 provided an in-depth discussion on what simulation setup should be used for the optimization based on the retrieved literature. Firstly, the pros and cons between performing a steady state or a transient simulation were discussed in section 3.1. The literature suggested that a steady state simulation is a better fit for optimization purposes and requires less computational resources. Therefore, the decision was made to only perform a steady-state simulation.

As mentioned in section 3.2, no one in the literature succeeded to properly simulate and validate an entire cabinet simulation because of its complexity. Moreover, only one study attempted to include the entire 3D structure of the cabinet [20], albeit a simplified version. Others tried to simulate a demarcated air curtain in combination with the crossflow in 3D, excluding the conservation space and internal geometry of the cabinet. It was shown that the use of the $k-\varepsilon$ model and more general a RANS model was not sufficient to capture all the characteristics of the flow, while using a LES turbulence model showed better results.
On the other hand, Simscale provided a 3D simulation of the entire cabinet excluding the crossflow, using a conjugate heat transfer and the $k-\omega$ SST turbulence model. For this simulation a total of 14 million cells were used and 157.1 core hours were needed for the meshing and the simulation. In addition, comparisons between experiment and simulation were made for the M-package temperatures and the air curtain temperature distributions. While there was some qualitative agreement for the trend in which the M-package temperature changes along the $\frac{x}{L}$ direction, they were deviating quantitatively with respect to the measured temperatures. Moreover, some qualitative agreement was found between the simulation and the experiment for the air curtain temperature profiles. However, the comparison mostly showed significant inaccuracies, especially near the supply and shelf 3. In addition, the simulation results were difficult to assess because of the many ascribed boundary conditions, used models and further simplifications in physics. The simulation had a cost of 157 core hours, being an expensive simulation considering the fact that Fri-Jado performed 54 iterations for optimizing their cabinet as mentioned in section 2.2 and had purchased a Simscale package that included 10000 core hours. Furthermore, the turbulence model that was used is proven by [50] to not capture all the flow characteristics, clearly indicating that much more computational power is needed in order to get a correct representation of the flow and temperature field of the entire cabinet. Finally, significant assumptions for the boundary conditions of the 3D simulation were made, which could be the cause for additional inaccuracy. Therefore, one can wonder what alternative possibilities are available to use CFD for optimizing the cabinet.
As mentioned in chapter 3, literature [48][10] suggested that optimization studies can be performed by using a 2D simulation of the cabinet. The air curtain can be modelled as a buoyant jet as mentioned in section 2.4. Because this is a fundamental flow, many experimental studies are performed on this flow type, making the simulation easier to validate. In addition, it is known that the air curtain is subjected to the Kelvin Helmholtz instability which cannot be properly simulated by using a RANS turbulence model, as it assumes isotropic turbulence. Moreover, there are only RANS turbulence models available in the purchased Simscale package, making this package not suited for exact modelling of the air curtain. Finally, it was decided to further simplify the simulation domain by leaving out the conservation space and internal geometry of the cabinet, as mentioned in section 3.3. Due to these simplifications, one can also make an easier assessment of the used modelling approach and performance of the CFD software. In conclusion, it was decided to perform a 2D RANS simulation of the air curtain, leaving out the conservation space and internal geometry.
In section 3.4, relevant benchmark tests that were performed in the past by Simscale were reviewed. Again, the lack of accuracy due to the implementation of a RANS turbulence model was validated in the benchmark test for a datacenter. While the benchmark test for the natural convection between heated plates showed nice results for $Ra = 0.86 \cdot 10^6$, no validation was made for higher Rayleigh numbers that are applicable to the cabinet. In addition, it has to be pointed out that the physics of the air curtain of the case study cabinet are a mixed convection case. No mixed convection benchmark tests are available on the Simscale website. Therefore, additional benchmark tests for a non-isothermal air curtain that included mixed convection were later performed.

7.4. What numerical methods should be used for the simulation?

Chapter 4 and appendix E discussed the available numerical methods in the commercial Simscale package. It was found that Simscale is mostly based on Open foam ®, which is an open source CFD software that discretizes the relevant governing equations (see chapter 4) by making use of the second order finite volume method. Because it was not recommended to generate 2D meshes on the Simscale platform (see sections 4.1 and 5.2), Ansys was used instead. In addition, RANS models were the only available turbulence models in the software package. To account for possible separation of the air curtain, the $k-\omega$ SST was applied. To account for near wall effects, inflation layers were used with a first layer cell height based on $y^+ < 5$. Note that it was also possible to use wall functions, although this option was not further explored. The method for determining the first layer cell height is described in section 5.2. For including natural convection, two different methods were available: The Boussinesq approximation and the weakly compressible flow formulation. The results and performance of both methods were later compared. For the discretization, the Gauss-seidel method was used for resolving all the solution fields, except for the pressure for which the GAMG solver was used. These solvers were the preset for the use of mixed convection that Simscale

recommended. The diffusion and convection terms were interpolated using the Gauss scheme and gradients were computed using the second order least squares methods, in order to account for the skewness error which is possible for non-orthogonal meshes. While the selected numerical methods, showed that the mesh was sufficiently converged for the simulation of the Fri-Jado geometry in section 5.8, it would be interesting to compare the performance of different solvers and numerical schemes with each other, in order to get a better picture of the background behind the discretization errors.

7.5. What is the accuracy of the benchmark test(s)?

In the first half of chapter 5, two benchmark tests were performed for an isothermal and non-isothermal air curtain. For both benchmarks, the methodology for the simulation setup was discussed before performing the simulation in sections 5.1-5.4. The goal was to achieve a y^+ smaller than 5 at the wall to which the air curtain was bound, since the $k-\omega$ SST turbulence model was used. Both the meshes that were used for the isothermal and non-isothermal air curtain showed that all the y^+ values that were adjacent to the wall to which the air curtain was bounded were below 5, showing that a sufficient inflation layer sizing was applied.

In addition, velocity profiles were compared to experimental velocity profiles that were obtained by [32] and [60] using PIV. For the isothermal air curtain, a good agreement between the velocity profiles was shown until $\frac{z}{b} = 8.7$, while for the non-isothermal air curtain a good agreement between the velocity profiles was shown until $\frac{z}{b} = 3.6$. More downstream with respect the aforementioned coordinates the velocity profiles became overpredicted due to the fact that the simulation was 2D and because of the implemented RANS turbulence models. For the non-isothermal air curtain, the overprediction of the velocity profiles was significantly less than the velocity profiles for the isothermal air curtain, because the overprediction was mitigated by the buoyant acceleration that was also present during the experiment. Both the non-isothermal simulations in which the Boussinesq approximation and the weakly compressible flow were applied, showed similar results for the velocity profiles.

Furthermore, the evolution of the air curtain thickness was compared to experimental values retrieved from literature. [32][60]. For the isothermal air curtain, the error between simulation and experiment remained under 10% until $\frac{z}{b} = 9.4$, while for the non-isothermal air curtain the error remained under 10% until $\frac{z}{b} = 5.4$ being significantly less. However, it has to be noted that the length of the Fri-Jado frontal opening height equals 0.7m which is smaller than the frontal opening height of the cabinet that was used for the benchmark test, having a total length of 1.6m. Both the Boussinesq approximation and the weakly compressible flows showed a similar prediction of the air curtain thickness, although it has to be noted that the Boussinsq approximation took significantly longer to converge (i.e. 10000 iterations for Boussinesq and 4000 iterations for weakly compressible). In addition, the convergence of the simulation with the Boussinesq approximation showed an increase in the total error. Moreover, the minimum temperatures that can occur in the Fri-Jado cabinet are -1°C and the maximum temperature that occur in the climate chamber equals 24 °C, while the Boussinesq approximation is recommended to be used for temperature differences below 15°C. Therefore, the weakly compressible flow was applied to the Fri-Jado geometry. Finally, the benchmark geometry with an inclined open boundary in combination with the weakly compressible flow formulation was simulated, in order to reduce the recirculation at the end of the air curtain. It was observed that the inclined boundary had a positive impact on the air curtain by reducing the recirculation which was caused by the open boundary, although the effect was not very significant.

7.6. What is the accuracy of the air curtain simulation used for optimization?

The second part of chapter 5 described and discussed the simulation for the Fri-Jado geometry.

The Fri-Jado geometry used a similar velocity inlet that was also used for the non-isothermal benchmark test. In addition, a velocity outlet instead of a pressure outlet was used to mitigate the bending near this outlet as was observed during the benchmark tests.

A mesh convergence study was performed to assess the discretization error. The comparison of the simulated air curtain temperature profiles with the experiment showed that the coarse mesh was sufficient for optimization purposes. Finally, the temperature and y-velocity contour plots showed some qualitative agreements with the temperature measurements and the smoke test. Note that a Reynolds number equal to 8000 was applicable to the conditions under which the benchmark test took place. Since the Fri-Jado cabinet has a lower Reynolds number, the benchmark tests were not completely applicable. However, the inlet velocity profile that was used for the Fri-Jado geometry was converted using the Reynolds number that corresponds to the Fri-Jado geometry. This time, no validation for the air curtain thickness and velocity profiles was possible, due to a lack of data. Despite this fact, the temperature profiles

also gave an indication of the air curtain thickness, which showed a reasonable agreement for the Fri-Jado geometry between the simulation and experiment. Therefore, by combining the comparison of the velocity profiles and air curtain thicknesses of the benchmark tests and the temperature profile assessment of the Fri-Jado geometry, one could say that the simulation is validated with the corresponding Reynolds number.

7.7. What is the interaction between the design parameters and what modifications can be made to the cabinet?

Once the simulation was validated in chapter 5, an optimization study was performed in chapter 6. Besides the offset and throw angles that were identified as performance parameters in chapter 2, the shape of the velocity profile was also varied as a uniform and stepped shape. The throw angles were varied from 5° until 45° , with stepsizes of 10°, while the offset angle was varied for 5°, 10° and 15°. For each possible configuration a simulation run was performed, in which the results are shown in figure 79. In figure 79, the thermal entrainment and mass entrainment ratio are depicted for each configuration. It was found that for offset angles of 5° and 10°, both the thermal entrainment and mass entrainment changed more significantly with respect to an offset angle of 15° by varying the throw angle. No specific trend was found, although it is certain that the entrainment ratios are influenced by the buoyancy and inertial forces. According to these simulations a combination offset and throw angles equal to 10° and 25° and a stepped velocity profile performs best.

7.8. Final Remaks

It has to be noted that many assumptions were made during this study. Therefore, the impact of the simulation of the Fri-Jado geometry remains uncertain until experimental evidence is obtained. One could apply the best performing configurations found during the optimization study to the Fri-Jado cabinet to validate these simulations. If a bad agreement is found, it could be an indication that the simulation included too many assumptions. If this would be the case, one could try to expand the simulation domain by including the conservation space and internal geometry and/or prescribe velocity boundary conditions to the gaps in between the M-packages and shelves that were modelled as walls. Moreover, while the best performing configuration showed that the stepped velocity profile performed better than the uniform velocity profile, it remains uncertain what alterations should be made to the Fri-Jado geometry in order to produce this shape. It was mentioned in chapter 6 that a twin bend deflector in the fan space before the supply produces a stepped velocity profile and a constant gradient deflector produces a uniform velocity profile. However, remark that no further details are present on the shape of the geometry and a different type of cabinet/ geometry was used. One could try to simulate the upper fan space and couple the outlet velocity profile of the supply to the inlet velocity profile of the air curtain that was simulated in this study.

Bibliography

[1] Dupont , J. L., Domanski, P., Lebrun, P., & Ziegler, F. (2019, June 1). *The role of refrigeration in the global economy (2019), 38th note...* The Role of Refrigeration in the Global Economy (2019), 38th Note... Retrieved December 3, 2021, from https://iifiir.org/en/fridoc/142028.

[2] Agarwal, R., Anderson, J., Bivens, D., Colbourne, D., Hundy, G., König, H., Lundqvist, P., McInerney, E., & Nekså, P. (2018). *SROC Chapter 4: Refrigeration*. IPCC. Retrieved December 3, 2021, from https://www.ipcc.ch/report/safeguarding-the-ozone-layer-and-the-global-climate-system/refrigeration/.

[3] Grof, T. (2009). Greening of industry under the montreal protocol. *United Nations Industrial Development Organization (UNIDO)*, 30.

[4] Amrane, K. (2019). Reducing the Carbon Footprint of Commercial Refrigeration Equipment.

[5] Lindberg, U., & Jensen, S. (2014). How could a lower temperature in the cold chain affect food waste. *Refrigeration Science and Technology*, 540-547.

[6] Dudeja, P., & Singh, A. (2017). Food safety in large organized eating establishments. In *Food Safety in the 21st Century* (pp. 339-353). Academic Press. [7] Little, A. D., Westphalen, D., Zogg, R. A., Varone, A. F., & Foran, M. A. (1996). *Energy Savings Potential for Commercial Refrigeration Equipment*. Arthur D. Little

[7] NOS. (2022). https://nos.nl/artikel/2437896-parijse-winkels-met-airco-aan-moeten-deuren-dichthouden

[8] Westphalen, D., Zogg, R. A., Varone, A. F., Foran, M. A., Brodrick, J. R., & DuBois, T. (1996). Energy savings potential for commercial refrigeration equipment. *Final Report Prepared for Building Equipment Division Office of Building Technologies*.

[9] Faramarzi, R. (1999). Efficient display case refrigeration. *ASHRAE journal*, *41*(11), 46.

[10] Navaz, H. K., Amin, M., Faramarzi, R., Kehtarnavaz, N., Kamensky, K., & Nowakowski, A. (2015). Airflow Optimization in Retail Cabinets and the Use of CFD Modelling to Design Cabinets. *Sustainable Retail Refrigeration*, 63.

[11] Fricke, B., & Becker, B. (2010). Energy use of doored and open vertical refrigerated display cases. *International Refrigeration and Air Conditioning Conference*

[12] Gaspar, P. D., Gonçalves, L. C., & Pitarma, R. A. (2011). Experimental analysis of the thermal entrainment factor of air curtains in vertical open display cabinets for different ambient air conditions. *Applied Thermal Engineering*, *31*(5), 961-969.

[13] Chaomuang, N., Flick, D., & Laguerre, O. (2017). Experimental and numerical investigation of the performance of retail refrigerated display cabinets. *Trends in Food Science & Technology*, *70*, 95-104.

[14] Laguerre, O., Hoang, M. H., & Flick, D. (2012). Heat transfer modelling in a refrigerated display cabinet: the influence of operating conditions. *Journal of Food Engineering*, *108*(2), 353-364.

[15] Zhijuan, C., Xuehong, W., Yanli, L., Qiuyang, M., & Wenhui, Z. (2013). Numerical simulation on the food package temperature in refrigerated display cabinet influenced by indoor environment. *Advances in Mechanical Engineering*, *5*, 708785.

[16] Chen, Y. G., & Yuan, X. L. (2005). Experimental study of the performance of single-band air curtains for a multi-deck refrigerated display cabinet. *Journal of food engineering*, *69*(3), 261-267.

[17] International Organization for Standardization (2015, December). *ISO 23953-2:2015 refrigerated display cabinets - part 2: Classifications, requirements and test conditions*. ISO 23953-2:2015 Refrigerated display cabinets Part

2: Classification, requirements and test conditions. Retrieved December 10, 2021, from https://www.iso.org/standard/62002.html.

[18] Norton, T., & Sun, D. W. (2006). Computational fluid dynamics (CFD)–an effective and efficient design and analysis tool for the food industry: a review. *Trends in Food Science & Technology*, *17*(11), 600-620.

[19] Cortella, G. (2002). CFD-aided retail cabinets design. *Computers and electronics in agriculture*, *34*(1-3), 43-66.

[20] D'Agaro, P., Cortella, G., & Croce, G. (2006). Two-and three-dimensional CFD applied to vertical display cabinets simulation. *International Journal of Refrigeration*, *29*(2), 178-190.

[21] Ge, Y. T., & Tassou, S. A. (2001). Simulation of the performance of single jet air curtains for vertical refrigerated display cabinets. *Applied Thermal Engineering*, *21*(2), 201-219.

[22] Ge, Y. T., Tassou, S. A., & Hadawey, A. (2010). Simulation of multi-deck medium temperature display cabinets with the integration of CFD and cooling coil models. *Applied Energy*, *87*(10), 3178-3188.

[23] Gaspar, P. D., Gonçalves, L. C., & Pitarma, R. A. (2012). Detailed CFD modelling of open refrigerated display cabinets. *Modelling and Simulation in Engineering*, *2012*.

[24] European Union. (2019). COMMISSION DELEGATED REGULATION (EU) 2019/2018 of 11 March 2019 Supplementing Regulation (EU) 2017/1369 of the European Parliament and of the Council with Regard to Energy Labelling of Refrigerating Appliances with a Direct Sales Function, 1–32.

[25] Fri-jado. (2021). Personal interview

[26] Simscale. (2021). www.simscale.com

[27] Sun, J., Tsamos, K. M., & Tassou, S. A. (2017). CFD comparisons of open-type refrigerated display cabinets with/without air guiding strips. *Energy Procedia*, *123*, 54-61.

[28] Evans, J. A., Scarcelli, S., & Swain, M. V. L. (2007). Temperature and energy performance of refrigerated retail display and commercial catering cabinets under test conditions. *International Journal of Refrigeration*, *30*(3), 398-408.

[29] Danjoux, R., Pastor, R. R., & Thunevin, S. (2010). Visualization of air flows with an infrared camera: presentation of a simple technique and examples of data analysis. *FLIR Technical Series, Application Note for Research & Science*.

[30] Gaspar, P. D., Gonçalves, L. C. C., & Pitarma, R. A. (2007). Experimental analysis of the thermal entrainment three dimensional effects in re-circulated air curtains.

[31] Navaz, H. K., Henderson, B. S., Faramarzi, R., Pourmovahed, A., & Taugwalder, F. (2005). Jet entrainment ratio in air curtain of open refrigerated display cases. *International Journal of Refrigeration*, *28*(2), 267-275.

[32] Field, B. S., & Loth, E. (2006). Entrainment of refrigerated air curtains down a wall. *Experimental Thermal and Fluid Science*, *30*(3), 175-184.

[33] Kalluri, R. R., & Loth, E. (2003). *Parametric study of negatively-buoyant wall jets and air curtains*. Air Conditioning and Refrigeration Center. College of Engineering. University of Illinois at Urbana-Champaign.

[34] Gray, I., Luscombe, P., McLean, L., Sarathy, C. S. P., Sheahen, P., & Srinivasan, K. (2008). Improvement of air distribution in refrigerated vertical open front remote supermarket display cases. *International Journal of Refrigeration*, *31*(5), 902-910.

[35] Field, B., Kalluri, R., & Loth, E. (2002). PIV investigation of air-curtain entrainment in open display cases. *IIF-II-Commission D1/B1*.

[36] Navaz, H. K., Faramarzi, R., Gharib, M., Dabiri, D., & Modarress, D. (2002). The application of advanced methods in analyzing the performance of the air curtain in a refrigerated display case. *J. Fluids Eng.*, *124*(3), 756-764.

[37] Amin, M., Dabiri, D., & Navaz, H. K. (2009). Tracer gas technique: A new approach for steady state infiltration ratio measurement of open refrigerated display cases. *Journal of Food Engineering*, *92*(2), 172-181.

[38] Amin, M., Dabiri, D., & Navaz, H. K. (2011). Comprehensive study on the effects of fluid dynamics of air curtain and geometry, on infiltration ratio of open refrigerated cavities. *Applied thermal engineering*, *31*(14-15), 3055-3065.

[39] Amin, M., Dabiri, D., & Navaz, H. K. (2012). Effects of secondary variables on infiltration ratio of open refrigerated vertical display cases with single-band air curtain. *Applied thermal engineering*, *35*, 120-126.

[40] Hayes, F. C., & Stoecker, W. F. (1969). Design data for air curtains. *Ashrae Transactions*, *75*(2), 168-180.

[41] Foster, A. M., Swain, M. J., Barrett, R., D'agaro, P., & James, S. J. (2006). Effectiveness and optimum jet velocity for a plane jet air curtain used to restrict cold room infiltration. *International journal of refrigeration*, *29*(5), 692-699.

[42] Gonzales, J., & Kaye, N. B. (2021). An entrainment model for air curtain effectiveness. *Building and Environment*, 108576

[43] Blevins, R. D. (1984). Applied fluid dynamics handbook. *New York*

[44] Sekula, E., & Redondo, J. M. (2008). The structure of turbulent jets, vortices and boundary layer: Laboratory and field observations. *Il nuovo cimento C*, *31*(5\6), 893-907.

[45] FLIR (2022). T series user's manual.

[46] Testo (2022). Testo 425 thermal anemometer user's manual

[47] ATAL (2022). ATAL ATV 11R user's manual

[48] Artico, G., Mousset, S., & Fortini, D. (2008). Performance Evaluation and Design Optimization of Refrigerated Display Cabinets Through Fluid Dynamic Analysis.

[49] Smale, N. J., Moureh, J., & Cortella, G. (2006). A review of numerical models of airflow in refrigerated food applications. *International Journal of Refrigeration*, *29*(6), 911-930.

[50] Moureh, J., & Yataghene, M. (2017). Large-eddy simulation of an air curtain confining a cavity and subjected to an external lateral flow. *Computers & Fluids*, *152*, 134-156.

[51] Foster, A. M., Madge, M., & Evans, J. A. (2005). The use of CFD to improve the performance of a chilled multi-deck retail display cabinet. *International Journal of Refrigeration*, *28*(5), 698-705.

[52] Wibron, E., Ljung, A. L., & Lundström, T. S. (2018). Computational fluid dynamics modeling and validating experiments of airflow in a data center. *Energies*, *11*(3), 644.

[53] Betts, P. L., & Bokhari, I. H. (2000). Experiments on turbulent natural convection in an enclosed tall cavity. *International Journal of Heat and Fluid Flow*, *21*(6), 675-683.

[54] Jasak, H. (1996). Error analysis and estimation for the finite volume method with applications to fluid flows.

[55] Liu, F. (2016). A thorough description of how wall functions are implemented in OpenFOAM. *Proceedings of CFD with OpenSource software*, 1-33.

[56] Ferziger, J. H., Perić, M., & Street, R. L. (2002). *Computational methods for fluid dynamics* (Vol. 3, pp. 196-200). Berlin: springer.

[57] Launder, B. E., & Spalding, D. B. (1983). The numerical computation of turbulent flows. In *Numerical prediction of flow, heat transfer, turbulence and combustion* (pp. 96-116). Pergamon.

[58] Launder, B. E., & Sharma, B. I. (1974). Application of the energy-dissipation model of turbulence to the calculation of flow near a spinning disc. *Letters in heat and mass transfer*, *1*(2), 131-137.

[59] Wilcox, D. C. (1998). *Turbulence modeling for CFD* (Vol. 2, pp. 103-217). La Canada, CA: DCW industries.

[60] Field, B. S., & Loth, E. (2004). An air curtain along a wall with high inlet turbulence. *J. Fluids Eng.*, *126*(3), 391-398.

[61] Tennekes, H., Lumley, J. L., & Lumley, J. L. (1972). *A first course in turbulence*. MIT press.

[62] Schlichting, H., & Gersten, K. (2003). *Boundary-layer theory*. Springer Science & Business Media.

[63] Celik, I. B., Ghia, U., Roache, P. J., & Freitas, C. J. (2008). Procedure for estimation and reporting of uncertainty due to discretization in CFD applications. *Journal of fluids Engineering-Transactions of the ASME*, *130*(7).

[64] Ebm-papst (2022). Product datasheet

[65] Navaz, H. K., Amin, M., Rasipuram, S. C., & Faramarzi, R. (2006). Jet entrainment minimization in an air curtain of open refrigerated display case. *International Journal of numerical methods for heat & fluid flow*.

[66] Syrakos, A., Varchanis, S., Dimakopoulos, Y., Goulas, A., & Tsamopoulos, J. (2017). A critical analysis of some popular methods for the discretisation of the gradient operator in finite volume methods. *Physics of Fluids*, *29*(12), 127103.

[67] Jasak, H. (2017). The detail of the Fourth order, least squares scheme [Discussion post]. https://www.cfd-online.com/Forums/openfoam/221454-detail-fourth-order-least-squares-scheme.html

A. Pictures of the cabinet

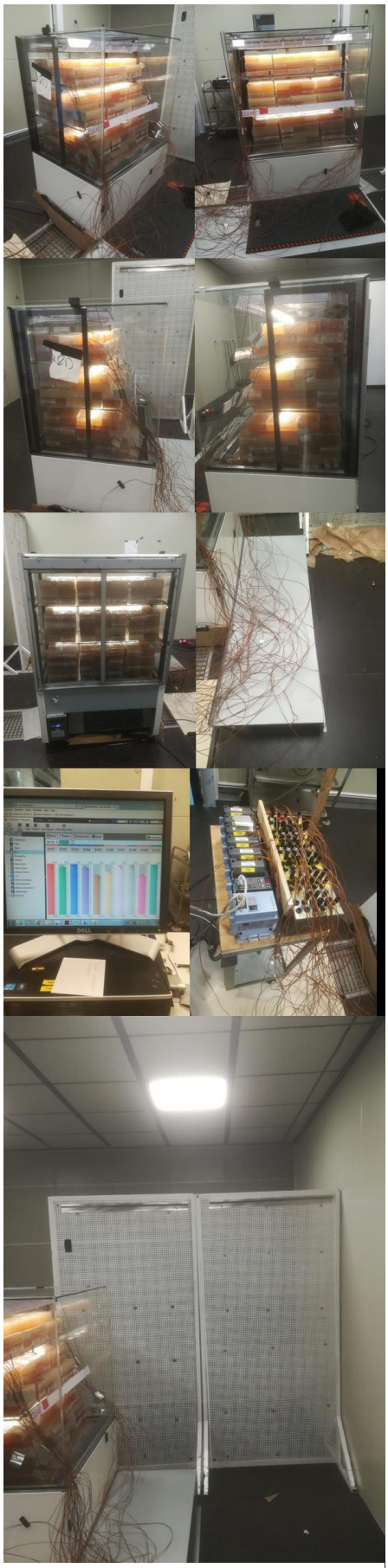

Fig. A1. Pictures of the experimental setup

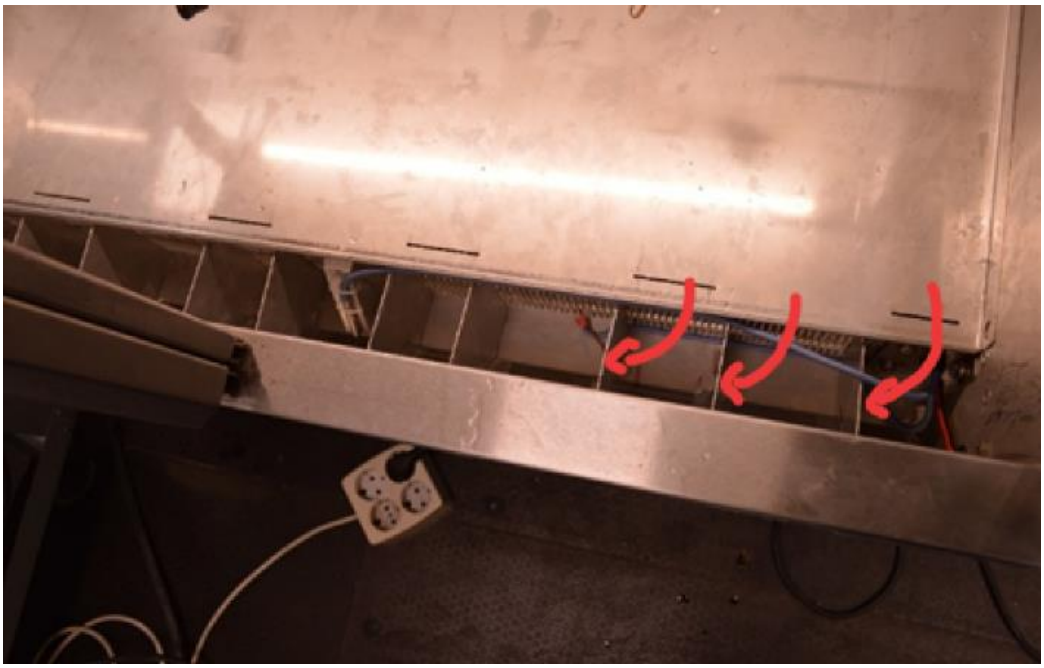

Fig. A2. Inclined fins in the BDAG to direct more air towards the sidewalls, as indicated by the red arrows.

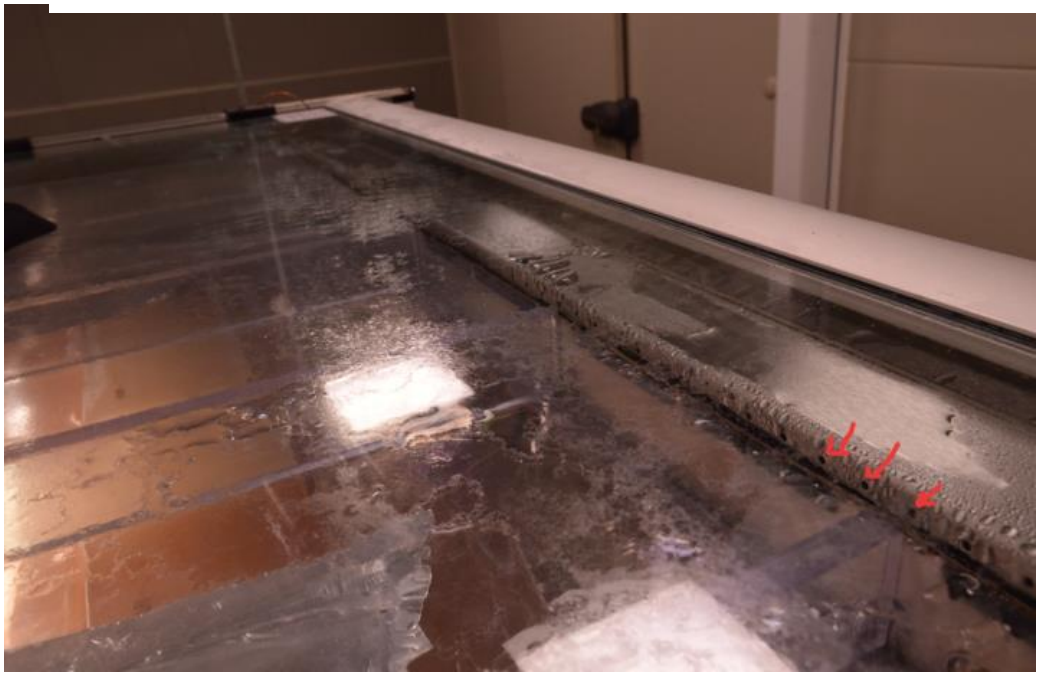

Fig. A3. Circular perforations (as indicated by the red arrows) that were added to the upper fan room to mitigate the condensate film.

B. Air curtain measurement data

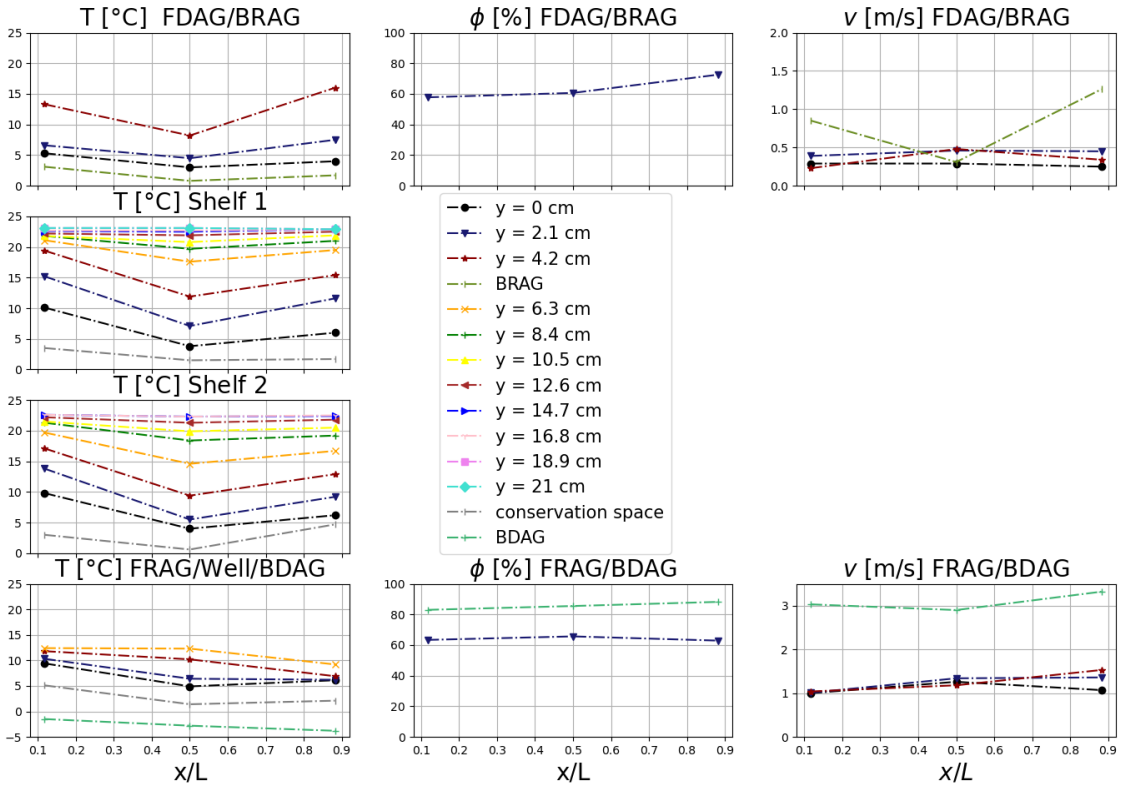

Fig. B1: Measured air curtain data

temperature profile Relative humidity Velocity

Table B1. Measured wall temperatures

Probes	Mean [°C]	Min. [°C]	Max. [°C]	Standard deviation [°C]
Sliding door inside downstream	11.8	11.3	12.9	0
Sidewall downstream inside	4.1	3	8.2	0.1
Sidewall upstream inside	3.6	2.6	7.6	0.1
Sliding door upstream inside	12	11.4	13	0
Sidewall outside downstream	20.6	20.0	21.0	0
Sliding door outside downstream	14.4	13.8	15.2	0
Sliding door outside upstream	14.4	13.8	15.5	0
Sidewall downstream outside	20.4	19.9	21.1	0

C. M-package Temperature Test Data

C1. Old complete M-package dataset

Table C1. Position of the M-package when standing in front of the cabinet and measured maximum and minimum temperatures after the 54th iteration (old test).

Reference	Position	Minimum Temperature (° C)	Maximum Temperature (° C)
M1	Shelf 1 Back Top Left	0.4	0.9
M2	Shelf 1 Back Bottom Left	-0.7	0.1
M3	Shelf 1 Back Top Center	0.3	1
M4	Shelf 1 Back Bottom Center	0.1	0.6
M5	Shelf 1 Back Top Right	0.1	0.7
M6	Shelf 1 Back Bottom Right	1.1	1.6
M7	Shelf 1 Front Top Left	2.8	3.2
M8	Shelf 1 Front Bottom Left	3.2	3.6
M9	Shelf 1 Front Top Center	3.7	4.5
M10	Shelf 1 Front Bottom Center	4.3	4.9
M11	Shelf 1 Front Top Right	2.2	2.8
M12	Shelf 1 Front Bottom Right	4.2	4.9
M13	Shelf 2 Back Top Left	0.6	1
M14	Shelf 2 Back Bottom Left	0.2	0.7
M15	Shelf 2 Back Top Center	0.7	1.1
M16	Shelf 2 Back Bottom Center	-0.3	0.0
M17	Shelf 2 Back Top Right	1.9	2.3
M18	Shelf 2 Back Bottom Right	-0.4	0.3
M19	Shelf 2 Front Top Left	2.8	3.1
M20	Shelf 2 Front Bottom Left	4.4	4.7
M21	Shelf 2 Front Top Center	3.9	4.2
M22	Shelf 2 Front Bottom Center	3.2	3.9
M23	Shelf 2 Front Top Right	2.8	3.3
M24	Shelf 2 Front Bottom Right	4.5	4.8
M25	Well Back Top Left	1.3	1.5
M26	Well Back Bottom Left	0.7	1.3
M27	Well Back Top Center	-0.4	0.1
M28	Well Back Bottom Center	0.7	1.1
M29	Well Back Top Right	1.3	1.6
M30	Well Back Bottom Right	0.9	1.3
M31	Well Middle Top Left	2.1	2.4
M32	Well Middle Bottom Left	2.3	2.6
M33	Well Middle Top Center	0.9	1.2
M34	Well Middle Bottom Center	1.2	1.3
M35	Well Middle Top Right	2.0	2.4
M36	Well Middle Bottom Right	1.7	2.1
M37	Well Front Top Left	4.5	5.2
M38	Well Front Bottom Left	4.3	4.6
M39	Well Front Top Center	3.6	4.2
M40	Well Front Bottom Center	4.2	4.9
M41	Well Front Top Right	3.4	3.8
M42	Well Front Bottom Right	3.4	4.1

C2. New complete M-package dataset

Table C2. measured M-package temperatures for the new test.

Number	Mean [°C]	Min. [°C]	Max. [°C]	Standard deviation [°C]
M1	5.6	5.2	5.9	0
M2	5.2	4.8	5.4	0
M3	1.8	1.5	2.1	0
M4	1.1	0.9	1.4	0
M5	1.8	1.6	2	0
M6	1	0.7	1.7	0.1
M7	6.4	6.1	6.6	0
M8	8.6	8.4	8.8	0
M9	3.9	3.7	4.1	0
M10	6.2	6	6.5	0
M11	3.2	3	3.5	0
M12	4.8	4.6	5.1	0
M13	4.8	4.6	5	0
M14	4.7	4.5	5	0
M15	1	0.8	1.4	0
M16	0.8	0.4	1.8	0
M17	2.4	2.2	2.5	0
M18	1.6	1.4	2.1	0
M19	8.1	7.8	8.2	0
M20	9	8.8	9.4	0
M21	4.4	4.1	4.6	0
M22	4.6	4.4	4.9	0
M23	4	3.9	4.3	0
M24	5.7	5.4	6	0
M25	4.4	4.1	4.9	0
M26	2.4	2.1	2.7	0
M27	0.7	0.5	0.9	0
M28	1.9	1.8	2.1	0
M29	2	1.8	2.2	0
M30	1.4	1.1	1.6	0
M31	6.2	5.8	6.5	0
M32	6.5	6.1	6.8	0
M33	2.7	2.4	3	0
M34	2.9	2.6	3.1	0
M35	4	3.6	4.4	0
M36	3.1	2.9	3.4	0
M37	7.5	7.2	7.8	0
M38	7.1	6.9	7.5	0
M39	3.8	3.5	4.1	0
M40	5.1	4.7	5.4	0
M41	5.6	5.3	5.9	0
M42	4.4	4.1	5	0

C3. M-package dataset for the air curtain temperature test

Table C3. measured M-package temperatures for the new test.

Number	Mean [°C]	Min. [°C]	Max. [°C]	Standard deviation [°C]
M7	5.9	5.7	6.1	0
M8	8.3	8.2	8.4	0
M9	4.5	4.3	4.9	0.1
M10	6.3	6.1	6.5	0
M11	3.2	3	3.4	0
M12	4.7	4.4	4.9	0
M19	7.5	7.4	7.6	0
M20	7.6	7.4	7.8	0
M21	4.5	4.3	4.6	0
M22	4.3	4.1	4.6	0.1
M23	3.6	3.4	3.7	0
M24	4.7	4.4	5	0.1
M37	7	6.8	7.1	0
M38	6.6	6.3	6.8	0.1
M39	3.1	2.9	3.3	0
M40	4.7	4.4	4.9	0.1
M41	4.9	4.7	5.2	0
M42	4.1	3.8	4.4	0.1

D. Thermocouple Locations

D1. Complete M-package measurement

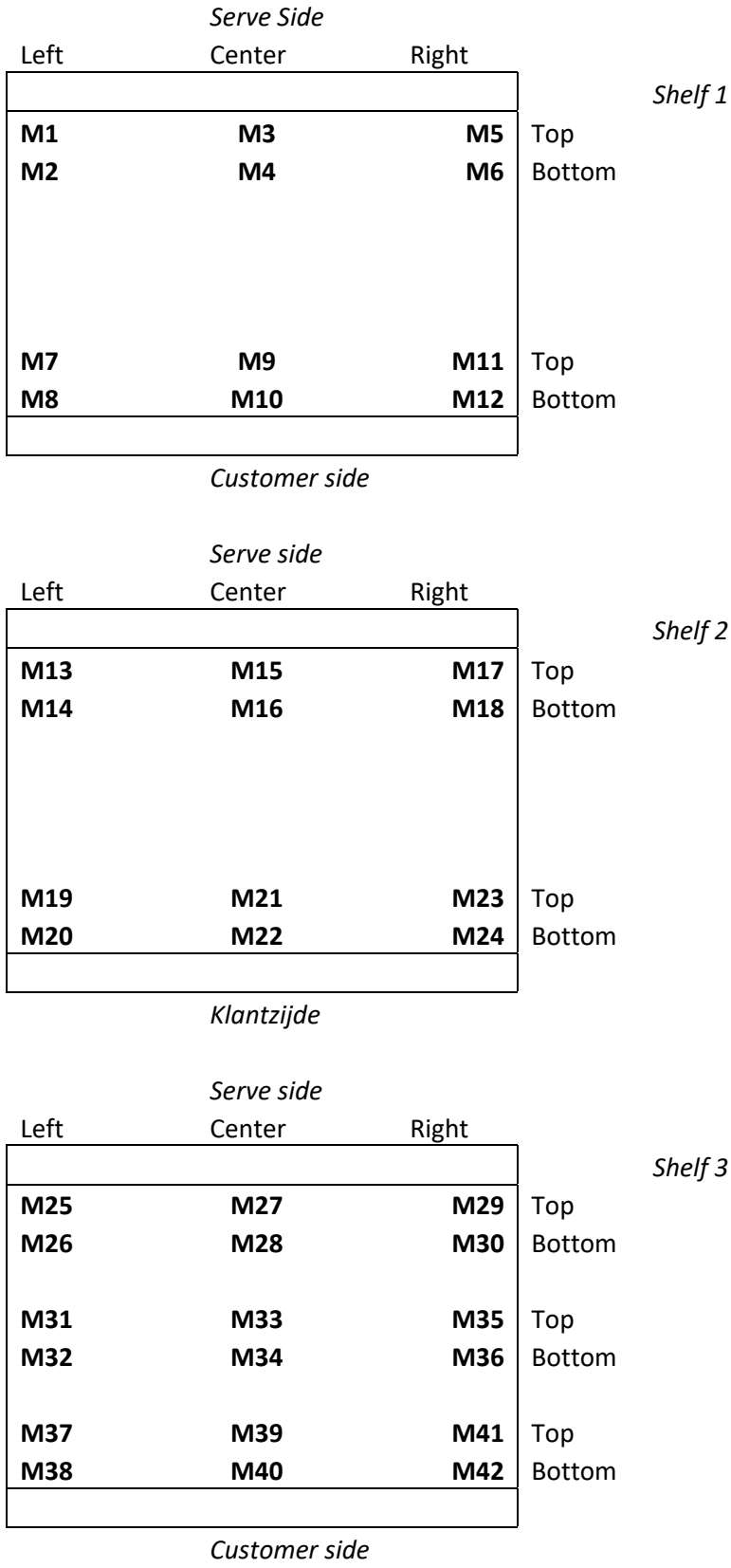

Fig. D1. Allocation of thermocouples in M-packages

D2. M-package measurements during measurements on the air curtain

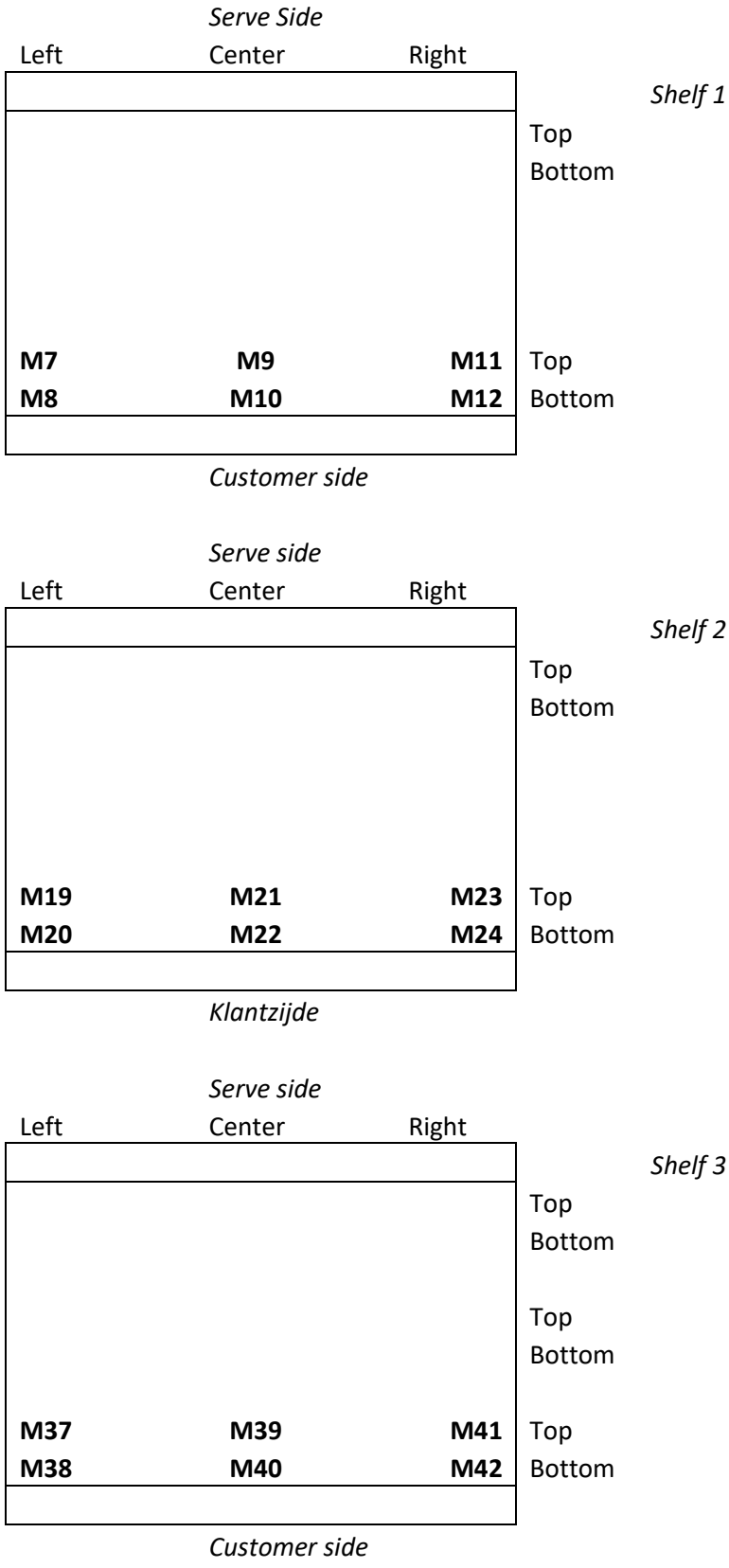

E. Discretization

E1. Mesh Non-orthogonality

The face non-orthogonality θ can be defined as the angle between the unit normal vector **s** of the shared face of two adjacent aligned cells and the distance vector **d** between the two cell centroids **P** and **N** as shown in figure 80. Alternatively, it can be defined as the angle between the unit normal vector **s** of the shared face of two adjacent not aligned cells and the distance vector **c** between cell centroid **P** and the face center, as shown in figure 81.

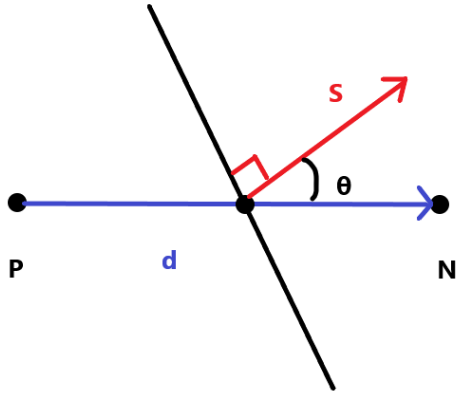

Fig. 80. Vectors **d** and **S** for two aligned cells. The values are stored at the cell centroids **N** and **P**

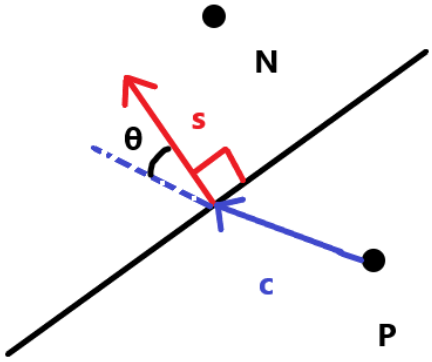

Fig. 81. Vectors c and s for two non-aligned cells

The relevance of mesh non-orthogonality can be understood by studying the diffusion term in the finite volume method, which is used by the OPENFOAM® solvers integrated in the Simscale platform. By integrating the diffusion term over the cell volume and using divergence theorem one can write

$$\int_V [\nabla \cdot (\nu \nabla \boldsymbol{U}) dV = \int_A [\nu (\nabla \boldsymbol{U}) \cdot \boldsymbol{s}] dA \approx \sum_{f=1}^{N} [\nu_f (\nabla \boldsymbol{U})_f \cdot \boldsymbol{s_f}] A_f \tag{69}$$

Whereas ν_f can be obtained from face interpolation, a difficulty arises to compute $(\nabla \boldsymbol{U})_f \cdot \boldsymbol{s_f}$ when the unit normal vector is not parallel to the distance vector $\boldsymbol{d}$. Consequently, $\boldsymbol{s_f}$ can be decomposed into an orthogonal component $\boldsymbol{\Delta_f}$ that is parallel to $\boldsymbol{d}$ and a non-orthogonal component $\boldsymbol{k_f}$, resulting in

$$\sum_{f=1}^{N} [\nu_f (\nabla \boldsymbol{U})_f \cdot \boldsymbol{s}] A_f = \sum_{f=1}^{N} [\nu_f (\nabla \boldsymbol{U})_f \cdot \boldsymbol{\Delta_f}] A_f + \sum_{f=1}^{N} [\nu_f (\nabla \boldsymbol{U})_f \cdot \boldsymbol{k_f}] A_f \tag{70}$$

Now the orthogonal term can be computed implicitly by (Jasak, 1996)[54]

$$(\nabla \boldsymbol{U})_f \cdot \boldsymbol{\Delta_f} = \frac{\boldsymbol{U_p} - \boldsymbol{U_N}}{|\boldsymbol{d}|} |\Delta_f| \tag{71}$$

which is nothing but the surface normal gradient. However, the non-orthogonal term is evaluated as a source term, which is computed explicitly because it provides a negative contribution to the diagonal of the magnification matrix, as described 4.1. Therefore, the non-orthogonal term contributes to instability of the used Navier-Stokes solver. Hence,

one should take into account the type of cells that are used to generate the mesh. Alternatively, Simscale offers the non-orthogonal correction method in which the non-orthogonal term is limited by a factor γ such that

$$(\nabla \boldsymbol{U})_f \cdot \boldsymbol{k_f} < \gamma \cdot \frac{\boldsymbol{U_p} - \boldsymbol{U_N}}{|\boldsymbol{d}|} |\Delta_{\boldsymbol{f}}| \tag{72}$$

which means that stability is increased, while sacrificing accuracy. However, using the non-orthogonal correction method results in extra iteration loops, which increases the computational resources. Therefore, generating a good mesh is preferred.

E2. Differencing Schemes

In general, Simscale makes use of a central differencing scheme to compute the face flow variables

$$\phi_f = \psi \phi_N + (1 - \psi)\phi_P \tag{73}$$

where ϕ_f the computed value at the interface, ϕ_P the center value of the owner cell and ϕ_N the center value of the neighboring cell. The schematic representation of central differencing is shown in figure 82
The pre-factor ψ is computed by

$$\psi = \frac{|x_f - x_P|}{|x_N - x_P|} \tag{74}$$

Where x is the distance in m. While central differencing is a second order accurate method and is a good fit for resolving the diffusion term, unphysical values can be computed when this scheme is applied to the convection term due to numerical dispersion. Therefore, different alternative discretization schemes can be applied for the convective term in equation (18). These discretization schemes are upwind and linear upwind differencing. In general, upwind differencing depends on the direction of the mass flux at the cell interface, which is determined by

$$\dot{m}_f = \rho_f A_f (\boldsymbol{u_f} \cdot \hat{n}) \tag{75}$$

For upwind differencing the computed value at the cell interface equals

$$\phi_f = \begin{cases} \phi_P\,, & \dot{m}_f > 0 \\ \phi_N\,, & \dot{m}_f < 0 \end{cases} \tag{76}$$

The schematic representation of upwind differencing is shown in figure 83. It has to be noted that upwind differencing is only first order accurate, which in turn causes numerical diffusion as a discretization error. Consequently, one can think of a more accurate method which is called linear upwind differencing. In this method, the gradient of the value in the local cell is used to increase the accuracy of the extrapolation of the face value to second order. Hence, the face value is computed by

$$\phi_f = \begin{cases} \phi_P + (\nabla\phi)_P \cdot \boldsymbol{r}\,, & \dot{m}_f > 0 \\ \phi_N + (\nabla\phi)_N \cdot \boldsymbol{r}\,, & \dot{m}_f < 0 \end{cases} \tag{77}$$

Where $\boldsymbol{r}$ is the distance vector between the cell center and the cell face. To compute the gradients of equation (77) one makes use of gradient schemes, which are discussed in the next section. Finally, it has to be noted that by using the linear upwind differencing scheme, local maxima and minima can occur at the cell face value. These local maxima and minima can sometimes result in unphysical values, e.g. a negative turbulent kinetic energy. Therefore, a so-called

gradient limiter φ can be used to dampen these local maxima and minima. The face value for the limited linear upwind difference scheme is computed by

$$\phi_f = \begin{cases} \phi_P + \varphi(\nabla\phi)_P \cdot \boldsymbol{r}\,, & \dot{m}_f > 0 \\ \phi_N + \varphi(\nabla\phi)_N \cdot \boldsymbol{r}\,, & \dot{m}_f < 0 \end{cases} \tag{78}$$

where $0 \leq \varphi \leq 1$ and the gradient is computed using a so-called gradient scheme. Note that using gradient limiters also reduces the order of accuracy of the solution, because the original linear variation across the cell is modified. Simscale offers different versions of differencing schemes, in which so-called V-schemes are used. These schemes differ from ordinary differencing schemes in the sense that only a single limiter is calculated for a flow vector variable. For V-schemes a limiter is calculated for all the components of a vector, while for an ordinary scheme a limiter is calculated for each component of the vector. Therefore, V-schemes are computationally less expensive. The limiter is calculated based on the direction of the most rapidly changing gradient, which offers a more stable but less accurate solution. Finally, bounded schemes in Simscale can be used to increase the convergence of equation (17), in which scalars are bound between user specified limits.

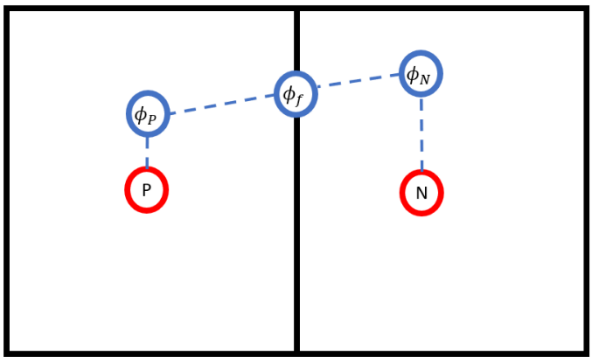

Fig. 82. Linear variation across the cell, which applies for central differencing and limited linear upwind differencing. In this picture, P denotes the owner cell and **N** the neighboring cell.

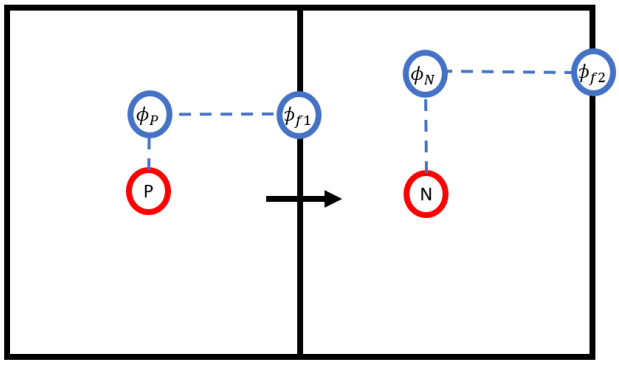

Fig. 83. Stepwise discontinuous variation across the cell, which applies for upwind differencing. In this picture, P denotes the owner cell and **N** the neighboring cell.

E3. Gradient Schemes

In a one-dimensional grid the gradient can easily be calculated by

$$\nabla\phi = \frac{\phi_N - \phi_P}{x_N - x_P} \tag{79}$$

However, when the grid becomes 2D or 3D, a more complex method is needed to compute the gradient. In general, Simscale makes use of two main different methods. The Green-Gauss cell-based method and the least squares method. In the Green-Gauss cell-based method, the divergence theorem is applied to the vector field of interest and discretized according to the second order finite volume method, using the same assumptions as described in section 4.1. Consequently, one can write for a generic cell with N faces

$$\int_V \nabla\phi \, dV = \sum_{i=1}^{N} \phi_f \hat{n}_f A_f \tag{80}$$

Because of the second order finite volume method, it can be also assumed that the variation across the cell volume is linear. Applying this assumption to equation (80) and rewriting leads to (Syrakos et al., 2017)[66]

$$(\nabla\phi)_P = \frac{1}{V_P}\sum_{i=1}^{N}\phi_f \hat{n}_f A_f \tag{81}$$

where the face values are calculated according to linear interpolation as described in equations (73) and (74). If the mesh is of bad quality linear interpolation can lead to a skewness error, as depicted in figure 84. Therefore, to reduce this error a good quality mesh is needed. Otherwise, the least squares interpolation method is preferred.

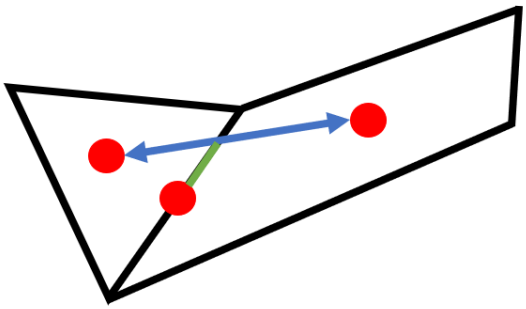

Fig. 84. Schematic illustration of the skewness error (the green line), that occurs when face values are computed using linear interpolation, in which the value is computed at the intersection of the blue line and the shared face.

In the least squares method, one can rewrite equation (79) as

$$\phi_N - \phi_P = (x_N - x_P)\cdot\nabla\phi \tag{82}$$

In 2D and in 3D the owner cell P has multiple neighboring cells N_i such that equation (82) can be written as a system of equations, where one solves for the gradient. E.g. the equation for the 3D case becomes

$$\boldsymbol{\phi_N} - \boldsymbol{\phi_P} = \begin{bmatrix} d_{PN1,x} & d_{PN1,y} & d_{PN1,z} \\ \vdots & \ddots & \vdots \\ d_{PNn,x} & d_{PNn,y} & d_{PNn,z} \end{bmatrix}\cdot\nabla\phi \tag{83}$$

where the scalar d_{PN} is the distance between the neighboring cell and the owner cell. Moreover, the number of rows is equal to the number of neighboring cells. Because this matrix is not square, no exact solution can be computed for the system of equations. This is where the least square method provides the solution where it minimizes the sum of the error squared. The error of the owner cell and a single neighboring cell i in one dimension equals

$$e_i = \phi_{N_i} - (\phi_P + \nabla\phi\cdot\boldsymbol{d}_{PNi}) \tag{84}$$

The least-square error estimation of the gradient for the system of equations can be written as

$$(\nabla\phi)_P = \left(\boldsymbol{d}^{\mathrm{T}}\boldsymbol{d}\right)^{-1}\boldsymbol{d}^T(\boldsymbol{\phi_N} - \boldsymbol{\phi_P}) \tag{85}$$

Note that $\boldsymbol{d}^T\boldsymbol{d}$ is a 3×3 square matrix making equation (85) easy to compute. However, for boundary layer problems or cells with a high aspect ratio, one can imagine that the distances between cell centroids in the streamwise direction are much greater than in the direction between cells normal to the wall, which leads to a dominance of the gradient related to the longest length scale. As a solution, one can use weighting functions

$$w_i = \frac{1}{|\boldsymbol{d}_i|} \tag{86}$$

Consequently, equation (85) can now be written as

$$(\nabla\phi)_P = \left(\boldsymbol{d}^{\mathrm{T}}\boldsymbol{d}\right)^{-1}\boldsymbol{d}^T\boldsymbol{W}^T\boldsymbol{W}(\boldsymbol{\phi_N} - \boldsymbol{\phi_P}) \tag{87}$$

Where $\boldsymbol{W}$ is a diagonal matrix of weights. The least squares method in equation (87) is second order accurate, but can be increased to fourth order accuracy by taking into account the gradients of the neighboring cells in the computation of the gradient of the owner cell (Jasak, 2017)[67]. As mentioned before, a limiter can be applied to both the Green-Gauss and Least-Squares methods to increase the stability as shown in equation (78). However, note that using this limiter decreases accuracy as $\varphi \to 1$.